

國立臺灣大學工學院化學工程學系

碩士論文

Department of Chemical Engineering

College of Engineering

National Taiwan University

Master Thesis

以分子動態模擬研究 PTT(聚對苯二甲酸丙二酯)

結晶初期行為

Early State Crystallization Process of Poly (Trimethylene
Terephthalate) (PTT) Polymer
from Atomistic Molecular Dynamics Simulations

謝旻剛

Min-Kang Hsieh

指導教授：林祥泰 博士

Advisor: Shiang-Tai Lin, Ph.D.

中華民國 97 年 7 月

July, 2008

國立臺灣大學碩士學位論文
口試委員會審定書

以分子動態模擬研究 PTT(聚對苯二甲酸丙二脂)

結晶初期行為

Early State Crystallization Process of Poly (Trimethylene
Terephthalate) (PTT) Polymer

from Atomistic Molecular Dynamics Simulations

本論文係謝晏剛君(學號 R95524014)在國立臺灣大學化學工程學系、所完成之碩士學位論文，於民國九十七年七月十七日承下列考試委員審查通過及口試及格，特此證明

口試委員：

林祥泰

(簽名)

(指導教授)

鄧錦龍

譚去真

黃慶輝

陳立仁

(簽名)

系主任、所長

誌謝

首先感謝口試委員譚玉真教授、黃慶怡教授及郭錦龍教授在百忙之中抽空前來參加我論文口試，感謝你們的指教及寶貴意見，讓我的論文增色不少。

畢業了，結束在台大六年的生活。多采多姿的大學生活，加上精實的研究生生活，成為我未來最有利的後盾。在這裡，學到的不只是專業的知識，更重要的是開闊自己的視野。分子模擬從只是引起我好其電影《透明人》中的一個鏡頭，變成了研究的工具，變成我的專業能力之一。在林祥泰教授的引領之下，了解箇中的奧妙，更給了我不一樣的角度來看這個世界所發生的每一件事，感謝林教授的提攜、教導，感謝您的協助完成本研究及碩士論文。也要感謝實驗室的每一個成員，感謝引我入門的小董學長，沒有你的棄而不顧，哪來我的迄而不捨。感謝阿伯的程式經驗分享，還有你耐心的聽我述說的研究，並在關鍵的時還提供不錯的想法。感謝阿竹、崇民及旻聰學長。感謝小傑，小容容，一起修課的歡樂，一起在實驗室待到 12 點。感謝舒潔，展嘉和孟廷在熱力學上的分享，感謝穎銘學弟，感謝博宇學弟，感謝小學弟阿源，調參數很辛苦但要更努力，感謝在這兩來來幫過我的大家。

感謝家人，感謝父親默默的支持，感謝母親為我操心，雖然你一直問我高分子是不是生物；感謝妹妹承受比較的壓力，也恭喜你學業更上一層樓。感謝前女友的支持跟鼓勵，你的離開讓我跌入深淵後更無後顧之憂的勇往直前。

摘要

以分子動態模擬研究聚對苯二甲酸丙二脂(PTT)結晶初期行為。藉由模擬恆溫結晶及拉伸程序，我們證實結晶核前驅物(precursor of nuclei)的存在，並發現其成長主要受到高分子主鏈的旋轉能量(torsional energy)及分子間凡得瓦爾作用力(van der Waals interaction)的影響。我們成功預測聚對苯二甲酸丙二脂的玻璃轉移溫度(T_g)及熔點(T_m)，並發現在恆溫結晶程序中，結晶核前驅物的總量在這兩溫度區間快速增加，接著維持週期性波動。此外；高分子主鏈藉由旋轉的分式重新排列，趨向結晶的結構。在拉伸程序中，有向性的晶核前驅物(oriented precursor)的總量大大的提升。系統中，高分子主鏈的旋轉角度分佈快速變成直鏈狀(trans-trans-trans-trans)構形。並在個別的有向性的晶核前驅物中，發現兩組旋轉角趨向結晶結構的轉變速率不同。其內部結構成長的三個因素：高分子鏈段的個數、旋轉角度(torsional angle)及排列緊密程度相互競爭或妥協，使結晶前趨物結構趨向結晶結構。由結果支持結晶前趨物在結晶初期扮演重要的角色。

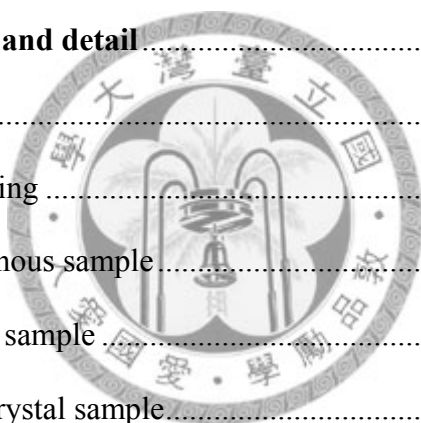
Abstract

Atomistic molecular dynamics simulations are performed to study the initial crystallization process of poly(trimethylene terephthalate) (PTT). The structure development of ordering structures (nuclei precursors) in the isothermal and stress-induced crystallization process has been observed in our simulations. The formation of nucleus precursors is found to be driven mainly by the torsional and van der Waals forces. The thermal properties, such as the glass transition temperature (T_g) and the melting temperature (T_m), determined from our simulation are in good agreement with experimental values. In isothermal processes, it is found that, between these two temperatures, the amount of precursors quickly arises during thermal relaxation period soon after the system is quenched and starts to fluctuate afterwards. The variation of precursor fraction with temperature exhibits a maximum between T_g and T_m , resembling temperature dependence of crystallization rate for most polymers. In addition, the backbone torsion distribution for segments within the precursor preferentially reorganizes to the trans-gauche-gauche-trans (t-g-g-t) conformation, the same as that in the crystalline state. On the other hand, during stress-induced crystallization, the amount of stress-induced precursor increases in all regions of temperature. The torsional distribution of the polymer backbone for segments rapidly rearrange to the t-t-t-t conformation in bulk phase. Within oriented precursors, the response of the torsional angle induced by stress is faster than that only induced by thermal stimulation, especially trans in ϕ_1 (the transition rate of trans state in ϕ_1 is faster than that of gauche state in ϕ_2). Within precursors, three factors: size, torsional angle and degree of packing found to compete/compromise during crystallization. As a consequence, we believe that the precursors play an important role as an incubator for the formation of the more compact and ordered nuclei.

Catalog

口試委員會審定書.....	i
誌謝.....	ii
摘要.....	iii
Abstract.....	iv
Catalog.....	v
Catalog of Table.....	ix
Catalog of figure.....	xi
1 Introduction.....	1
1.1 Kinetics of polymer crystallization.....	1
1.2 Existence of Precursors.....	3
1.3 Stress-induced crystallization.....	5
1.4 Polymer of PTT.....	8
1.5 The transition of conformation during crystallization.....	15
1.6 Motivation.....	17
2 Theory.....	19
2.1 Molecular dynamic simulation.....	19
2.2 Algorithm.....	19
2.3 Force field.....	20
2.3.1 Bond energy.....	21
2.3.2 Angle energy.....	21
2.3.3 Torsion energy.....	22
2.3.4 Inversion energy.....	22
2.3.5 Coulomb interaction.....	22
2.3.6 Van der Waals interaction.....	23

2.4	Thermal behavior.....	25
2.4.1	Glass transition temperature.....	25
2.4.2	Melting temperature.....	25
2.5	Mechanical properties.....	28
2.6	Definition of the segment packing structure (precursor structure).....	29
2.7	Definition of the torsion angle state.....	30
2.8	Other properties.....	31
2.8.1	Radial distribution function.....	31
2.8.2	Persistence length.....	32
2.8.3	Orientation factor.....	32
3	Computation method and detail.....	34
3.1	Method.....	34
3.2	Model building.....	35
3.2.1	Amorphous sample.....	35
3.2.2	Crystal sample.....	36
3.2.3	Semi-crystal sample.....	36
3.3	Ensemble and control detail.....	41
3.4	Force field validation.....	42
3.4.1	Crystal structure properties and torsional angles.....	42
3.4.2	Thermal properties.....	42
3.4.3	Mechanical property.....	43
3.5	Simulation process.....	48
3.5.1	Iso-thermal crystallization process.....	48
3.5.2	Stress-induced crystallization process.....	49
4	Isothermal Crystallization.....	51



4.1	Bulk properties	51
4.1.1	Density.....	51
4.1.2	Energy.....	51
4.1.3	Discussion.....	56
4.2	Structure development in PTT upon quenching.....	57
4.2.1	Precursor fraction	57
4.2.2	Degree of order of the system	60
4.2.3	Discussion.....	62
4.3	Structure development within Nucleus precursor	63
4.3.1	Structure identification	63
4.3.2	Radial distribution function.....	65
4.3.3	The average size of precursor.....	70
4.3.4	Torsion angle distribution.....	70
4.3.5	Discussion.....	73
5	Stress-Induced Crystallization.....	75
5.1	Bulk properties	75
5.1.1	Density.....	75
5.1.2	Energy.....	75
5.1.3	Discussion.....	76
5.2	Structure development of the PTT upon drawing	84
5.2.1	Precursor fraction	84
5.2.2	Degree of Order.....	89
5.2.3	Torsional angle transition.....	89
5.2.4	Discussion.....	101
5.3	Structure development within oriented precursor.	103

5.3.1	Structure identification	103
5.3.2	The RDF, average size, and torsional angle of precursors	105
5.3.3	Discussion.....	116
6	Conclusion	118
	Appendix A	120
	Appendix B	124
	Appendix C	128
	Reference	139



Catalog of Table

Table 1.1 The Avrami parameters for crystallization of polymers.....	3
Table 1.2 Summary of Avrami exponent in isothermal process.	13
Table 1.3 Summary of model's exponent in non-isothermal process.	13
Table 1.4a The kinetic crystallizability of non-isothermal process analysis by Ziabicki model[44].	14
Table 1.4b The kinetic crystallizability of non-isothermal process analysis by Ziabicki model[43].	14
Table 1.5 The identification of IR bands corresponding with propylene glycol segments.	17
Table 3.1 Comparison of the lattice parameters, density, and torsional angles of crystalline PTT.....	44
Table 3.2 Young's modulus of PTT at different condition.....	47
Table 3.3 The number of independent samples used to study stress-induced crystallization.	49
Table 3.4a The simulation time for isothermal relaxation of PTT after different draw ratios at a constant draw speed of $1 \times 10^9 \text{ s}^{-1}$	50
Table 3.4b The simulation time for isothermal relaxation of PTT after different draw ratios at constant draw speeds of $1 \times 10^{10} \text{ s}^{-1}$ and $1 \times 10^{10} \text{ s}^{-1}$	50
Table 4.1 The number and size of individual precursors identified in isothermal crystallization.	64
Table 5.1 The fraction of precursor with draw speed at $1 \times 10^9 \text{ s}^{-1}$	86
Table 5.2 The fraction of precursor with draw speed at $1 \times 10^{10} \text{ s}^{-1}$	87
Table 5.3 The fraction of precursor with draw speed at $1 \times 10^{11} \text{ s}^{-1}$	88
Table 5.4 The index of torsional angle with draw speed at $1 \times 10^9 \text{ s}^{-1}$	98

Table 5.5 The index of torsional angle with draw speed at $1 \times 10^{10} \text{s}^{-1}$	99
Table 5.6 The index of torsional angle with draw speed at $1 \times 10^{11} \text{s}^{-1}$	100
Table 5.7 The number and size of individual precursors identified in stress-induced crystallization with draw speed $1 \times 10^9 \text{s}^{-1}$	104
Table 5.8 The number and size of individual precursors identified in stress-induced crystallization with draw speed $1 \times 10^{10} \text{s}^{-1}$	104
Table 5.9 The number and size of individual precursors identified in stress-induced crystallization with draw speed $1 \times 10^{11} \text{s}^{-1}$	105
Table A.1 The definition of each atom type in atomic model.....	120
Table A.2 The value of parameters of band energy in our simulation.....	121
Table A.3 The value of parameters of angle energy in our simulation.	121
Table A.4 The value of parameters of torsion energy in our simulation.....	122
Table A.5 The value of parameters of inversion energy in our simulation.	122
Table A.5 The value of parameters of Van der Waals interaction in our simulation....	123
Table B.1 The number and size of individual precursors identified in MD simulations. (27x8)	124
Table C.1 The number and size of individual precursors identified in stress-induced crystallization with draw speed $1 \times 10^{10} \text{s}^{-1}$. (27x14)	128
Table C.2 The number and size of individual precursors identified in stress-induced crystallization with draw speed $5 \times 10^{10} \text{s}^{-1}$. (27x14)	129
Table C.3 The number and size of individual precursors identified in stress-induced crystallization with draw speed $1 \times 10^{11} \text{s}^{-1}$. (27x14)	129

Catalog of figure

Figure 1.1 Stress-draw ratio curve of melt-quenched amorphous PTT film during uniaxial drawing around T_g . [18].....	7
Figure 1.2 Crystallinity changes as a function of draw ratio for uniaxially and biaxially drawn PTT films. [18].....	8
Figure 1.3 Chemical structure of a repeating unit of PTT (a) and a fragment (4 repeating units) of the PTT chain (b). Carbon atoms are shown in grey, oxygen in red, and hydrogen in yellow. The green cylinders connecting the centers of adjacent aromatic rings are taken as elementary segments in the precursor analysis.	9
Figure 2.1 Comparison the energy barriers distribution with rotating torsion angles. Check the results of dreiding force field in ϕ_1 (solid line), and ϕ_2 (dash line) against that of quantum mechanics using the B3LYP functional and 6-31G** basis set in Gaussian 98 in ϕ_1 (triangle), and ϕ_2 (diamond).....	24
Figure 2.2 Modification the energy barriers distribution with rotating torsion angle of ϕ_1 . Accept the result of parameter $n = 3$, $K = 2$, and $d = -1$ to use in torsion energy.....	24
Figure 2.3 General variations in (a) volume, V , (b) enthalpy, H , and (c) and storage shear modulus, G' as function of temperature. Also show (d) volume expansion coefficient, α , and (e) heat capacity, C_p , which is the first derivation of V and H , respectively with respect to temperature, and (f) the loss shear modulus, G'' . [2].....	26
Figure 2.4 The viscoelastic behavior of amorphous polymer (solid line), crystalline polymer (dashed line), and cross-linking polymer (dotted line) as function of temperature. There are five regions shown as (1) glassy region, (2) glass transition region, (3) rubbery plateau region, (4) rubbery flow region, and (5) liquid flow region.[2].....	27
Figure 2.5 The volume profile with temperature of the polymer.[2].....	27

Figure 3.1 The flowchart of the calculation process.....	35
Figure 3.2 The radius of gyration (Rg) of PTT chains as the function of repeat units..	37
Figure 3.3 An amorphous structure at 600K. The system contains 4 chains of PTT molecules, each having a degree of polymerization of 27 overall 2708 atoms. The cell parameter: $a = 31.93\text{\AA}$, $b = 31.93\text{\AA}$, $c = 31.93\text{\AA}$, $\alpha = 90.00(\text{deg})$, $\beta = 90.00(\text{deg})$, $\gamma = 90.00(\text{deg})$, and density is 1.06 g/cc.....	38
Figure 3.4 A crystalline structure. The model contains 8 (2x2x2) atomic lattice cells, 4 chains of PTT molecules, each having 4 repeat units, overall 400 atoms. The cell parameter: $a = 8.66\text{\AA}$, $b = 12.56\text{\AA}$, $c = 37.39\text{\AA}$, $\alpha = 101.66(\text{deg})$, $\beta = 90.00(\text{deg})$, $\gamma = 110.11(\text{deg})$, and density is 1.47 g/cc.....	39
Figure 3.5 An equally semi-crystal structure with $X_c=18\%$. The model contains 25 chains of PTT molecule, each having a degree of polymerization of 4, overall 2550 atoms. The cell parameter: $a = 21.96\text{\AA}$, $b = 31.53\text{\AA}$, $c = 39.35\text{\AA}$, $\alpha = 90.00(\text{deg})$, $\beta = 90.00(\text{deg})$, $\gamma = 90.00(\text{deg})$, and density is 1.33 g/cc.....	40
Figure 3.6 The density variation of PTT upon cooling and heating. The 600K equilibrated sample cooled to 50K (open square) and 50K equilibrated sample heated to molten state (open circle). Each process was performed by step changes of temperature of 25K after 25ps.....	45
Figure 3.7 The plot of the stress and strain curve. In all case, the slope of three lines is uniform. The technique of black average (3% of stain) used in data analysis results in the data shown form -1.5% to 1.5%. This example is drawn with draw speed $1 \times 10^{10} \text{s}^{-1}$ in x-direction at 200K.....	46
Figure 3.8 The calculated Yonug's modulus is a function of the temperature and draw speeds. The average curve considers all draw speeds.....	46
Figure 3.9 The cooling and iso-thermal crystallization processes.....	48

Figure 4.1 The time evolution of density during relaxation at different temperature....	52
Figure 4.2 The time evolution of kinetic energy.....	52
Figure 4.3 The time evolution of potential energy during relaxation at different temperature.....	53
Figure 4.4 the time evolution of bond energy during relaxation at different temperature.	53
Figure 4.5 the time evolution of angle energy during relaxation at different temperature.	54
Figure 4.6 The time evolution of torsional energy during relaxation at different temperature.....	54
Figure 4.7 the time evolution of inversion energy during relaxation at different temperature.....	55
Figure 4.8 The time evolution of coulomb energy during relaxation at different temperature.....	55
Figure 4.9 The time evolution of van der Waals interaction during relaxation at different temperature.....	56
Figure 4.10 The variation of the amount of the precursor (defined in equationn 2.14) with time at 350, 400, and 450K. (27x4).....	58
Figure 4.11 The variation of the average amount of the precursor (defined in equationn 2.14) with temperature. (27x4).....	58
Figure 4.12 The variation of the amount of the precursor (defined in equationn 2.14) with time at 350, 400, and 450K. (27x8).....	59
Figure 4.13 The variation of the average amount of the precursor (defined in equationn 2.14) with temperature. (27x8).....	59
Figure 4.14 The RDF of the quenched PTT state at 400K.	60

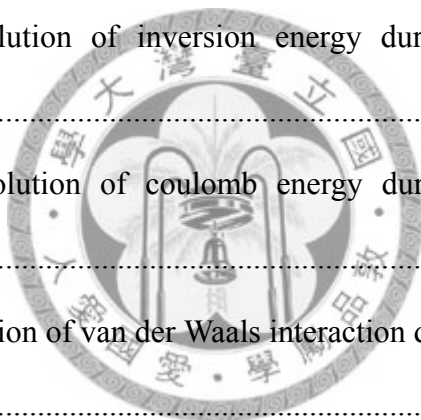


Figure 4.15 The probability of the atoms in the PTT quenched state at 400K.	61
Figure 4.16 The orientation factor in the PTT quenched state at 400K.....	61
Figure 4.17 Illustration of the growth of nucleus precursor from melted state at 400 K. A color scale is used for better discrimination of the size of precursors.....	64
Figure 4.18 The RDF of 1,4 carbon atoms in crystalline PTT structure during a heating process.....	66
Figure 4.19 The RDF of precursor at 300K.....	66
Figure 4.20 The RDF of precursor at 350K.....	67
Figure 4.21 The RDF of precursor at 400K.....	67
Figure 4.22 The RDF of precursor at 450K.....	68
Figure 4.23 The time evolution of RDF intensity (4.11Å) (diamond) and the time averaged number of parallel segments contained in a representative precursor (triangle) at 300 K.	68
Figure 4.24 The time evolution of RDF intensity (4.11Å) (diamond) and the time averaged number of parallel segments contained in a representative precursor (triangle) at 350 K.	69
Figure 4.25 The time evolution of RDF intensity (4.11Å) (diamond) and the time averaged number of parallel segments contained in a representative precursor (triangle) at 400 K.	69
Figure 4.26 The time evolution of RDF intensity (4.11Å) (diamond) and the time averaged number of parallel segments contained in a representative precursor (triangle) at 450 K.	70
Figure 4.27 the backbone torsions $\langle\phi_1\rangle$ in trans (triangles) and $\langle\phi_2\rangle$ in gauche (circles) for segments in a precursor (closed symbols) and outside any precursor (open symbols) at 300 K.	71

Figure 4.28 the backbone torsions $\langle\phi_1\rangle$ in trans (triangles) and $\langle\phi_2\rangle$ in gauche (circles) for segments in a precursor (closed symbols) and outside any precursor (open symbols) at 300 K.	71
Figure 4.29 the backbone torsions $\langle\phi_1\rangle$ in trans (triangles) and $\langle\phi_2\rangle$ in gauche (circles) for segments in a precursor (closed symbols) and outside any precursor (open symbols) at 300 K.	72
Figure 4.30 the backbone torsions $\langle\phi_1\rangle$ in trans (triangles) and $\langle\phi_2\rangle$ in gauche (circles) for segments in a precursor (closed symbols) and outside any precursor (open symbols) at 300 K.	72
Figure 4.31 The percentage of these torsions in the trans and gauche states within all precursors.	73
Figure 5.1 The DR variation of density at different temperatures with draw speed $1 \times 10^9 \text{ s}^{-1}$	77
Figure 5.2 The temperature dependence of density at different DR with draw speed $1 \times 10^9 \text{ s}^{-1}$	77
Figure 5.3 The DR variation of density at different temperatures with draw speed $1 \times 10^{10} \text{ s}^{-1}$	78
Figure 5.4 The temperature dependence of density at different DR with draw speed $1 \times 10^{10} \text{ s}^{-1}$	78
Figure 5.5 The DR variation of density at different temperatures with draw speed $1 \times 10^{11} \text{ s}^{-1}$	79
Figure 5.6 The temperature dependence of density at different DR with draw speed $1 \times 10^{11} \text{ s}^{-1}$	79
Figure 5.7 The temperature dependence of torsional energy at different DR with draw speed $1 \times 10^9 \text{ s}^{-1}$	80

Figure 5.8 The temperature dependence of van der Waals interaction at different DR with draw speed $1 \times 10^9 \text{ s}^{-1}$	80
Figure 5.9 The temperature dependence of torsional energy at different DR with draw speed $1 \times 10^{10} \text{ s}^{-1}$	81
Figure 5.10 The temperature dependence of van der Waals interaction at different DR with draw speed $1 \times 10^{10} \text{ s}^{-1}$	81
Figure 5.11 The temperature dependence of torsional energy at different DR with draw speed $1 \times 10^{11} \text{ s}^{-1}$	82
Figure 5.12 The temperature dependence of van der Waals interaction at different DR with draw speed $1 \times 10^{11} \text{ s}^{-1}$	82
Figure 5.13 The draw speed dependence of density, torsional energy, and van der Waals interaction at different DR.....	83
Figure 5.14 The temperature dependence of precursor fraction at different DR with draw speed $1 \times 10^9 \text{ s}^{-1}$	84
Figure 5.15 The temperature dependence of precursor fraction at different DR with draw speed $1 \times 10^{10} \text{ s}^{-1}$	85
Figure 5.16 The temperature dependence of precursor fraction at different DR with draw speed $1 \times 10^{11} \text{ s}^{-1}$	85
Figure 5.17 The DR variation of RDF at (a) 400K, (b) 300K, and (c) 200K with draw speed $1 \times 10^9 \text{ s}^{-1}$	90
Figure 5.18 The DR variation of RDF at (a) 400K, (b) 300K, and (c) 200K with draw speed $1 \times 10^{10} \text{ s}^{-1}$	90
Figure 5.19 The DR variation of RDF at (a) 400K, (b) 300K, and (c) 200K with draw speed $1 \times 10^{11} \text{ s}^{-1}$	91
Figure 5.20 The results of orientation factor at various temperatures and DR.....	91

Figure 5.21 The percentage of trans state depends on temperature at DR=2, 3, and 4 with draw speed $1 \times 10^9 \text{ s}^{-1}$	92
Figure 5.22 The percentage of trans state depends on temperature at DR=2, 3, and 4 with draw speed $1 \times 10^{10} \text{ s}^{-1}$	92
Figure 5.23 The percentage of trans state depends on temperature at DR=2, 3, and 4 with draw speed $1 \times 10^{11} \text{ s}^{-1}$	93
Figure 5.24 The percentage of gauche state depends on temperature at DR=2, 3, and 4 with draw speed $1 \times 10^9 \text{ s}^{-1}$	93
Figure 5.25 The percentage of gauche state depends on temperature at DR=2, 3, and 4 with draw speed $1 \times 10^{10} \text{ s}^{-1}$	94
Figure 5.26 The percentage of gauche state depends on temperature at DR=2, 3, and 4 with draw speed $1 \times 10^{11} \text{ s}^{-1}$	94
Figure 5.27 The trans-to-gauche ratio in ϕ_1 depends on temperature at DR=2, 3, and 4 with draw speed $1 \times 10^9 \text{ s}^{-1}$	95
Figure 5.28 The trans-to-gauche ratio in ϕ_1 depends on temperature at DR=2, 3, and 4 with draw speed $1 \times 10^{10} \text{ s}^{-1}$	95
Figure 5.29 The trans-to-gauche ratio in ϕ_1 depends on temperature at DR=2, 3, and 4 with draw speed $1 \times 10^{11} \text{ s}^{-1}$	96
Figure 5.30 The gauche-to-trans ratio in ϕ_2 depends on temperature at DR=2, 3, and 4 with draw speed $1 \times 10^9 \text{ s}^{-1}$	96
Figure 5.31 The gauche-to-trans ratio in ϕ_2 depends on temperature at DR=2, 3, and 4 with draw speed $1 \times 10^{10} \text{ s}^{-1}$	97
Figure 5.32 The gauche-to-trans ratio in ϕ_2 depends on temperature at DR=2, 3, and 4 with draw speed $1 \times 10^{11} \text{ s}^{-1}$	97
Figure 5.33 The time evolution of RDF intensity (4.11 \AA) (diamond) and the time	

averaged number of parallel segments contained in a representative precursor (triangle) at 200 K with draw speed $1 \times 10^9 \text{s}^{-1}$	106
Figure 5.34 The backbone torsions $\langle \phi_1 \rangle$ in trans (triangles) and $\langle \phi_2 \rangle$ in gauche (circles) for segments in a precursor at 200K with draw speed $1 \times 10^9 \text{s}^{-1}$	106
Figure 5.35 The time evolution of RDF intensity (4.11\AA) (diamond) and the time averaged number of parallel segments contained in a representative precursor (triangle) at 300 K with draw speed $1 \times 10^9 \text{s}^{-1}$	107
Figure 5.36 The backbone torsions $\langle \phi_1 \rangle$ in trans (triangles) and $\langle \phi_2 \rangle$ in gauche (circles) for segments in a precursor at 300K with draw speed $1 \times 10^9 \text{s}^{-1}$	107
Figure 5.37 The time evolution of RDF intensity (4.11\AA) (diamond) and the time averaged number of parallel segments contained in a representative precursor (triangle) at 400 K with draw speed $1 \times 10^9 \text{s}^{-1}$	108
Figure 5.38 The backbone torsions $\langle \phi_1 \rangle$ in trans (triangles) and $\langle \phi_2 \rangle$ in gauche (circles) for segments in a precursor at 400K with draw speed $1 \times 10^9 \text{s}^{-1}$	108
Figure 5.39 The time evolution of RDF intensity (4.11\AA) (diamond) and the time averaged number of parallel segments contained in a representative precursor (triangle) at 200 K with draw speed $1 \times 10^{10} \text{s}^{-1}$	109
Figure 5.40 The backbone torsions $\langle \phi_1 \rangle$ in trans (triangles) and $\langle \phi_2 \rangle$ in gauche (circles) for segments in a precursor at 200K with draw speed $1 \times 10^{10} \text{s}^{-1}$	109
Figure 5.41 The time evolution of RDF intensity (4.11\AA) (diamond) and the time averaged number of parallel segments contained in a representative precursor (triangle) at 300 K with draw speed $1 \times 10^{10} \text{s}^{-1}$	110
Figure 5.42 The backbone torsions $\langle \phi_1 \rangle$ in trans (triangles) and $\langle \phi_2 \rangle$ in gauche (circles) for segments in a precursor at 300K with draw speed $1 \times 10^{10} \text{s}^{-1}$	110
Figure 5.43 The time evolution of RDF intensity (4.11\AA) (diamond) and the time	

averaged number of parallel segments contained in a representative precursor (triangle) at 400 K with draw speed $1 \times 10^{10} \text{ s}^{-1}$	111
Figure 5.44 The backbone torsions $\langle \phi_1 \rangle$ in trans (triangles) and $\langle \phi_2 \rangle$ in gauche (circles) for segments in a precursor at 400K with draw speed $1 \times 10^{10} \text{ s}^{-1}$	111
Figure 5.45 The time evolution of RDF intensity (4.11 \AA) (diamond) and the time averaged number of parallel segments contained in a representative precursor (triangle) at 200 K with draw speed $1 \times 10^{11} \text{ s}^{-1}$	112
Figure 5.46 The backbone torsions $\langle \phi_1 \rangle$ in trans (triangles) and $\langle \phi_2 \rangle$ in gauche (circles) for segments in a precursor at 200K with draw speed $1 \times 10^{11} \text{ s}^{-1}$	112
Figure 5.47 The time evolution of RDF intensity (4.11 \AA) (diamond) and the time averaged number of parallel segments contained in a representative precursor (triangle) at 300 K with draw speed $1 \times 10^{11} \text{ s}^{-1}$	113
Figure 5.48 The backbone torsions $\langle \phi_1 \rangle$ in trans (triangles) and $\langle \phi_2 \rangle$ in gauche (circles) for segments in a precursor at 300K with draw speed $1 \times 10^{11} \text{ s}^{-1}$	113
Figure 5.49 The time evolution of RDF intensity (4.11 \AA) (diamond) and the time averaged number of parallel segments contained in a representative precursor (triangle) at 400 K with draw speed $1 \times 10^{11} \text{ s}^{-1}$	114
Figure 5.50 The backbone torsions $\langle \phi_1 \rangle$ in trans (triangles) and $\langle \phi_2 \rangle$ in gauche (circles) for segments in a precursor at 400K with draw speed $1 \times 10^{11} \text{ s}^{-1}$	114
Figure 5.51 The temperature dependence of the growth rate of precursor size with different draw speeds.....	115
Figure 5.52 The temperature dependence of transition rate of torsional angle ϕ_1 with different draw speeds.....	115
Figure 5.53 The temperature dependence of transition rate of torsional angle ϕ_2 with different draw speeds.....	116

Figure A.1 The atomic position on the PTT polymer repeat unit.	120
Figure B.1 The time evolution of RDF intensity (4.11Å) (diamond) and the time averaged number of parallel segments contained in a representative precursor (triangle) at 350 K. (27x8).....	125
Figure B.2 the backbone torsions $\langle\phi_1\rangle$ in trans (triangles) and $\langle\phi_2\rangle$ in gauche (circles) for segments in a precursor (closed symbols) and outside any precursor (open symbols) at 350 K. (27x8).....	125
Figure B.3 The time evolution of RDF intensity (4.11Å) (diamond) and the time averaged number of parallel segments contained in a representative precursor (triangle) at 400 K. (27x8).....	126
Figure B.4 the backbone torsions $\langle\phi_1\rangle$ in trans (triangles) and $\langle\phi_2\rangle$ in gauche (circles) for segments in a precursor (closed symbols) and outside any precursor (open symbols) at 350 K. (27x8).....	126
Figure B.5 The time evolution of RDF intensity (4.11Å) (diamond) and the time averaged number of parallel segments contained in a representative precursor (triangle) at 450 K. (27x8).....	127
Figure B.6 the backbone torsions $\langle\phi_1\rangle$ in trans (triangles) and $\langle\phi_2\rangle$ in gauche (circles) for segments in a precursor (closed symbols) and outside any precursor (open symbols) at 350 K. (27x8).....	127
Figure C.1 The time evolution of RDF intensity (4.11Å) (diamond) and the time averaged number of parallel segments contained in a representative precursor (triangle) at 200 K with draw speed $1 \times 10^{10} \text{s}^{-1}$. (27x14).....	130
Figure C.2 the backbone torsions $\langle\phi_1\rangle$ in trans (triangles) and $\langle\phi_2\rangle$ in gauche (circles) for segments in a precursor (closed symbols) and outside any precursor (open symbols) at 200 K with draw speed $1 \times 10^{10} \text{s}^{-1}$. (27x14).....	130

Figure C.3 The time evolution of RDF intensity (4.11Å) (diamond) and the time averaged number of parallel segments contained in a representative precursor (triangle) at 300 K with draw speed $1 \times 10^{10} \text{s}^{-1}$. (27x14).....	131
Figure C.4 the backbone torsions $\langle \phi_1 \rangle$ in trans (triangles) and $\langle \phi_2 \rangle$ in gauche (circles) for segments in a precursor (closed symbols) and outside any precursor (open symbols) at 300 K with draw speed $1 \times 10^{10} \text{s}^{-1}$. (27x14).....	131
Figure C.5 The time evolution of RDF intensity (4.11Å) (diamond) and the time averaged number of parallel segments contained in a representative precursor (triangle) at 400 K with draw speed $1 \times 10^{10} \text{s}^{-1}$. (27x14).....	132
Figure C.6 the backbone torsions $\langle \phi_1 \rangle$ in trans (triangles) and $\langle \phi_2 \rangle$ in gauche (circles) for segments in a precursor (closed symbols) and outside any precursor (open symbols) at 400 K with draw speed $1 \times 10^{10} \text{s}^{-1}$. (27x14).....	132
Figure C.7 The time evolution of RDF intensity (4.11Å) (diamond) and the time averaged number of parallel segments contained in a representative precursor (triangle) at 200 K with draw speed $5 \times 10^{10} \text{s}^{-1}$. (27x14).....	133
Figure C.8 the backbone torsions $\langle \phi_1 \rangle$ in trans (triangles) and $\langle \phi_2 \rangle$ in gauche (circles) for segments in a precursor (closed symbols) and outside any precursor (open symbols) at 200 K with draw speed $5 \times 10^{10} \text{s}^{-1}$. (27x14).....	133
Figure C.9 The time evolution of RDF intensity (4.11Å) (diamond) and the time averaged number of parallel segments contained in a representative precursor (triangle) at 300 K with draw speed $5 \times 10^{10} \text{s}^{-1}$. (27x14).....	134
Figure C.10 the backbone torsions $\langle \phi_1 \rangle$ in trans (triangles) and $\langle \phi_2 \rangle$ in gauche (circles) for segments in a precursor (closed symbols) and outside any precursor (open symbols) at 300 K with draw speed $5 \times 10^{10} \text{s}^{-1}$. (27x14).....	134
Figure C.11 The time evolution of RDF intensity (4.11Å) (diamond) and the time	

averaged number of parallel segments contained in a representative precursor (triangle) at 400 K with draw speed $5 \times 10^{10} \text{s}^{-1}$. (27x14).....	135
Figure C.12 the backbone torsions $\langle \phi_1 \rangle$ in trans (triangles) and $\langle \phi_2 \rangle$ in gauche (circles) for segments in a precursor (closed symbols) and outside any precursor (open symbols) at 400 K with draw speed $5 \times 10^{10} \text{s}^{-1}$. (27x14).....	135
Figure C.13 The time evolution of RDF intensity (4.11\AA) (diamond) and the time averaged number of parallel segments contained in a representative precursor (triangle) at 200 K with draw speed $1 \times 10^{11} \text{s}^{-1}$. (27x14).....	136
Figure C.14 the backbone torsions $\langle \phi_1 \rangle$ in trans (triangles) and $\langle \phi_2 \rangle$ in gauche (circles) for segments in a precursor (closed symbols) and outside any precursor (open symbols) at 200 K with draw speed $1 \times 10^{11} \text{s}^{-1}$. (27x14).....	136
Figure C.15 The time evolution of RDF intensity (4.11\AA) (diamond) and the time averaged number of parallel segments contained in a representative precursor (triangle) at 300 K with draw speed $1 \times 10^{11} \text{s}^{-1}$. (27x14).....	137
Figure C.16 the backbone torsions $\langle \phi_1 \rangle$ in trans (triangles) and $\langle \phi_2 \rangle$ in gauche (circles) for segments in a precursor (closed symbols) and outside any precursor (open symbols) at 300 K with draw speed $1 \times 10^{11} \text{s}^{-1}$. (27x14).....	137
Figure C.17 The time evolution of RDF intensity (4.11\AA) (diamond) and the time averaged number of parallel segments contained in a representative precursor (triangle) at 400 K with draw speed $1 \times 10^{11} \text{s}^{-1}$. (27x14).....	138
Figure C.18 the backbone torsions $\langle \phi_1 \rangle$ in trans (triangles) and $\langle \phi_2 \rangle$ in gauche (circles) for segments in a precursor (closed symbols) and outside any precursor (open symbols) at 400 K with draw speed $1 \times 10^{11} \text{s}^{-1}$. (27x14).....	138

1 Introduction

Since the first polymer, Ketenes, was found in 1905 by Hermann Staudinger, polymers have become a popular material for various applications, such as bags, bottles and clothing. After one-century's development, we now know that "polymer crystallization controls the structural formation processes of polymeric materials and thereby dominates the properties of the final polymer products,"[1] and the crystalline phase improves mechanic strength. To design favorable microscopic and macroscopic structures of crystalline polymer, it is important to understand the molecular mechanism of polymer crystallization. The followings are introductions of the issues we focus on.

1.1 Kinetics of polymer crystallization

The crystalline structure has been extensively studied since the X-ray diffraction technology was first time applied to crystalline substances in 1912 by Von Laue[2]. The structure of the crystalline in one unit cell was not fully understood until the method of preparing the single crystalline discovered in 1957 by Keller[3]. General speaking, the crystal structure was described from large scale to small as following: the spherulitic structure in micro scale, the lamellae structure in nano scale, the lattice cell structure in atomic scale; all of them have been found by light scattering techniques, such as Depolarized Light-scattering, Electron Micrograph, Wide-angle X-ray Diffraction, and Electron diffraction methods.

How a crystal structure created from the bulk amorphous polymer was an interesting problem accompanied with observing the crystal structure. The kinetics of the

crystallization was studied to try solving the problem. In 1939, the first theory of crystallization kinetics was reported by Avrami[4], and proposed the Avrami equation which intended form metallurgy to the polymer science. Many researches base on this theory to identify the Avrami parameters of polymers, and proposed the crystallization mechanism based on the value of the parameters which summarize in **Table 1.1** (See **equation 1.1** for the Avarami equation). However, the theory can not explain the molecular organization of crystalline region, structure of the spherulities, and so on. In 1964, another theory was developed by Keith and Padden[5], addressing the kinetics of spherulitic growth by radial growth rate which was interpreted as a competition between the formation of the critical size at surface nucleus (rate of nucleation) and a chain crossing the energy barrier to the crystal (rate of chain diffusion). In 1976, Hoffman and co-workers derived the growth rate equation from the free energy differences between the chain folding and lamellar formation[2]. Hoffman defined three temperature regimes of crystallization kinetics and explained how different rates of the secondary nucleation affect the growth rate. The mechanism of the secondary nucleation (growth of nucleus) is well understood and widely accepted as a result of their works. In contrast, there are still debates on the mechanism of primary nucleation in polymers. (See **1.2 Existence of Precursors**)

To summarize the classical theory of nucleation, the crystallization of a material when cooled to a temperature below its melting point is generally recognized to be a two-stage process. In the stage of primary nucleation, crystal nuclei (clusters comprising ordered molecules) appear and re-dissolve via molecular collisions until the size of a nucleus reaches some critical value, above which the nuclei is thermodynamically stable. The subsequent growth of the critical nuclei follows kinetic mechanism and is classified

as growth stage. Complicated by additional constraints in topological connectivity, the crystallization in polymers presents remarkable differences both in the nucleation and in the growth stages when compared to that in small molecules.

Table 1.1 The Avrami parameters for crystallization of polymers

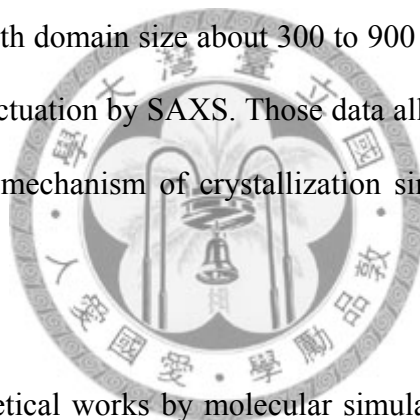
	Crystallization mechanism	Avrami parameters		Restrictions
		Z	n	
Spheres	Sporadic	$2/3\pi g^3 l$	4	3 dimension
	Predetermined	$4/3\pi g^3 L$	3	3 dimension
Discs	Sporadic	$1/3\pi g^2 l d$	3	2 dimension
	Predetermined	$\pi g^2 L d$	2	2 dimension
Rods	Sporadic	$1/4\pi g^2 l d^2$	2	1 dimension
	Predetermined	$1/2\pi g L d^2$	1	1 dimension

1.2 Existence of Precursors

Experimentally it was observed a very long induction period prior to polymer crystallization[6]. What happens during the induction period has been an interest of many polymer scientists. In classical nucleation theory, the important assumption is the system remains homogenous before the actual nucleation and growth process set in. However, a number of experiments show that the assumption is not always justified. Some researches supported that the spinodal phase separation takes place prior to nucleation. In Imai's research, the induction period of the crystallization of poly(ethylene terephthalate) (PET) has been found some ordering structure created by SAXS, WAXS in 1992[7], SANS in 1995[6] before crystallization takes place. Heeley reported similar results in 2003[8], studying the early stages of the crystallization of Isotactic Polypropylene (iso-PP). On the other hand, In 1997, Fukao[9] and in 2007,

Soccio[10] reported the dynamical transition of the dielectric value at early stage of PET and Poly(propylene succinate) (PPS) crystallization relatively. Those results indicate certain structure development during the induction period.

However, the existence of nucleus precursors is criticized by some researchers. In 2000, Wang [11] reported the result of the early stages of melt crystallization in Isotactic Polypropylene (iPP) by WAXS, SAXS, and PL. He claimed that the accuracy of experimental data from these measurements depend on the amount of crystallinity. Before WAXS detecting the crystal structure, SAXS has observed the peak corresponding to a lamellar repeating structure in 20 to 24 nm region. Eventually the local orientational order with domain size about 300 to 900 nm was found by PL before the detection of density fluctuation by SAXS. Those data all follow an expected Avrami form, suggesting a single mechanism of crystallization since the early stage (i.e., no precursor formation).



Recently, some theoretical works by molecular simulation have been reported. In 1998, Muthukumar' group reported the formation of the lamella structure during the nucleation process by a single chain from Langevin dynamic simulations[12]. In 2000, they reported the nucleation progress by longer chain. Several "baby nuclei" (order structure in the early stage of the crystallization) in the same single chain are formed at the beginning process, and then become several "smectic pearls". After further growth, the highly oriented and eventually chain-folded crystals appear[13]. Moreover, the properties and behaviors of the bulk polymer systems (more than one chain) have been studied. In 2006, Gee[14] reported precursor formation as the polymer melts are deep quenched into the unstable region where spinodal decomposition starts. He chose

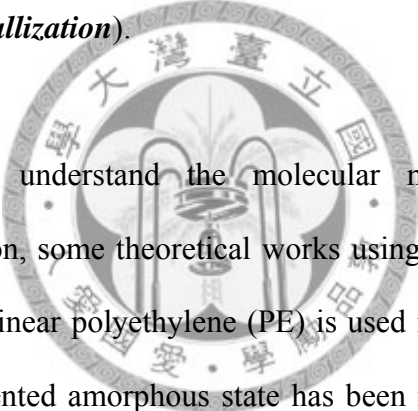
poly(vinylidene fluoride) (PVDF), and polyethylene (PE) as marital, used a very large size (450,000 to 500,000 united atoms) system, and observed the phenomenon of spinodal liquid-liquid phase separation upon rapidly cooling from melt state. In 2007, Miura[15] observed the ordering process in confined domain and isotropic domain assuming the constrained effect of surrounding amorphous medium are strong and weak, respectively. He concluded that the high rigidity of polymer and strong restriction of the surrounding domain interface encourage the information of the ordering structure.

1.3 Stress-induced crystallization

The phenomena of stress-induced (or flow-induced, strain-induced, force-induced) crystallization is that polymer segments are oriented along the elongated direction due to applied force. Many researches report that the drawing and spinning process would increase the crystallinity of polymeric materials, resulting in oriented segments that would explosively improve the crystallization by oriented nucleus.[1] The oriented nucleus of PTT may be created above 310K(38°C)[16] and almost be competed below 353K(80°C).[17]

There are many papers showing the evidences of the structural changes during drawing and spinning processes. The behavior of stress-draw ratio curve of the melt-quenched amorphous PTT film during uniaxial drawing could be divided to there regions, including initial(I), plateau(II), and final(III) [18, 19].(Figure 1.1) A further increase of the draw ratio above 2.5 causes a significant strain hardening as shown in region III. The fast increase of the modulus in this region indicates that there might be major structural changes occurring in addition to the orientation of the chain along the

deformation direction. Simultaneously, the crystallinity (measured by density) of the PTT abruptly rise at draw ratio 2.5. (**Figure 1.2**) On the other hand, the oriented structure development is observed by orientation factor (the definition of which can be found in **2.8.3 orientation factor**). Orientation factor of the melt-quenched amorphous PTT film, calculated by IR dichroic ratio of characteristic bands (by equation 2.18), increase with increasing draw ratio[16]. Similarly, Orientation factor of partial oriented yarns (POY) PTT fiber, which is calculated by intensity of WXRD (by equation 2.19), increase with increasing draw ratio and take-up speed[20]. Moreover, the birefringence of PTT increase with spinning speeds. Besides, the conformation of PTT chain change during drawing or spinning process (which will be discussed in **1.5 The transition of conformation during crystallization**).



In order to further understand the molecular mechanical mechanism of stress-induced crystallization, some theoretical works using molecular simulation have been conducted recently. Linear polyethylene (PE) is used in most of simulations. The crystallization from an oriented amorphous state has been reported by Koyama[21] in 2002. The crystallization, spending around 30 ns simulation time, is evidenced by the increase of mean length of the trans sequences, and the increase order in the pre-oriented direction. Furthermore, the temperature effect and non-isothermal extensive process are considered by Lavine [22] in 2003. The orientation factor increase with draw ratio until high extension, and the number of crystals, crystal size, and the angle that the crystal c-axis align along the stress direction, increase as the annealing temperature increases. In non-isothermal extensional process, the crystallization is observed to show the rapid densification corresponding to increasing order parameter between 360K and 320K (around T_m). He also proposed that the mechanism of oriented

crystallization can be interpreted as competition between the rate of the relaxation of deformation-induced orientation and the rate of the nucleation which locks in structure at some level of orientation. Moreover, the extensional flow process inducing the shish-kebab crystallization has been reported by Dukovski[23] in 2003, and the secondary nucleation process by creating a knot in the polymer system has been studied by Saitta[24] in 2002.

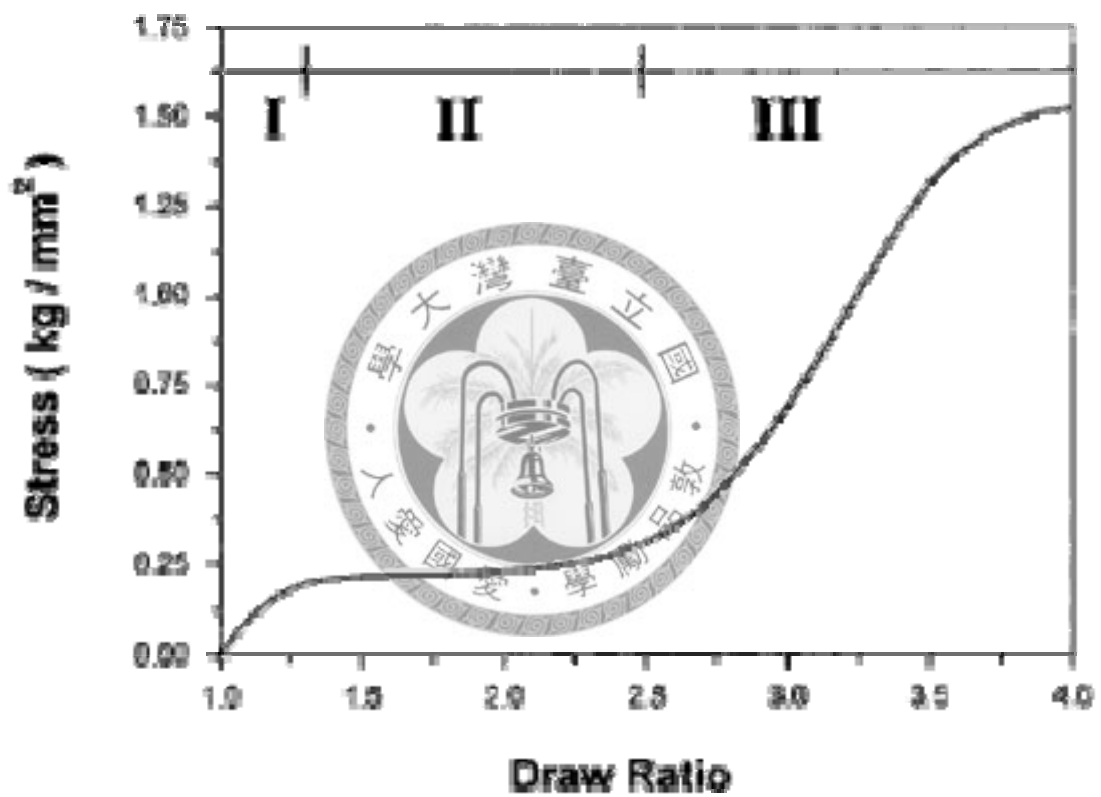


Figure 1.1 Stress-draw ratio curve of melt-quenched amorphous PTT film during uniaxial drawing around T_g . [18]

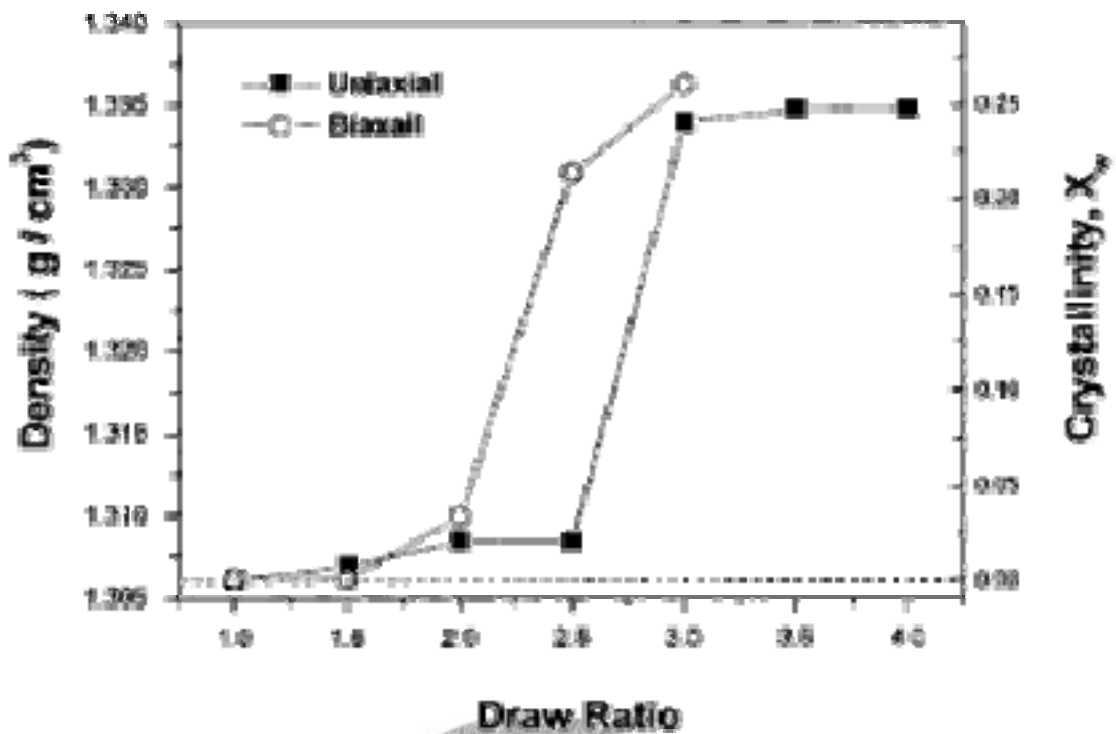
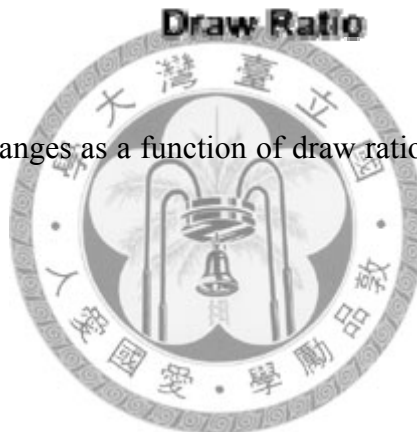


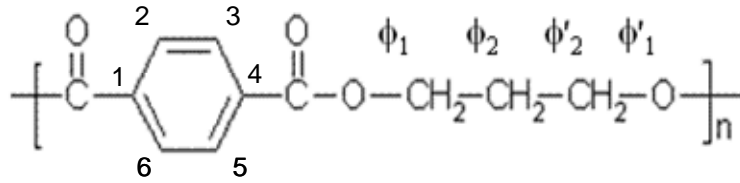
Figure 1.2 Crystallinity changes as a function of draw ratio for uniaxially and biaxially drawn PTT films. [18]



1.4 Polymer of PTT

Poly (Trimethylene Terephthalate) (PTT), such as Poly(Ethylene Terephthalate) (PET) and Poly(Buthylene Terephthalate) (PBT), is a member of aromatic polyester polymers. (**Figure 1.3**) PTT is synthesized by the condensation of 1,3-propanediol (PDO) with either terephthalic acid or dimethyl terephthalic. Recently, breakthroughs in raw material, PDO, synthesis reduce the cost of PTT, and offer a chance to catch up with its homologues neighbors PET and PBT in the commercial material markets.

a)



b)

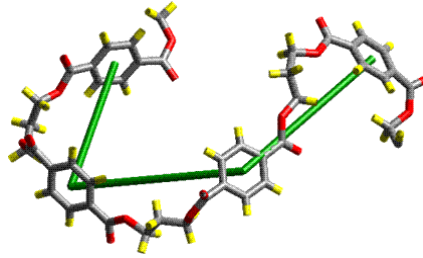


Figure 1.3 Chemical structure of a repeating unit of PTT (a) and a fragment (4 repeating units) of the PTT chain (b). Carbon atoms are shown in grey, oxygen in red, and hydrogen in yellow. The green cylinders connecting the centers of adjacent aromatic rings are taken as elementary segments in the precursor analysis.

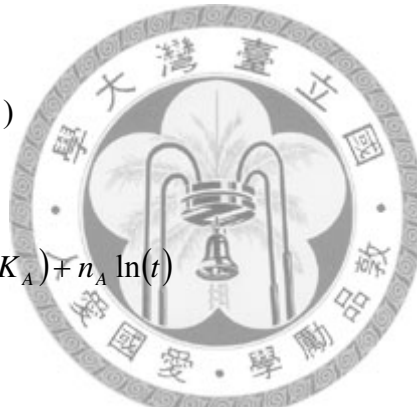
The crystal structure, mechanical properties, and thermal properties of PTT have been reported experimentally. PTT is a triclinic crystalline structure which contains two chemical repeat in each cell, with the cell parameters reported in **Table 3.1**. The purely crystalline density is 1.387~1.43 g/cc[25-27] by theoretical calculations; the experimental density of semicrystalline is reported to be 1.31~1.35g/cc [16, 28]; the simulation result is reported to be 1.262 g/cc[29]. In PTT crystal structure, three methylene units exhibit very compliant gauche-gauche conformation resulting in its outstanding elastic recovery and resiliency compared to PBT and PET. Experimental measurement of Young's modulus is reported to be 2.3~2.8GPa[30-32]; the simulation results were reported to be 3.84±0.16 GPa in amorphous system[29] , and 6.31±0.64

GPa in semicrystalline system[33]. Besides, the experimental result of the melting point is reported to be 499~503K[34-36], and the equilibrium melting temperature T_m^0 is estimated to be 510~525K[37, 38] by linear Hoffman-Weeks extrapolation (LHW), and 546~578K[38] by non-linear Hoffman-Weeks extrapolation (NLHW). The glass transition temperature is reported to be 315~348K.[30, 35]

The crystallization behaviors of PTT have been studied by *isothermal (melt and quench) crystallization* and *non-isothermal crystallization* process. In isothermal process, Avrami model is the most popular theory for analysis of the crystallization rate from experiment:

$$X(t) = 1 - \exp(-K_A t^{n_A}) \quad (1.1a)$$

$$\ln\{-\ln[1 - X(t)]\} = \ln(K_A) + n_A \ln(t) \quad (1.1b)$$



where $X(t)$ is normalized crystallinity at time t , k is crystallization rate constant, and n_A is Avrami exponent. (See **Table 1.1**) From the data fitting by the equation (1.1b), the crystallization behavior can be identified as primary crystallization, which consists of an outward growth of lamellar stacks until impingement, and a secondary crystallization of filling in the spherulities of interstices[36]. Some results suggest that both primary and secondary crystallizations overlap[36], but others consider the secondary crystallization occurs after primary process completes[39]. The Avrami exponent, n , have been reported with different temperature region shown in **Table 1.2**. Based on the n_A value, we know that the mechanism of the primary crystallization are an athermal nucleation with two-dimensional crystallization growth ($n_A=2$) above T_g , and three-dimensional

crystallization growth ($n_A=3$) around T_m . The high n_A value ($n_A=5$) indicates a solid sheaf growth with athermal nucleation in cold crystallization about T_g . On the other hand, except Avrami model[40, 41], a modified Avrami model[42], Ozawa model[41, 42], and Ziabicki model[42] have been used to analyze the crystallization rate in non-isothermal crystallization, respectively.

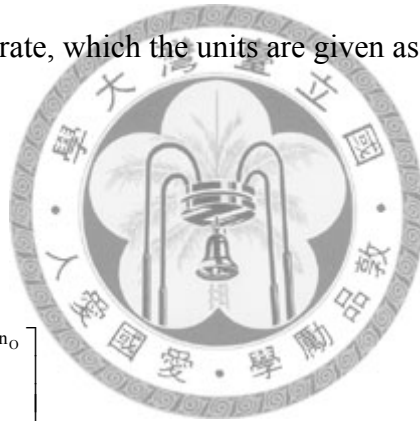
Modified Avrami model

$$X(t) = 1 - \exp\left[-K_A t^{n_A}\right] \quad (1.2)$$

where K_A is crystallization rate, which the units are given as inverse of time,

Ozawa model

$$X(T) = 1 - \exp\left[-\left(\frac{K_O}{\phi}\right)^{n_O}\right] \quad (1.3)$$



where $X(T)$ is normalized crystallinity at temperature T , K_O is crystallization rate, and ϕ is cooling rate,

Ziabicki model

$$\frac{dX(t)}{dt} = K_Z(T)[1 - X(t)] \quad (1.4)$$

where $K_Z(T)$ is crystallization rate described by a Gaussian function of following from

$$K_Z(T) = K_{Z,\max} \exp\left[-4 \ln 2 \frac{(T - T_{\max})^2}{D^2}\right] \quad (1.5)$$

where T_{\max} is the temperature at which the crystallization rate is maximum, $K_{Z,\max}$ is crystallization at T_{\max} , D is the width at half-height determined from the function of crystallization rate, and is also proposed the kinetic crystallization ability of the semi-crystalline polymer

$$G = \int_{T_g}^{T_m^0} K(T) dT = \frac{1}{2} \left(\frac{\pi}{\ln 2} \right)^{0.5} K_{\max} D \quad (1.6a)$$

$$G_c = \frac{G}{\phi} \quad (1.6b)$$



The exponent of Avrami and Ozawa model summarizes in **Table 1.3**, and the results of Ziabicki model in **Table 1.4ab**. From Avrami model, the n_A value decrease with increasing cooling rate (from 4 to 3), which indicated the nucleation mechanism transition from a thermal to an athermal model. [36] From modified Avrami model, the n_A value was reported to be a constant[42]. Besides, the T_{\max} value decrease with increasing cooling rate, and D value increase with increasing cooling rate[43, 44]. These analysis results conclude that the crystallization rate increases with increasing cooling rate.

Table 1.2 Summary of Avrami exponent in isothermal process.

Temperature region	Avrami exponent, n	Reference
<i>Primary crystallization</i>		
328~348K(cold crystallization)	~5	[36]
443~485K	2~3	[36]
448~468K	2.6~3.8	[45]
450~480K	2.5~3	[39]
453~475K	~2	[40]
475~503K	2.7~2.84	[34]
<i>Secondary crystallization</i>		
450~480K	~1	[39]

Table 1.3 Summary of model's exponent in non-isothermal process.

Cooling rate	Exponent	Reference
<i>Avrami model</i>		
0.63~ 20K/min	1.9~3.7	[40]
5~25K/min	4 ~ 3.3	[41]
<i>modified Avrami model</i>		
5~30K/min	4.4~4.7	[42]
<i>Ozawa model</i>		
0.63~ 20K/min	1.9~3.7	[40]
5~25K/min	--	[41]
5~30K/min	2.4~4.37	[42]

Table 1.4a The kinetic crystallizability of non-isothermal process analysis by Ziabicki model[44].

ϕ (K/min)	D	K_{\max}	G_c
5	7.6	0.75	1.21
10	8.2	1.12	0.98
20	8.9	1.94	0.92
30	9.3	3.24	1.13
40	10.6	3.58	1.01
average			1.05

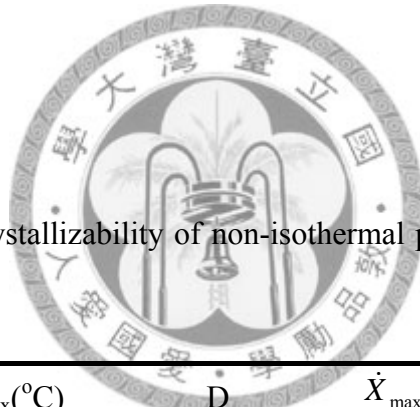
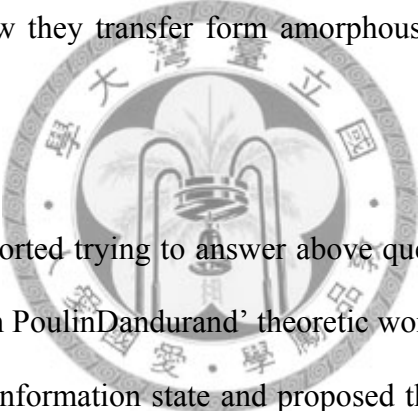


Table 1.4b The kinetic crystallizability of non-isothermal process analysis by Ziabicki model[43].

ϕ (K/min)	T_{\max} (°C)	D	\dot{X}_{\max} ($\times 10^2$)	G_c
5	185.82	9.84	1.05	1.31
10	178.63	11.52	1.91	1.41
15	173.45	19.66	2.23	1.86
20	170.27	18.37	2.99	1.75
30	163.90	20.36	3.26	1.41
40	158.53	24.99	3.67	1.46
50	152.33	28.46	3.63	1.32
average				1.50

1.5 The transition of conformation during crystallization

The drawing process which would rapidly enhance the crystallization by ordering the polymer segments have been introduced in the previous section. Many researchers are interested in changing the conformation of PTT polymer during the drawing or spinning process. In particular, they focus on the torsion angles of the propylene glycol segments (O-CH₂-CH₂-CH₂-O). The crystal lattice of the PTT has been studied by Desborough[26] and Poulindandurand [25]. They both reported that the distribution of the torsion angle of the O-CH₂-CH₂-CH₂-O segment is *tans-gauche-gauche-trans* (t-g-g-t) in the crystalline state. However, what the torsion angle distribution in amorphous state is and how they transfer form amorphous to crystalline state remain unclear.



Many papers were reported trying to answer above questions, but the results were not very consistent. Base on PoulinDandurand' theoretic work [25], Kim [16] calculated the energy level of each conformation state and proposed that the *g-t-t-g* conformation is much more populous in the amorphous region than *t-t-t-t* is. In contrast, Ohtaki[46] argued that the conformation is random in amorphous state. Jeong[19] reported the content of the gauche state of ϕ_2 (See **Figure 1.3**) to be 33.4% in fully amorphous state, which is estimated by the ratio of the infrared intensity of the gauche and trans conformer.

The mechanism of the conformation transition from amorphous to crystal phase has also been studied using IR spectroscopy, X-ray scattering, and ¹³C solid-state NMR. From IR spectroscopy, which is the most popular method, some bands have been

identified to reflect the torsional state of propylene glycol segments during crystallization process. However, we found that the bands corresponding in phase and conformer are not very consistent from researchers' identifications, although the assignment for each band agreed with each other. We summarize those bands and their relation with phase and conformer in **Table 1.5**. By comparing the IR spectroscopy of the pure crystalline phase and amorphous phase, Kim's group reported that the transition of the torsion angle is from *gttg* to *tggt* [16] during cold-crystallization. This process almost stops below 80°C.[17] Murase's group reported similar results in which the ϕ_2 conformation is from *tt* to *gg* when the polymer is subjected to a long annealing time[46]. On the other hand, the conformational dynamics was investigated during drawing process. Chuah's group[28], Kim's group[17], Jeong[19], and Murase's group[46] all reported that the ϕ_2 conformation is from *tt* to *gg* accompanying the draw ratio. Further, Chuah and Jeong both proposed the linear relationship between the gauche content of ϕ_2 and crystallinity during stress-induced crystallization. Besides, Chuah's group[47] reported the fiber conformation changes from *tggt* to *tttt* at high drawing speeds and some specific temperature by using X-ray scattering to observe the unit cell length of the crystal structure. Murase's group[48] reported the conformation which only focus on ϕ_1 , however, changes from *trans* to *gauche* in half and remains in other half during drawing process by using ^{13}C NMR technique.

Above all, in crystal state, the ϕ_2 conformation exists largely in the *gauche* state, and the ϕ_1 conformation exists largely in the *trans* state; in amorphous state, the ϕ_2 conformation exists mostly in the *trans* state, but the ϕ_1 conformation is unclear. Moreover, the transition during annealing process, the ϕ_2 conformation changes from *trans* state to *gauche* state but ϕ_1 conformation is unclear; the transition during drawing

process, the ϕ_2 conformation changes from *trans* state to *gauche* state, if polymer chains undergo sufficient thermal relaxation; however, the ϕ_1 conformation is unclear.

Table 1.5 The identification of IR bands corresponding with propylene glycol segments.

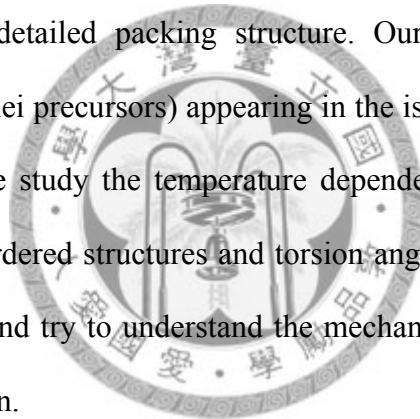
Band	Assignment	Phase	Conformer type
811	CH ₂ rocking[28, 49]	amorphous[19, 28]	trans [19, 28]
933	CH ₂ rocking[28, 49, 50]	crystal[16, 19, 28] Amorphous[50]	gauche [19, 28]
1037	CC stretch[16, 28, 46]	Amorphous[16] Crystal[28, 46]	gauche[16, 46]
1043	CC stretch[16, 49, 50]	crystal[16, 49, 50]	gauche [16] [49]]
1358	CH ₂ wagging [16-18, 28, 46, 49, 50]	Crystal [16-19, 28, 46, 49, 50]	trans [18] gauche [28, 46]
1385	CH ₂ wagging [17, 18, 28, 46, 49, 50]	crystal[49, 50] amorphous[17, 18, 28, 46]	gauche [18] trans [28, 46]
1471	CH banding[16, 17, 49, 50]	crystal[16, 17, 19, 49, 50] amorphous[16]	

1.6 Motivation

While experimental and theoretical efforts are made to verify and explain the molecular mechanism in the growth of nuclei in polymeric materials, the primary stage of polymer crystallization is less well understood. In experiment, the crystallization of the polymer has been studied by isothermal, non-isothermal, and stress-induced processes, and establishes the knowledge of the kinetics behaviors, the phenomena of the early ordering structure, and orientation crystallization behaviors. The molecular mechanism of the crystallization, however, seems difficult to study experimentally. On the other hand, most of simulation works in crystallization are only based on simple

linear polymer (PE). Furthermore, in order to reduce the simulation time, coarse-grained or bead-spring models are used. Such models overlook the atomistic details of the polymers so that detailed change in chain conformation could not be observed. It could potentially lead to discrepancies found between in some properties between simulations and experiment.

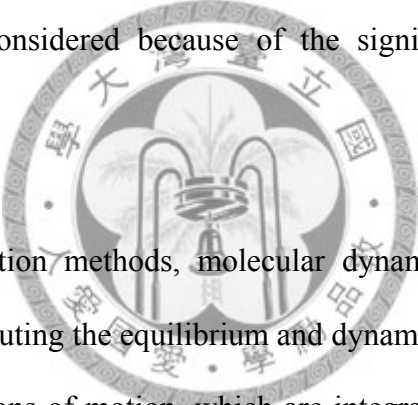
In this work, we use fully atomistic models to simulation the crystallization process of poly(trimethylene terephthalate), PTT. Unlike coarse-grained or bead-spring models that are more often adopted in simulation for crystallization process of polymers[12-15, 51], atomistic molecular models, while more computational demanding, provide a much better resolution on the detailed packing structure. Our simulations focus on the ordering of structures (nuclei precursors) appearing in the isothermal and stress-induced crystallization process. We study the temperature dependence of the amount of such clusters, the behavior of ordered structures and torsion angle transition during drawing and annealing processes, and try to understand the mechanism of the nucleation at the early stage of crystallization.



2 Theory

2.1 Molecular dynamic simulation

Recently, computer simulations have come to be recognized as a powerful and promising tool to investigate the molecular process of polymer crystallization. A polymeric system contains a large number of atoms, and the motion of atoms exist large degrees of freedom. The large degrees of freedom increase the difficulty to understand the relationship between the properties and motion of atoms. Some simplified polymer models have been proposed to describe the general behaviors of polymer. Now, more realistic models can be considered because of the significant advancement in the computation power.



Among of all simulation methods, molecular dynamic simulation is the most popular technique for computing the equilibrium and dynamic properties. The method is solution of classical equations of motion, which are integrated numerically to give the information on the positions and velocities of the atoms in the system. The net forces on each atom are calculated by the differentiation of the potential energy.

2.2 Algorithm

There are some algorithms used in the molecular dynamics simulation to solve for the equations of motion. In this work, Verlet method is used in all simulation. The initial form of the Verlet equations is obtained by utilizing a Taylor expansion of the position at time $t + \Delta t$ and $t - \Delta t$

$$\bar{r}_i(t + \Delta t) = \bar{r}_i(t) + \bar{v}_i(t)\Delta t + \frac{1}{2!} \frac{\bar{f}_i(t)}{m_i} \Delta t^2 + \frac{1}{3!} \bar{r}_i^{(3)}(t) \Delta t^3 + o(\Delta t^4) \quad (2.1)$$

$$\bar{r}_i(t - \Delta t) = \bar{r}_i(t) - \bar{v}_i(t)\Delta t + \frac{1}{2!} \frac{\bar{f}_i(t)}{m_i} \Delta t^2 - \frac{1}{3!} \bar{r}_i^{(3)}(t) \Delta t^3 + o(\Delta t^4) \quad (2.2)$$

where $\bar{f}_i(t)$ is the net force applying on the i atom at time t , m_i is the mass of the i atom. Summing the two equations gives

$$\bar{r}_i(t + \Delta t) = 2\bar{r}_i(t) - \bar{r}_i(t - \Delta t) + \frac{\bar{f}_i(t)}{m_i} \Delta t^2 + o(\Delta t^4) \quad (2.3)$$

and subtracting the two equations gives

$$\bar{v}_i(t) = \frac{\bar{r}_i(t + \Delta t) - \bar{r}_i(t - \Delta t)}{2\Delta t} + o(\Delta t^2) \quad (2.4)$$

Above can give the position (**equation. 2.3**) and velocity (**equation. 2.4**) of each atom at each simulation time.

2.3 Force field

Forces resulting from atomic interactions are in the above algorithm. The concept of calculation is

$$-\frac{\partial U(t)}{\partial \bar{r}_i} = \bar{f}_i(t) = m_i \frac{d^2 \bar{r}_i(t)}{dt^2} \quad (2.5)$$

where $U(t)$ is the overall potential energy at time t . The potential energy is the summation of the valence types (bond, angle, torsion, and inversion energy) and non-bond types (coulomb and van der waals interaction). In this work, we chose Dreiding[52] force field whose general forms are described below.

2.3.1 Bond energy

The bond energy is described by harmonic style as following

$$U_b = \frac{1}{2} K_b (R - R_0)^2 \quad (2.6)$$

where K_b is constant, and R_0 is equilibrium length of bond. The parameters of the bond stretch are shown in **Table A.2**.



2.3.2 Angle energy

The angle energy is described by cosine harmonic style as following

$$U_\theta = \frac{1}{2} K_\theta (\cos \theta - \cos \theta_0)^2 \quad (2.7)$$

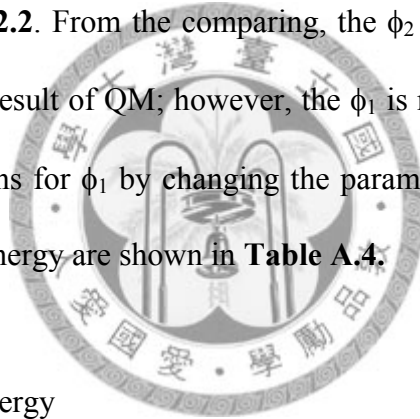
where K_θ is parameter of energy barrier, and θ_0 is equilibrium band angle. The parameters of the angle energy are shown in **Table A.3**.

2.3.3 Torsion energy

The torsion energy is described by harmonic style as following

$$U_{\varphi} = \sum_{n=1}^p \frac{1}{2} K_{\varphi_n} [(1 + d \cos(n\varphi))] \quad (2.8)$$

where K_{φ} is parameter of energy barrier, n is number of periods, d is +1 or -1, and φ is the torsion angle period. The torsion terms of the propylene glycol segment (O-CH₂-CH₂-CH₂-O) being modified to better reproduce quantum mechanics (QM) results. **Figure 2.1** is the energy barrier results of rotating torsion angles, and the modification is in **Figure 2.2**. From the comparing, the ϕ_2 the result of Dreiding force field agrees well with the result of QM; however, the ϕ_1 is not. We try to reproduce the shape from QM calculations for ϕ_1 by changing the parameters of torsion energy. The parameters of the torsion energy are shown in **Table A.4**.



2.3.4 Inversion energy

The inversion energy is described by harmonic style as following

$$U_{\psi} = \frac{1}{2} K_{\psi} (\psi - \psi_0)^2 \quad (2.9)$$

where K_{ψ} is constant, and ψ_0 is equilibrium inversion angle. The parameters of the inversion energy are shown in **Table A.5**.

2.3.5 Coulomb interaction

The coulomb interaction is calculated by the following formula

$$U_R = \frac{Q_i Q_j}{4\pi\epsilon_0 R_{ij}} \quad (2.10)$$

Atomic (Mulliken) charges Q_i are determined from density functional theory (DFT) calculations for the monomer of PTT using the B3LYP functional[53-55] and 6-31G** basis set[56] in Gaussian 98[57]. The method of Particle-Particle/Particle-Mesh (PPPM) Ewald sum[58, 59] is applied for long range interactions in periodic systems.

2.3.6 Van der Waals interaction

The exponential-6 form is calculated inner the distance of the r_i , using the scaling factor, S , to zero value from r_i to r_o . The value of the r_i is 12Å and r_o is 15Å in all calculation. The parameters of the van der Waals interaction are shown in **Table A.6**.

$$\begin{aligned}
 U_{vdW} &= D_0 \left\{ \frac{6}{\zeta - 6} e^{\zeta(1 - \frac{R_{ij}}{R_0})} - \frac{\zeta}{\zeta - 6} \left(\frac{R_0}{R_{ij}}\right)^6 \right\} \quad r < r_i \\
 &= S * D_0 \left\{ \frac{6}{\zeta - 6} e^{\zeta(1 - \frac{R_{ij}}{R_0})} - \frac{\zeta}{\zeta - 6} \left(\frac{R_0}{R_{ij}}\right)^6 \right\} \quad r_i < r < r_o \\
 &= 0 \quad r_o < r
 \end{aligned} \quad (2.11a)$$

$$S = \frac{(r_o^2 - r^2)^2 (r_o + 2r - 3r_i)}{(r_o^2 - r_i^2)^3} \quad (2.11b)$$

where D_o is the deep of the energy well, R_o is the distance of the minima interaction, and ζ is the constant, which the unit is distance. (All the value of parameters are in Appendix A)

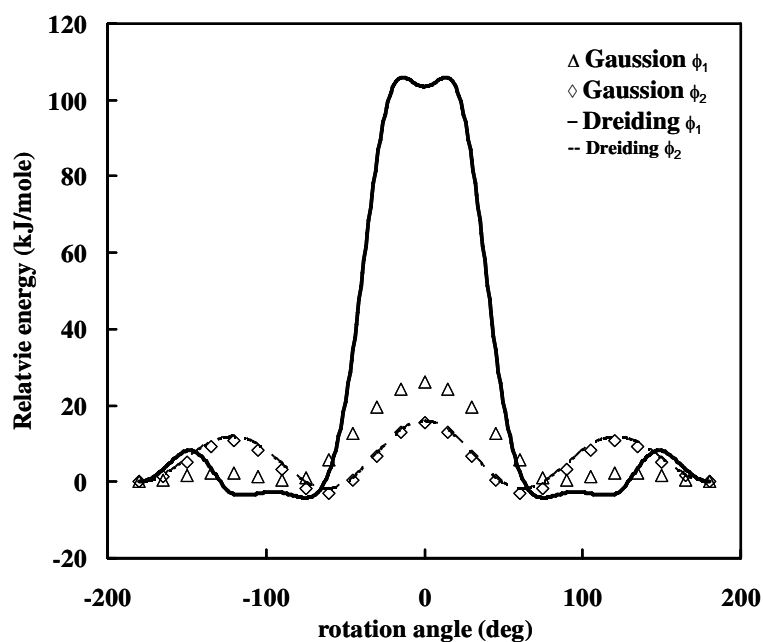


Figure 2.1 Comparison the energy barriers distribution with rotating torsion angles. Check the results of dreiding force field in ϕ_1 (solid line), and ϕ_2 (dash line) against that of quantum mechanics using the B3LYP functional and 6-31G** basis set in Gaussian 98 in ϕ_1 (triangle), and ϕ_2 (diamond).

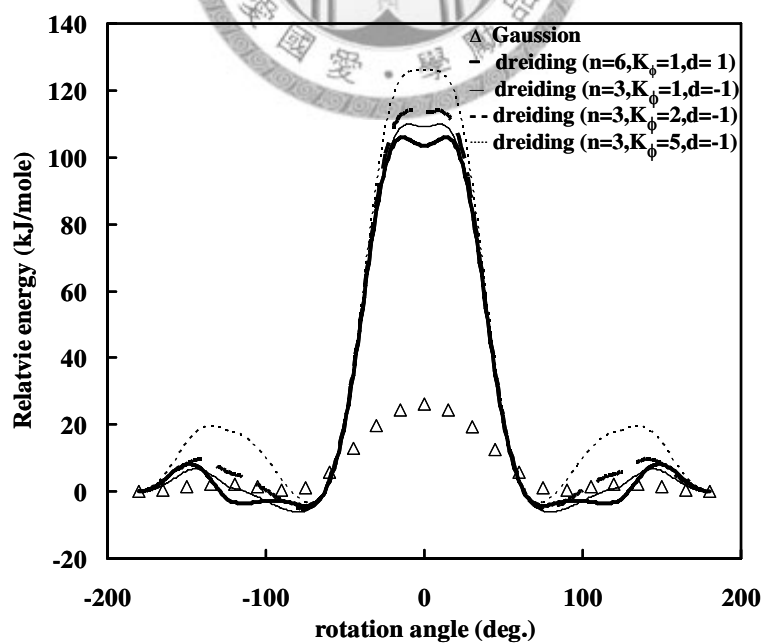


Figure 2.2 Modification the energy barriers distribution with rotating torsion angle of ϕ_1 . Accept the result of parameter $n = 3$, $K = 2$, and $d = -1$ to use in torsion energy.

2.4 Thermal behavior

2.4.1 Glass transition temperature

Crystalline polymers may phase change to morphologies-crystalline and glassy state, flexible thermoplastic state, and liquid state (ordered liquid state in liquid crystalline polymer before melting) upon increasing of temperature. The transition point between crystalline and glassy state and flexible thermoplastic state is known as the glass transition temperature (T_g). From experimental observation, the properties of volume (density), enthalpy, storage shear modulus (**Figure 2.3**), and young's modulus (**Figure 2.4**) show an obvious change at T_g . From the viewpoint of the motion of atom, only few (1 to 4) atoms are involved in motions below T_g , while more (10 to 50) atoms (smaller than entanglement region) gain sufficient thermal energy to move in a coordinated manner in the glass transition region. In our simulation, we analyze the density change of purely amorphous sample during heating and cooling to find the second-order transitive point which identify as T_g point.

2.4.2 Melting temperature

The melting behavior of the polymer is the process of the crystalline fusion, which is a first-order transition. In experiment, the melting temperature is found to be a region (rather than a point) and with its width depending on the heating rate. In our simulation, we analyze the density change of purely amorphous sample during heating process to find the volume (density) change as shown in **Figure 2.5**.

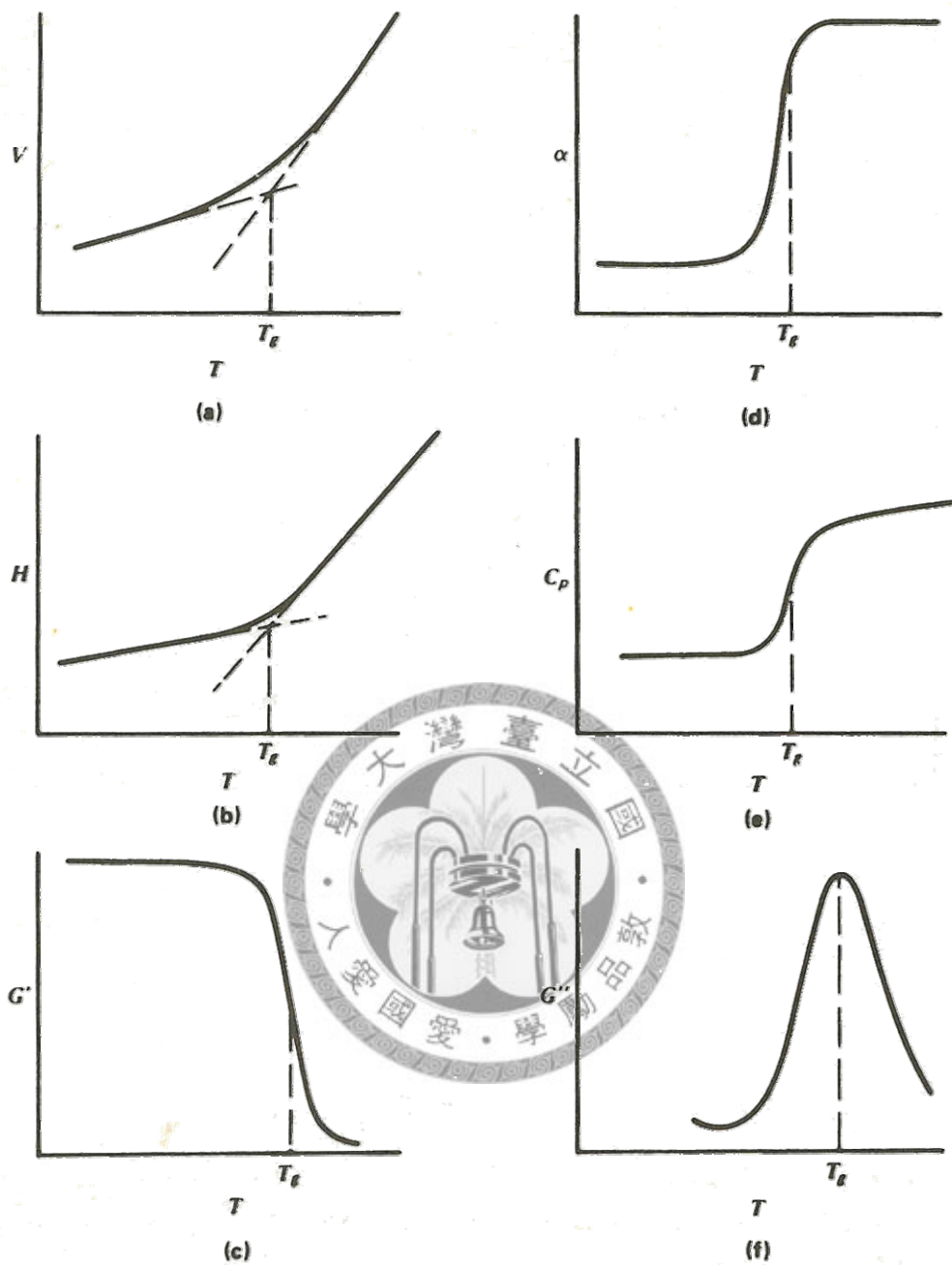


Figure 2.3 General variations in (a) volume, V , (b) enthalpy, H , and (c) storage shear modulus, G' as function of temperature. Also show (d) volume expansion coefficient, α , and (e) heat capacity, C_p , which is the first derivation of V and H , respectively with respect to temperature, and (f) the loss shear modulus, G'' . [2]

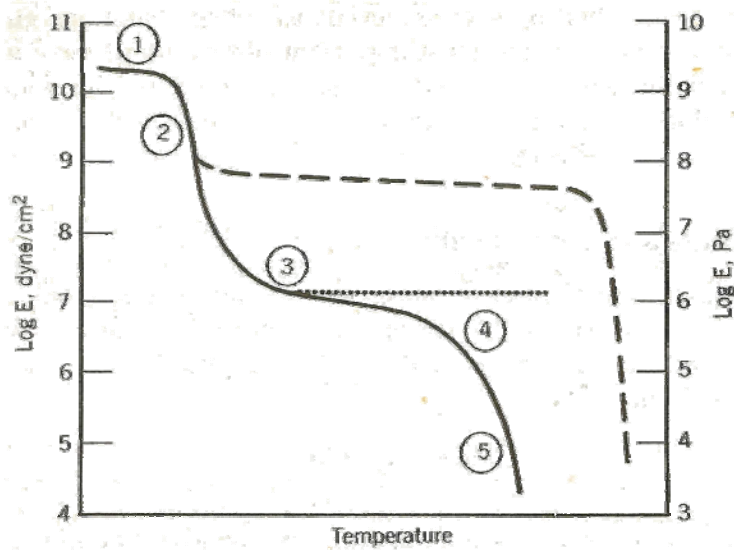


Figure 2.4 The viscoelastic behavior of amorphous polymer (solid line), crystalline polymer (dashed line), and cross-linking polymer (dotted line) as function of temperature. There are five regions shown as (1) glassy region, (2) glass transition region, (3) rubbery plateau region, (4) rubbery flow region, and (5) liquid flow region.[2]

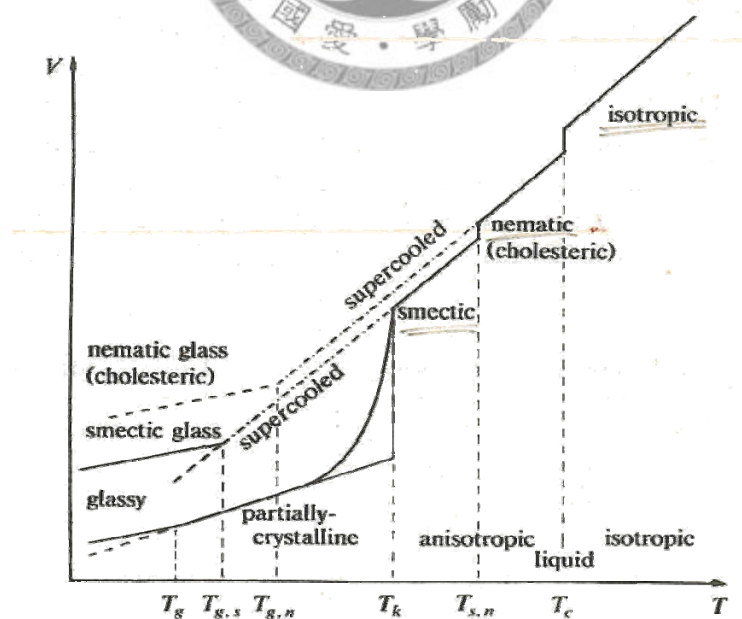


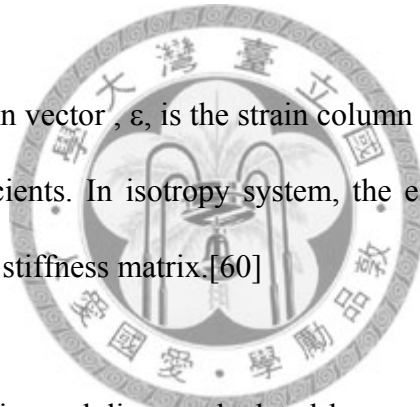
Figure 2.5 The volume profile with temperature of the polymer.[2]

2.5 Mechanical properties

Elastic moduli (Young's modulus, E , bulk modulus, B , shear modulus, G) are the common index of mechanic strength of the solid material. The deformation of polymer by application of stress depends on the atomic structure. (See T_g modulus behavior) Form elastic deformation, the relationship between the stress, σ , and strain, ε , can be expressed by a generalized Hooke's law which is simplified by engineering strains assumption as following

$$\sigma = C\varepsilon \quad (2.12)$$

where σ is the stress column vector, ε , is the strain column vector and C is the tensor of the elastic stiffness coefficients. In isotropy system, the elastic moduli and Poisson's ratio, ν , can be estimate by stiffness matrix.[60]



In experimental, elastic moduli are calculated by measuring the deformation and stress form tensile test. In simulation, the *tensile test* method was proposed[61-64] to estimate the Young's modulus. The method like, experiment, uniaxially deforms the system during molecular dynamic simulation. The computer program LAMMPS[65] used throughout this work allows only orthorhombic systems. Therefore only Young's modulus and Poisson's ratio (but not the shear modulus) at different temperature were determined. In our analysis, independent processes of $\pm 6\%$ deformation were applied to the simulation box at three directions and the Young's modulus is determined from the slope of the strain-stress curve.

2.6 Definition of the segment packing structure (precursor structure)

To detect and quantify any structural development, we define the nucleus precursors in the system as follows:

- (1) A segment of PTT is defined to be the vector pointing from the center of an aromatic ring to the next aromatic ring on the same polymer chain (green cylinders in **Figure 1.3b**).
- (2) Adjacent segments are defined as those whose separation distance between centers of mass falls within 9 Å.
- (3) Two adjacent segments whose included angles are within 10 degrees are marked as mutually parallel.
- (4) A nucleus precursor is identified as a cluster containing mutually parallel segments.

A precursor defined by such criteria has an orientationally ordered but loosely packed structure. Based on this definition, we may easily determine the number n_s of nucleus precursors containing s parallel segments at any instant of time in the course of dynamic simulation.

The local ordering within the system during the induction period of the crystallization process can be quantified by the “fraction of precursor”. (Note that we have separately confirmed that the system as a whole remain isotropic at all temperatures, i.e., there is no long-ranged directional preference for the orientation of the precursors as one would expect from quenching.) First, we define the fraction of precursor X_i from precursors of size s as

$$X_s = s \langle n_s \rangle / \left(\sum_{i=1}^{\infty} i \langle n_i \rangle \right) \quad (2.13)$$

where $\langle n_i \rangle$ is the average number of cluster of size i (i.e, the average value of n_i (calculated at every picosecond) over one nanosecond). The total fraction of precursor X is defined as

$$X = \sum_{s=4}^{\infty} X_s \quad (2.14)$$

We have excluded the contributions from $s \leq 3$ because formation of such clusters highly depends on segment collisions and the value of average number $\langle n_s \rangle$ is almost time invariant at a given temperature.

2.7 Definition of the torsion angle state

In order to study the change of the propylene glycol segments (O-CH₂-CH₂-CH₂-O) conformation of PTT, we need to define the conformation states of the torsional angle. In our analysis, we consider a torsion to be in the trans state if its angle ranges between (165° ~ 180° and -165° ~ -180°) and in the gauche state between (45° ~ 75° and -45° ~ -75°).

2.8 Other properties

2.8.1 Radial distribution function

Radial distribution function (RDF), $g(r)$, describes how the density of surrounding matter varies as a function of the distance from a distinguished point. Suppose, for example, that we choose a molecule at some point O in the system. RDF is the mean local density at distance from O to mean density of all system ratio:

$$g(r) = \frac{\text{mean local density at distance } r \text{ from O}}{\text{mean density of overall system}} \quad (2.15)$$

As long as the gas is dilute the correlations in the positions of the molecules that $g(r)$ takes into account are due to the potential $\phi(r)$ that a molecule at P feels owing to the presence of a molecule at O. Using the Boltzmann distribution law

$$g(r) = \exp\left(\frac{-\phi(r)}{kT}\right) \quad (2.16)$$

If $\phi(r)$ was zero, the molecules did not exert any influence on each other $g(r) = 1$ for all r . Then from (1) the mean local density would be equal to the mean density ρ : the presence of a molecule at O would not influence the presence or absence of any other molecule and the gas would be ideal. As long as there is a $\phi(r)$ the mean local density will always be different from the mean density ρ due to the interactions between molecules.

2.8.2 Persistence length

The persistence length was determined from the segment vector correlation function

$$\langle \bar{u}(0) \cdot \bar{u}(s) \rangle = e^{-s/P} \quad (2.17)$$

where $\bar{u}(s)$ is unit vector of s segment, and P is persistence length [66].

2.8.3 Orientation factor

Orientation factor, f , is an index of the orientational ordering of segments in the system. From the IR spectra, it can be given by dichroic ratio

$$f = \frac{(D-1)(D_0+2)}{(D+2)(D_0-1)} \quad (2.18)$$

where $D_0 = 2\cot^2\alpha_v$ is the dichroic ratio of an ideally oriented polymer with perfect alignment of its molecules parallel to the fiber axis (α_v is transition moment angle of vibration), and D is measured dichroic ratio. Besides, it also can be given by the intensity of WAXD

$$f = \frac{3\langle \cos^2 \phi_{c,z} \rangle - 1}{2} \quad (2.19)$$

where $\langle \cos^2 \phi_{c,z} \rangle$ equals $1 - 2\langle \cos^2 \phi_{010,z} \rangle$, $\phi_{c,z}$ is the angle between the reference

direction(fiber axis) and the polymer chain, $\phi_{010,z}$ is the angle between the fiber axis and the normal of the crystallographic plane(010), and $\langle \cos^2 \phi_{010,z} \rangle$ value can calculate by integrating the intensity of the WXR.

In our analysis, we consider $\phi_{c,z}$ to be the included angle between the drawing direction and the segments (as defined in **2.6 Definition of the segment packing structure**), similar to the definition above, and then use **equation 2.19** to calculate the orientation factor. When the polymer chains are perfectly oriented parallel and perpendicular to the draw direction, the f value equals to 1 and -0.5, respectively. For randomly distributed segments, the value of f is 0.



3 Computation method and detail

3.1 Method

The nucleation process at early state of crystallization is studied using molecular dynamics (MD) simulations. The object is to understand the mechanism of formation of nuclei precursors by monitoring the development of ordering structures. The PTT monomer and polymer 3D structure unit are created with commercial software Cerius²[67]. Amorphous, semi-crystalline and purely crystalline structures were created. Each system contains about two thousands and seven hundreds atoms in one unit cell. As a validation of the use of Dreiding, we compare some physical properties from our simulation to experiment. Then, the systems undergo equilibration process in order to reach a more stable system conformation. Molecular dynamics simulations at constant T and P are then performed using an open-source program: Large-scale Atomic/Molecular Massively Parallel Simulation (LAMMPS)[65]. Finally, the results are analyzed by our own program. (See the flowchart **Figure 3.1**) The simulations presented in this work amounts to 1×10^5 CPU hours on one Intel Xeon 3.0 GHz processor.

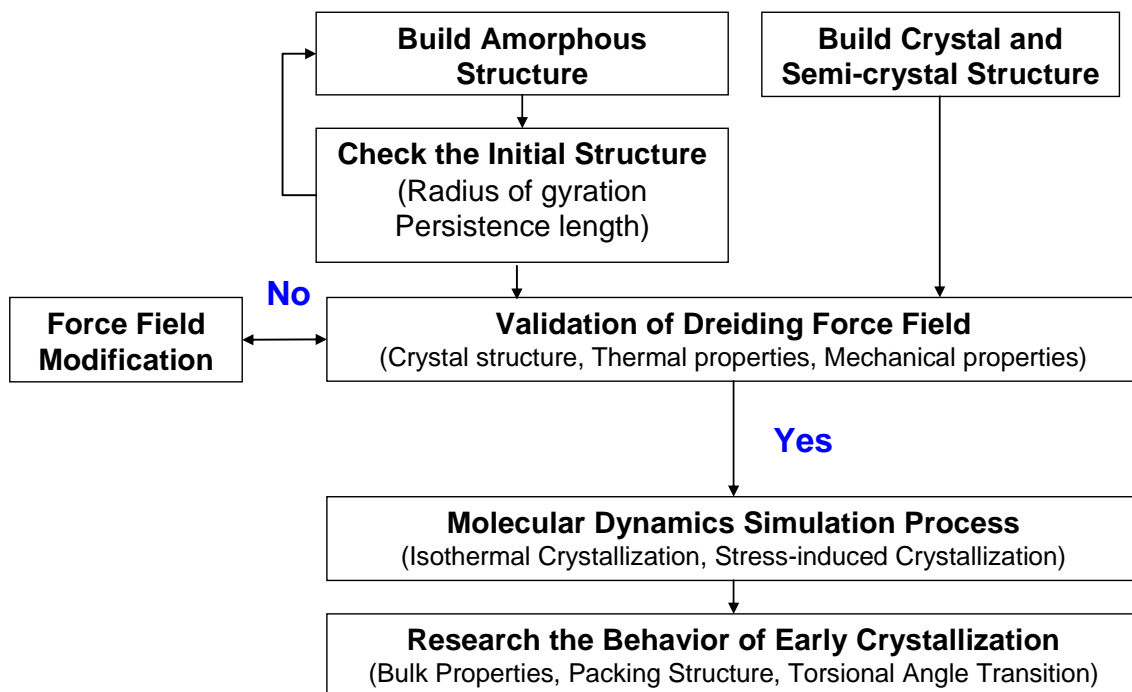
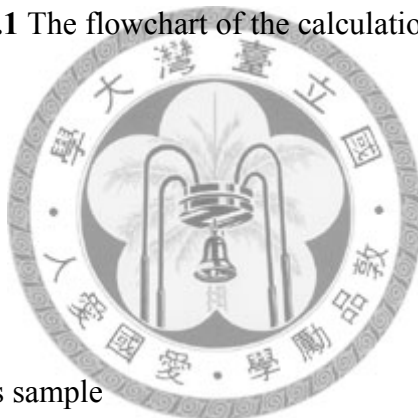


Figure 3.1 The flowchart of the calculation process.



3.2 Model building

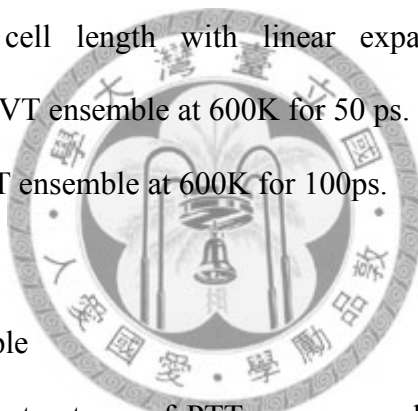
3.2.1 Amorphous sample

The initial amorphous structures of PTT are prepared using the Amorphous Builders module implemented in commercial package Cerius². The persistence length in random coil (~ 4.5 Å), is smaller than that in RIS model (~ 6 Å). **Figure 3.2** shows the radius of gyration (R_g) of PTT chains as the function of sample size (total number of repeat units) for polymers with degrees of polymerization (DP) of 27, 36, and 48, which is smaller than that in RIS model (26 Å vs. 74 Å with DP = 27). Note: R_g is independent on chains) (Note that the entanglement molecular weight of PTT was determined to be 4900 to 5000 g/mol[29, 68] corresponding to a degree of polymerization of 24). In this study, two system sizes are used: (1) small systems consist of 4 chains with DP=27, and (2) large systems consist of 8 chains with DP=27. For small systems, the simulation box

contains 108 repeating units of PTT, or equivalently 2708 atoms. The density is set 1.30 g/cc, and three dimension periodic boundaries are used. The structure of each sample is optimized by energy minimize. Then, the sample undergoes a series of expansion-compression equilibrium process at 600K, as detailed below

(**Figure 3.3** shows a sample amorphous system.)

- (1) Expansion to 125% of the initial cell length with linear expansion rate in three axes simultaneously using NVT ensemble at 600K for 60 ps.
- (2) Compression to 95% of the initial cell length with linear compression rate in three axes simultaneously using NVT ensemble at 600K for 100 ps.
- (3) Expansion to initial cell length with linear expansion rate in three axes simultaneously using NVT ensemble at 600K for 50 ps.
- (4) Equilibration using NPT ensemble at 600K for 100ps.



3.2.2 Crystal sample

The initial crystalline structures of PTT are prepared using the Crystal Builders module implemented in commercial package Cerius². A superlattice is first created from 2x2x2 crystalline unit cells of PTT. A crystalline model, with a density of 1.42 g/cc, contains 4 PTT chains, each having 4 repeat units. The structure of each sample is energy minimized. The crystal sample is considered as reference state of many analyses in this work. A sample crystalline structure is shown in **Figure 3.4**.

3.2.3 Semi-crystal sample

The initial semi-crystal structures of PTT are prepared in two steps: the crystalline structure is created first, and then amorphous phase is added with crystalline phase fixed.

The crystal structures which contain 25 chains of PTT molecule, each having a degree of polymerization of 4. The structure of each sample is optimized by energy minimize with compressing volume to 1.47 g/cc, and three dimension periodic boundaries are used. Then, the sample undergoes expansion-compression equilibrium process at 600K with 88%, 50%, and 18% amounts of fixed atoms in the crystalline region. Finally, the samples equilibrate at 200K. The semi-crystal samples are used to determine the melting behavior in this work. **Figure 3.5** shows a sample of semi-crystalline structure.

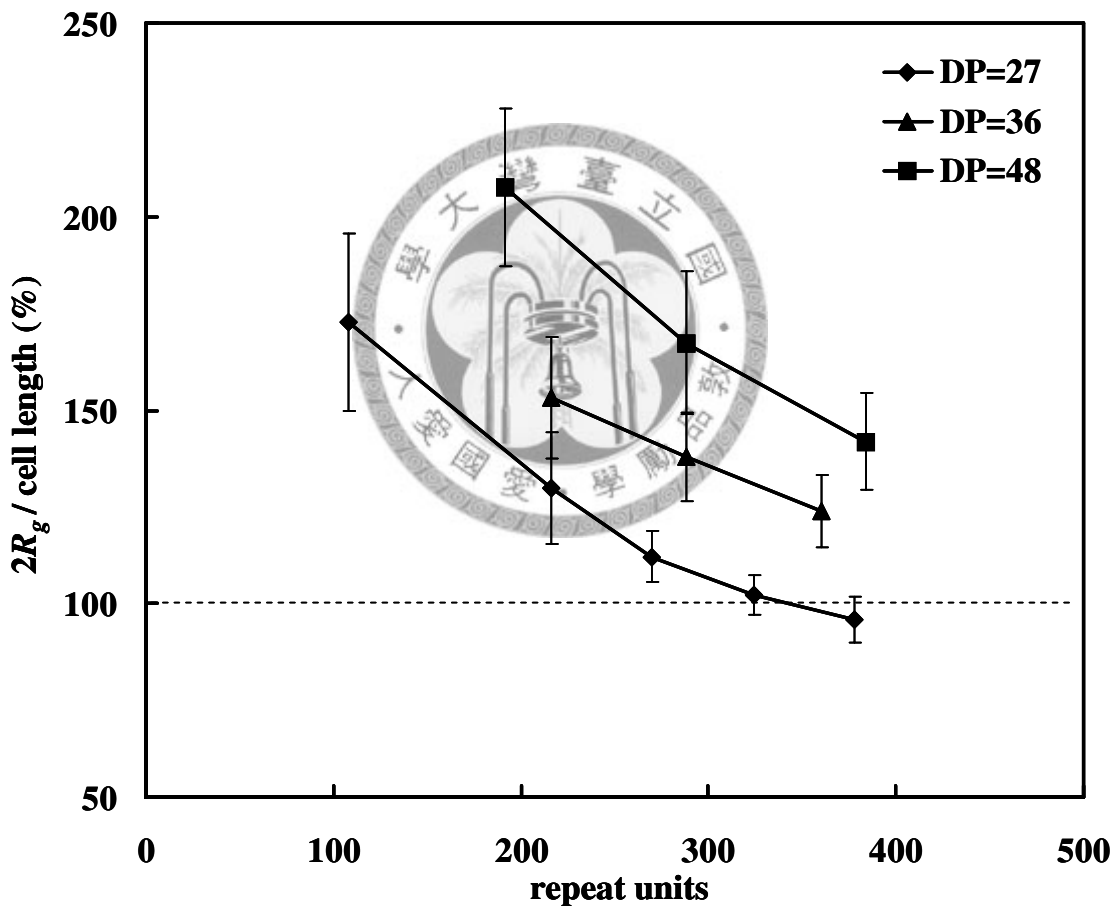


Figure 3.2 The radius of gyration (R_g) of PTT chains as the function of repeat units.

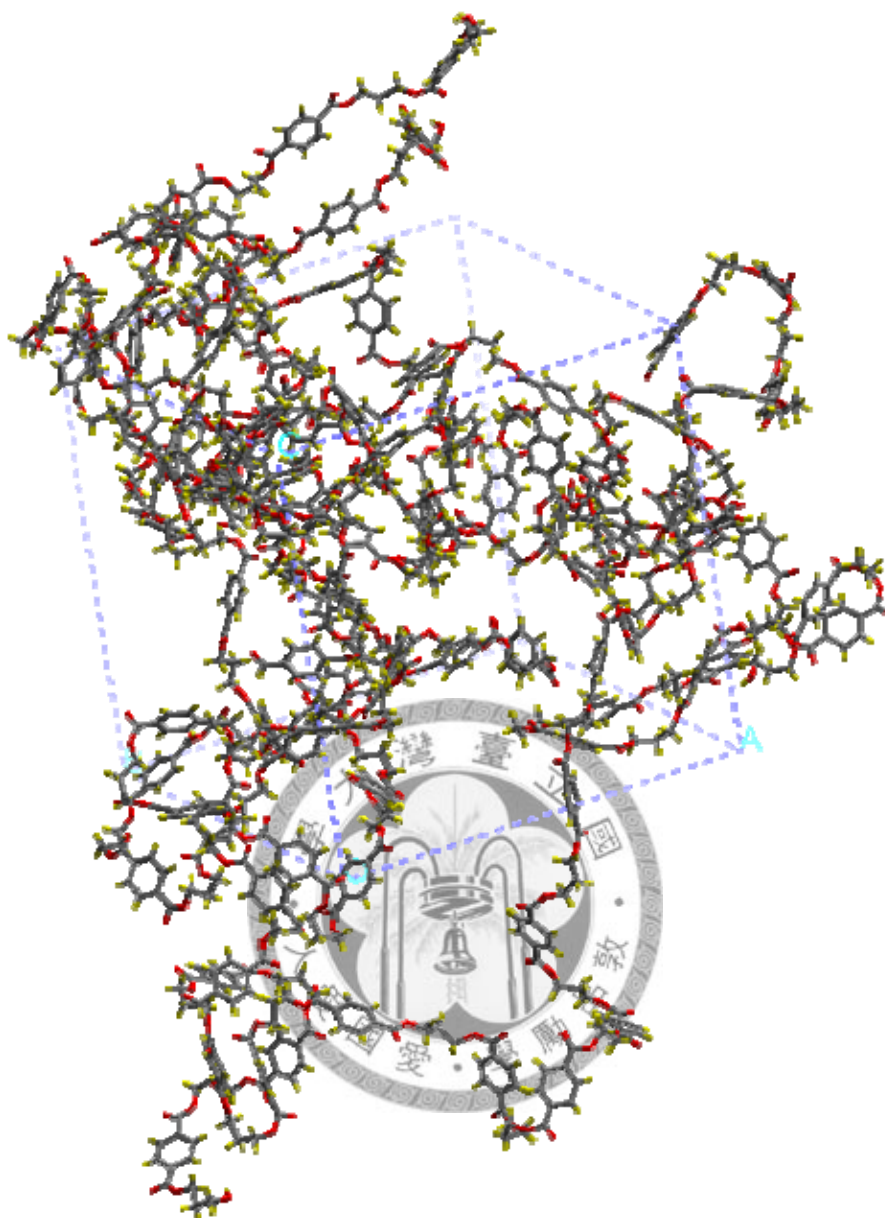


Figure 3.3 An amorphous structure at 600K. The system contains 4 chains of PTT molecules, each having a degree of polymerization of 27 overall 2708 atoms. The cell parameter: $a = 31.93\text{\AA}$, $b = 31.93\text{\AA}$, $c = 31.93\text{\AA}$, $\alpha = 90.00(\text{deg})$, $\beta = 90.00(\text{deg})$, $\gamma = 90.00(\text{deg})$, and density is 1.06 g/cc.

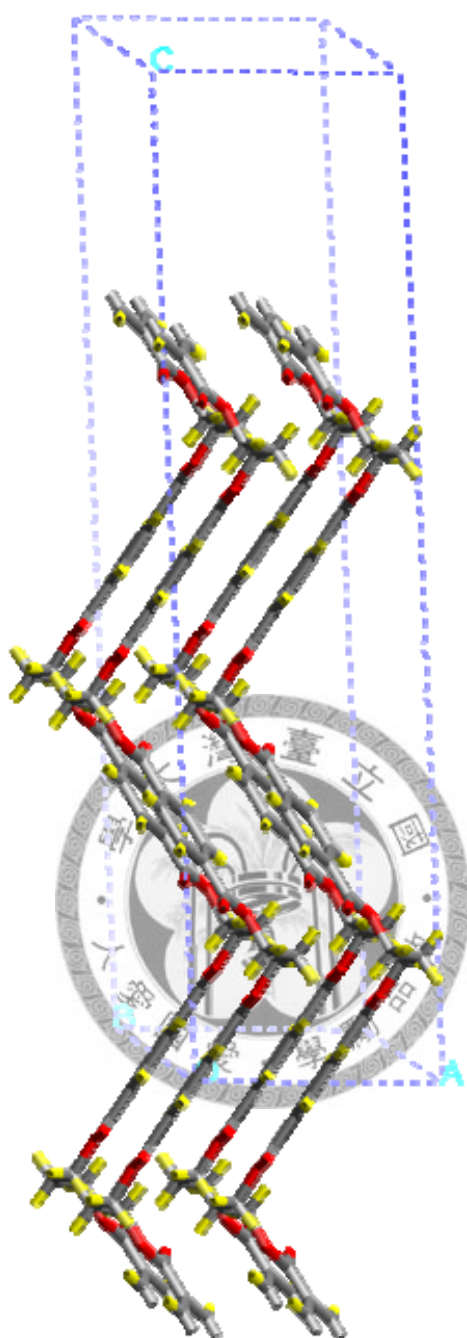


Figure 3.4 A crystalline structure. The model contains 8 (2x2x2) atomic lattice cells, 4 chains of PTT molecules, each having 4 repeat units, overall 400 atoms. The cell parameter: $a = 8.66\text{\AA}$, $b = 12.56\text{\AA}$, $c = 37.39\text{\AA}$, $\alpha = 101.66(\text{deg})$, $\beta = 90.00(\text{deg})$, $\gamma = 110.11(\text{deg})$, and density is 1.47 g/cc.

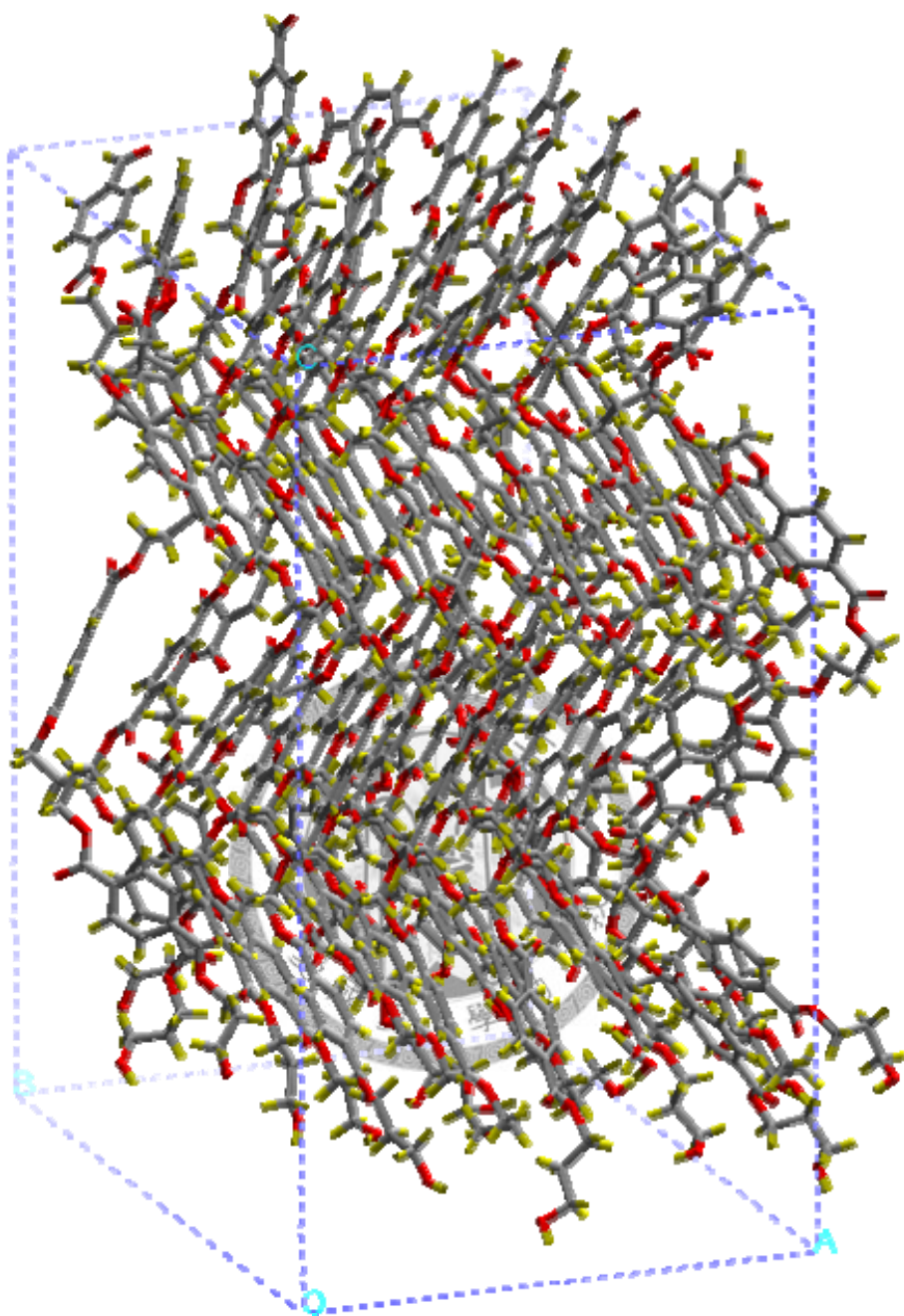


Figure 3.5 An equally semi-crystal structure with $X_c=18\%$. The model contains 25 chains of PTT molecule, each having a degree of polymerization of 4, overall 2550 atoms. The cell parameter: $a = 21.96\text{\AA}$, $b = 31.53\text{\AA}$, $c = 39.35\text{\AA}$, $\alpha = 90.00(\text{deg})$, $\beta = 90.00(\text{deg})$, $\gamma = 90.00(\text{deg})$, and density is 1.33 g/cc.

3.3 Ensemble and control detail

In the amorphous building processes, NPT ensemble (control pressure at 0 bar (the pressure deviation is about 0.1GPa) is used. In crystal building processes, NPT ensemble also is used. In semi-crystal building processes, NVT ensemble is used. On the other hand, the iso-thermal and stress-induced crystallization processes used NPT ensemble with pressure at 0 bar and $NTL_x\sigma_{yy}\sigma_{zz}$ ensemble with zero normal stress in y and z directions[63].

The control of temperature and pressure both use Nose-Hoover thermostat[69, 70], is given by

$$\dot{\bar{f}}_i(t) = -\frac{\partial U(t)}{\partial \bar{r}_i} + (\xi + \chi)\bar{p}_i \quad (3.1a)$$



Where ξ, χ are the fiction coefficients in inverse time unit, and their rate of change depends on the deviation of instantaneous T (or P) form desired T (or P), as equation 3.1b, c

$$\dot{\xi} = \frac{3N}{Q}(k_B T - k_B T_{desired}) \quad (3.1b)$$

$$\dot{\chi} = \frac{(P - P_{desired})V}{t_p^2 k_B T_{desired}} \quad (3.1c)$$

where Q is the thermal inertia parameter, t_p is ,and V is system volume. In LAMMPS,

the frequency of the relaxation of temperature and pressure are need. All of our simulation, the frequency of temperature control is once per 100 fs; the pressure of that is once per 1000 fs.

3.4 Force field validation

The force field is the key to any successful MD simulation. We examine the crystalline structure properties and torsional angles, thermal property, and mechanical properties.

3.4.1 Crystal structure properties and torsional angles

Table 3.1 compares the lattice parameters, torsional angles ($\phi_1, \phi_2, \phi'_1, \phi'_2$ as indicated in **Figure 1.1**), and density of crystalline PTT from simulation and experiment. Results are averaged from MD simulations performed on a PTT crystalline unit cell at 0 bar and 300 K for 300ps. In general, the simulation results are in good agreement with experiment. It is interesting to note that the asymmetric torsional angles ($\phi_1 \neq \phi'_1$, and $\phi_2 \neq \phi'_2$) observed in experiment is also seen in our simulation.

3.4.2 Thermal properties

The melting temperature (T_m), and glass transition temperature (T_g) are determined by examination of the variation of density upon stepwise cooling and/or heating at an effective rate of 1K/1ps. Hysteresis in the density change is observed as shown in **Figure 3.6**. The melting temperature is observed as a region between 550K and 750K by heating the semi-crystal samples, due to the fusion of crystalline phase. (T_m , experimental value is 499~503 K) The glass transition point is observed by cooling and

heating of the amorphous samples and a change of slope at 360 K. These results suggest that the T_g is about 360 K (experimental value is 315~348 K). Besides, we can observe the vaporization between 850K~900K.

3.4.3 Mechanical property

The Young's modulus of PTT, determined from the slope of the stress and strain curve (as shown in **Figure 3.7**) are listed in **Table 3.2**. The calculated elastic constant is a function of the temperature and draw speeds shown as **Figure 3.8**. Young's modulus remains at a high value until temperature rises to 300K. Upon 350K, the value of modulus decreases with increasing temperature. The results indicate that the thermal effect begin to influence the elastic properties above 350K. Moreover, at the highest draw speed ($1 \times 10^{11} \text{s}^{-1}$), the value of modulus is much lower than other speeds. That indicates the rate of void creation would be more quickly than that of the thermal relaxation at such a high draw speed. The calculated Young's modulus at 300K is 2.73 ± 0.53 GPa in good agreement with experimental measurement 2.3~2.8 GPa.

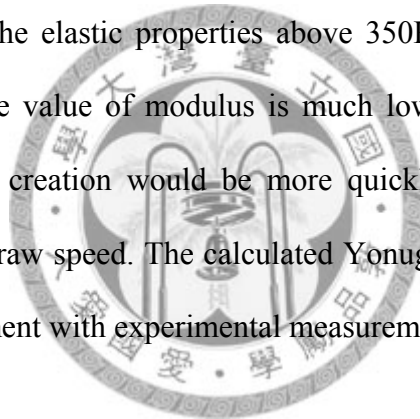


Table 3.1 Comparison of the lattice parameters, density, and torsional angles of crystalline PTT.

	Expt1[26]	Expt2[25]	Expt3[71]	Expt4[71]	Simulat.[33]	MD [†]
a (Å)	4.637	4.59	4.53	4.5	4.50±0.14	4.40±0.05
b (Å)	6.266	6.21	6.20	6.3	6.05±0.18	6.33±0.06
c (Å)	18.46	18.31	18.7	18.2	18.83±0.44	18.84±0.15
α (deg.)	98.4	98.0	97.6	97.5	98.00±1.28	101.7±0.7
β (deg.)	93.0	90.0	93.2	91.4	91.18±1.99	90.0±0.4
γ (deg.)	111.1	111.7	110.1	111.7	111.50±0.57	110.2±1.1
ρ (g/cc)	1.387	1.43	1.408	1.44	--	1.42±0.02
ϕ_1 (deg.)	(±175)	167.4	--	--	--	175.0±4.4
ϕ_2 (deg.)	(±60)	-73.7	--	--	--	-64.8±8.6
ϕ'_2 (deg.)	--	-61.9	--	--	--	-64.7±8.6
ϕ'_1 (deg.)	--	-152.8	--	--	--	-162.7±10.3

[†]Results averaged from MD simulations performed on a PTT crystalline unit cell at 0 bar and 300 K for 300ps.

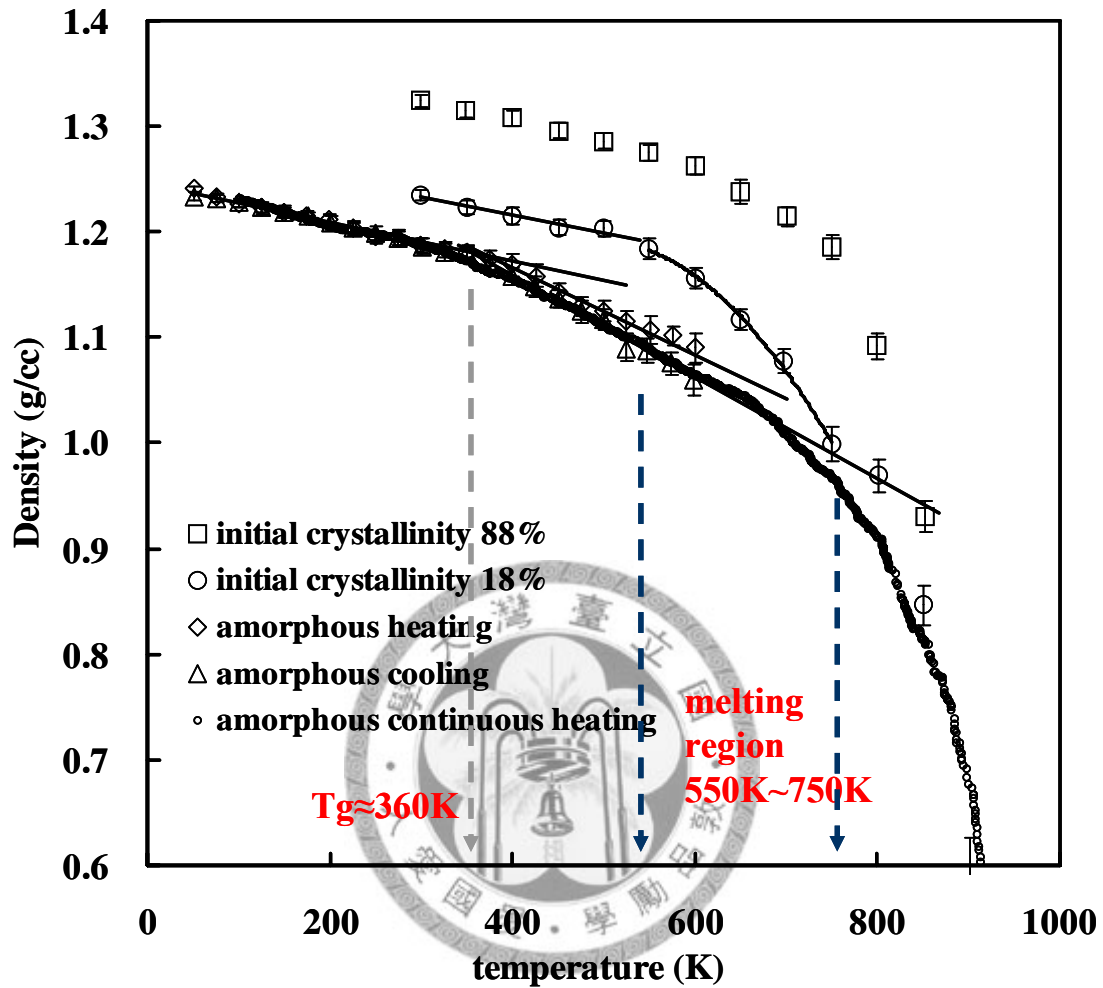


Figure 3.6 The density variation of PTT upon cooling and heating. The 600K equilibrated sample cooled to 50K (open square) and 50K equilibrated sample heated to molten state (open circle). Each process was performed by step changes of temperature of 25K after 25ps.

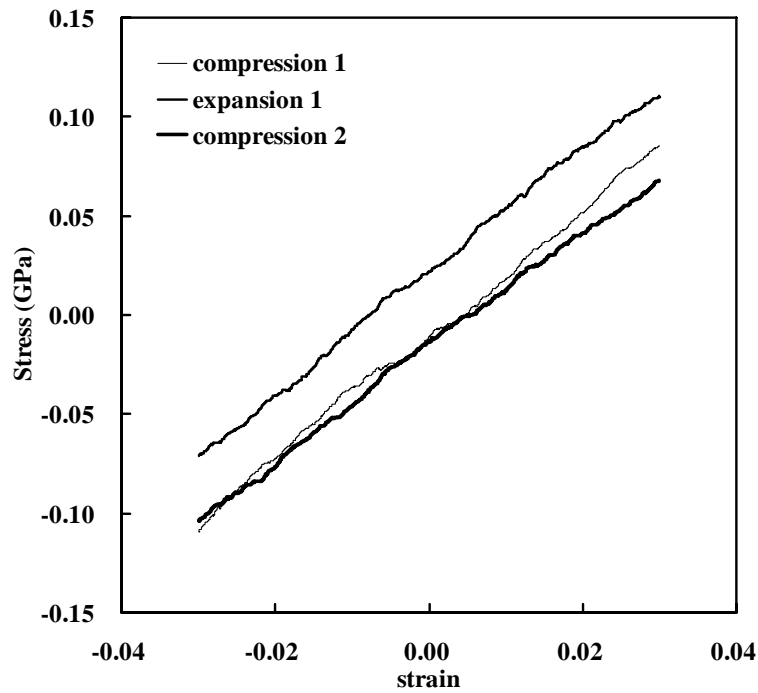


Figure 3.7 The plot of the stress and strain curve. In all case, the slope of three lines is uniform. The technique of black average (3% of stain) used in data analysis results in the data shown form -1.5% to 1.5%. This example is drawn with draw speed $1 \times 10^{10} \text{ s}^{-1}$ in x-direction at 200K.

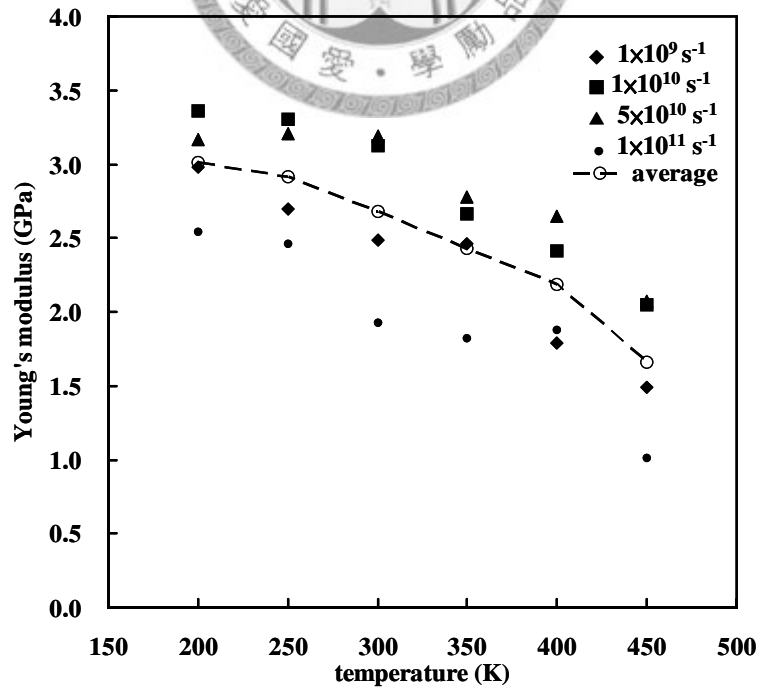


Figure 3.8 The calculated Yonug's modulus is a function of the temperature and draw speeds. The average curve considers all draw speeds.

Table 3.2 Young's modulus of PTT at different condition.

Temperature (K)	Test direction	Draw speeds			
		$1 \times 10^9 \text{ s}^{-1}$	$1 \times 10^{10} \text{ s}^{-1}$	$5 \times 10^{10} \text{ s}^{-1}$	$1 \times 10^{11} \text{ s}^{-1}$
200	x	2.99 ± 0.41	3.25 ± 0.33	2.90 ± 0.88	2.59 ± 0.56
	y	2.97 ± 0.35	3.71 ± 0.63	3.74 ± 0.63	2.87 ± 0.79
	z	2.98 ± 0.15	3.12 ± 0.36	2.87 ± 0.39	2.16 ± 0.63
	average	2.98 ± 0.01	3.36 ± 0.31	3.17 ± 0.50	2.54 ± 0.36
250	x	2.99 ± 0.44	3.14 ± 0.42	3.23 ± 0.40	2.50 ± 0.77
	y	2.29 ± 0.46	3.76 ± 0.40	3.43 ± 0.61	2.70 ± 0.87
	z	2.81 ± 0.24	3.02 ± 0.26	2.96 ± 0.38	2.18 ± 0.54
	average	2.70 ± 0.37	3.31 ± 0.39	3.21 ± 0.24	2.46 ± 0.26
300	x	2.56 ± 0.22	3.12 ± 0.36	3.02 ± 0.50	1.58 ± 0.42
	y	2.60 ± 0.53	3.38 ± 0.27	3.69 ± 0.59	2.84 ± 0.68
	z	2.31 ± 0.25	2.87 ± 0.18	2.87 ± 0.40	1.74 ± 0.64
	average	2.49 ± 0.16	3.12 ± 0.26	3.19 ± 0.43	2.05 ± 0.68
350	x	2.37 ± 0.47	2.56 ± 0.36	2.71 ± 0.67	1.82 ± 0.59
	y	--	2.86 ± 0.50	2.91 ± 0.57	2.09 ± 1.17
	z	2.55 ± 0.30	2.57 ± 0.42	2.71 ± 0.58	1.56 ± 0.58
	average	2.46 ± 0.13	2.66 ± 0.17	2.78 ± 0.11	1.82 ± 0.27
400	x	1.76 ± 0.25	2.57 ± 0.52	2.72 ± 0.84	1.74 ± 0.80
	y	1.56 ± 0.41	2.43 ± 0.57	2.07 ± 0.64	1.76 ± 1.15
	z	2.05 ± 0.32	2.24 ± 0.40	2.77 ± 0.53	2.16 ± 0.67
	average	1.79 ± 0.25	2.41 ± 0.17	2.52 ± 0.39	1.88 ± 0.24
450	x	1.65 ± 0.31	2.02 ± 0.41	1.98 ± 0.60	1.51 ± 0.56
	y	1.30 ± 0.33	2.04 ± 0.27	2.12 ± 0.63	0.90 ± 0.76
	z	1.52 ± 0.08	2.09 ± 0.26	2.32 ± 0.80	0.85 ± 0.50
	average	1.49 ± 0.18	2.05 ± 0.04	2.14 ± 0.17	1.02 ± 0.44

3.5 Simulation process

3.5.1 Iso-thermal crystallization process

The equilibrated sample at 600 K is cooled to 50 K at a rate of 1 K/ps. At each 50 K interval during the quenching process, simulation samples are taken and subjected to long (up to 24 ns), constant temperature and pressure simulations (NPT) for the nucleation analysis. The cooling and iso-thermal crystallization processes are illustrated in **Figure 3.9**.

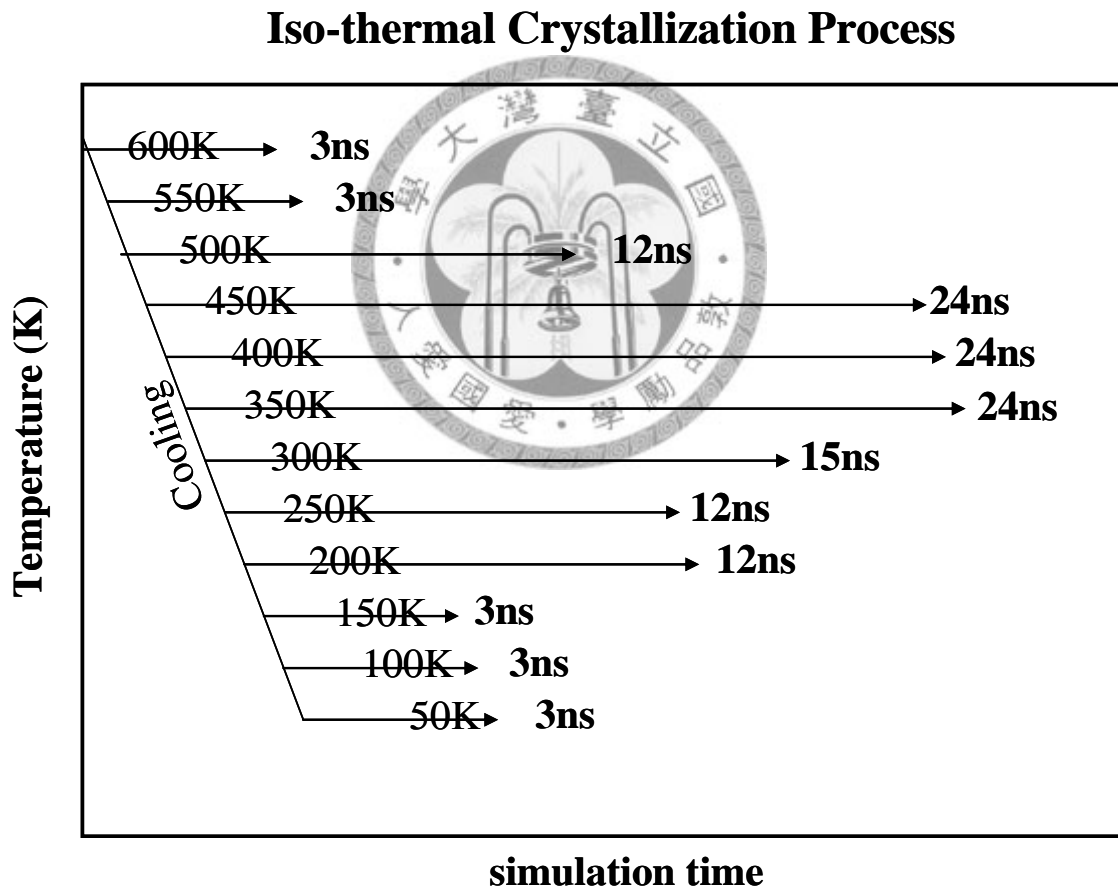


Figure 3.9 The cooling and iso-thermal crystallization processes.

3.5.2 Stress-induced crystallization process

After a 100 ps isothermal relaxation, the samples are then drawn with different drawing speeds ($1 \times 10^8 \text{ s}^{-1}$ (only at 400K), $1 \times 10^9 \text{ s}^{-1}$, $1 \times 10^{10} \text{ s}^{-1}$, and $1 \times 10^{11} \text{ s}^{-1}$), and isothermally relaxed at several draw ratios (DR=1, 2, 3, and 4) up to 12 ns. **Table 3.3** shows the number of sample is drawn to study stress-induced crystallization; the simulation time at different draw ratios is shown in **Table 3.4ab**.

Table 3.3 The number of independent samples used to study stress-induced crystallization.

Temperature (K)	Draw speeds		
	$1 \times 10^9 \text{ s}^{-1}$	$1 \times 10^{10} \text{ s}^{-1}$	$1 \times 10^{11} \text{ s}^{-1}$
200	3	3	3
250	3	3	3
300	3	3	3
350	3	3	3
400	3	3	3
450	3	3	3

Table 3.4a The simulation time for isothermal relaxation of PTT after different draw ratios at a constant draw speed of $1 \times 10^9 \text{ s}^{-1}$.

Temperature (K)	Draw speed = $1 \times 10^9 \text{ s}^{-1}$		
	DR=2	DR=3	DR=4
200	9 ns	3 ns	6 ns
250	12 ns	3 ns	--
300	15 ns	6 ns	6 ns
350	18 ns	9 ns	--
400	18 ns	12 ns	6 ns
450	15 ns	9 ns	--

Table 3.4b The simulation time for isothermal relaxation of PTT after different draw ratios at constant draw speeds of $1 \times 10^{10} \text{ s}^{-1}$ and $1 \times 10^{11} \text{ s}^{-1}$.

Temperature (K)	Draw speed = $1 \times 10^{10} \text{ s}^{-1}$ and $1 \times 10^{11} \text{ s}^{-1}$		
	DR=2	DR=3	DR=4
200	6 ns	6 ns	6 ns
250	--	--	--
300	6 ns	6 ns	6 ns
350	--	--	--
400	6 ns	6 ns	6 ns
450	--	--	--

4 Isothermal Crystallization

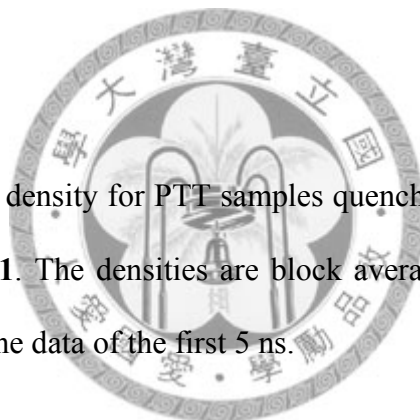
In the following, we will analyze the iso-thermal crystallization of PTT in various ways, including bulk properties, structural analysis of the precursors.

4.1 Bulk properties

The behaviors of bulk of amorphous phase are investigated during the early iso-thermal crystallization processes in this section. We focus on the density and all the energy components.

4.1.1 Density

The time evolution of density for PTT samples quenched to different temperatures are presented in **Figure 4.1**. The densities are block averaged (over 400 ps) from the trajectory, with exclusion the data of the first 5 ns.



4.1.2 Energy

The time evolution of energy for PTT samples quenched to different temperatures is presented, including kinetic (in **Figure 4.2**), potential (in **Figure 4.3**), band (in **Figure 4.4**), angle (in **Figure 4.5**), torsion (in **Figure 4.6**), inversion (in **Figure 4.7**) energies, and coulomb (in **Figure 4.8**) and van der Waals (in **Figure 4.9**) interactions.

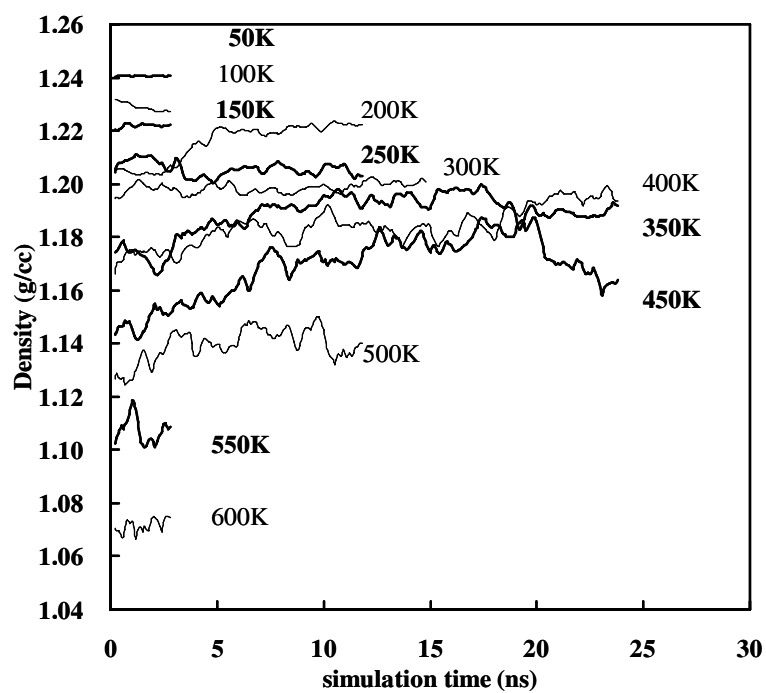


Figure 4.1 The time evolution of density during relaxation at different temperature.

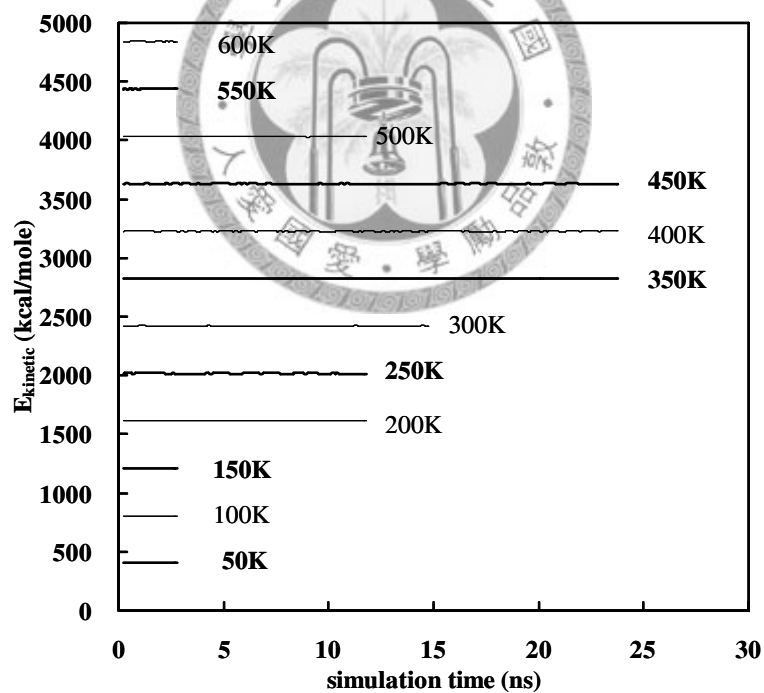


Figure 4.2 The time evolution of kinetic energy.

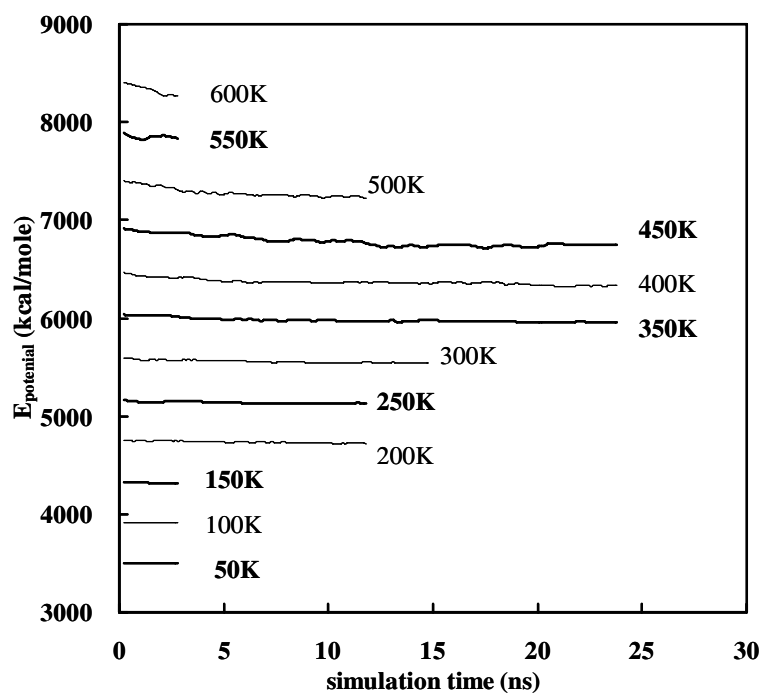


Figure 4.3 The time evolution of potential energy during relaxation at different temperature.

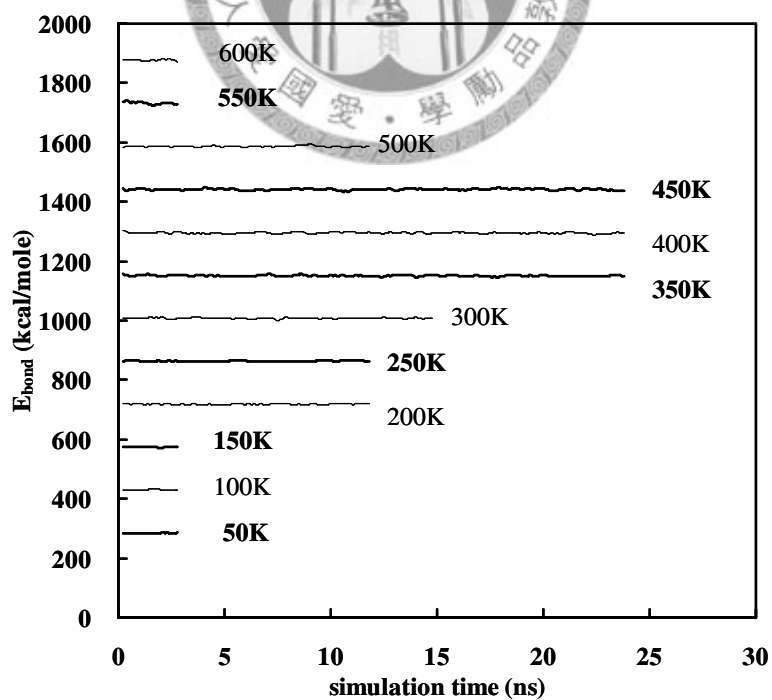


Figure 4.4 the time evolution of bond energy during relaxation at different temperature.

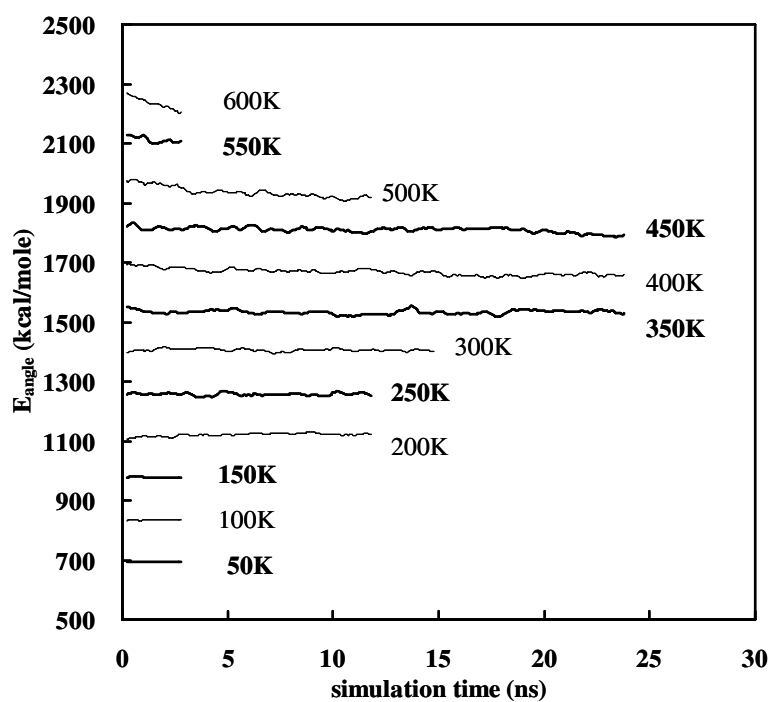


Figure 4.5 the time evolution of angle energy during relaxation at different temperature.

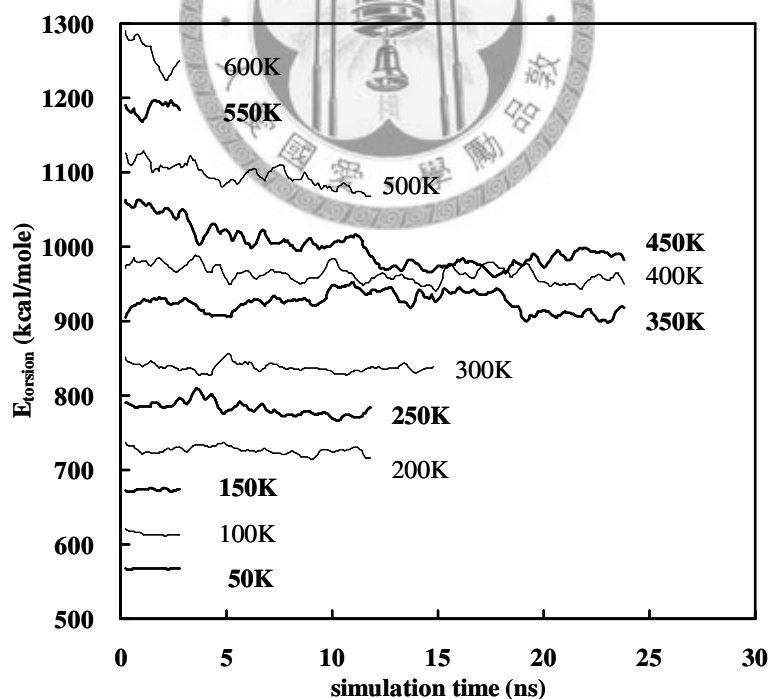


Figure 4.6 The time evolution of torsional energy during relaxation at different temperature.

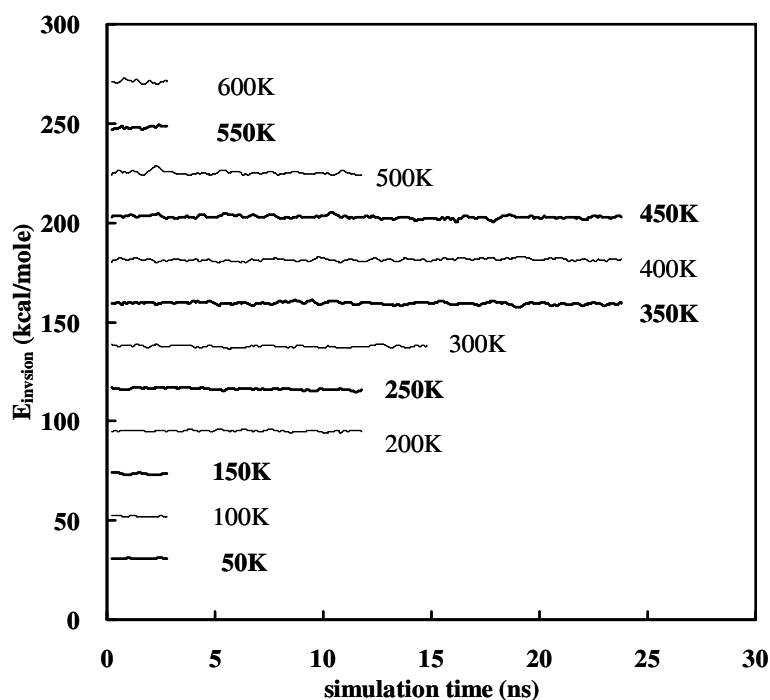


Figure 4.7 the time evolution of inversion energy during relaxation at different temperature.

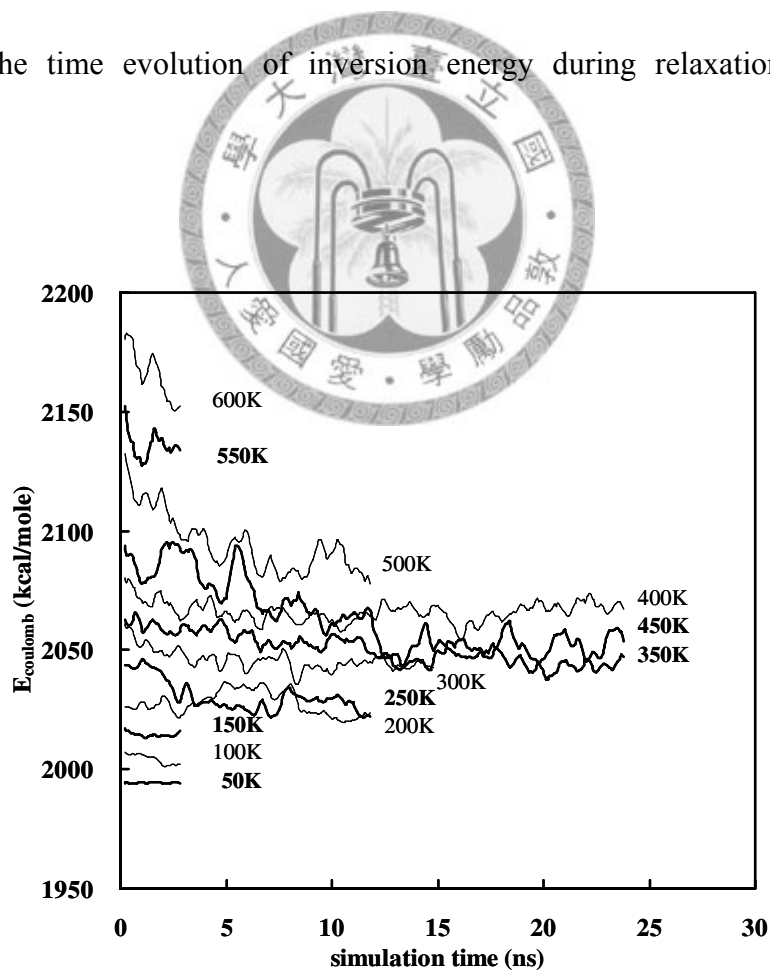


Figure 4.8 The time evolution of coulomb energy during relaxation at different temperature.

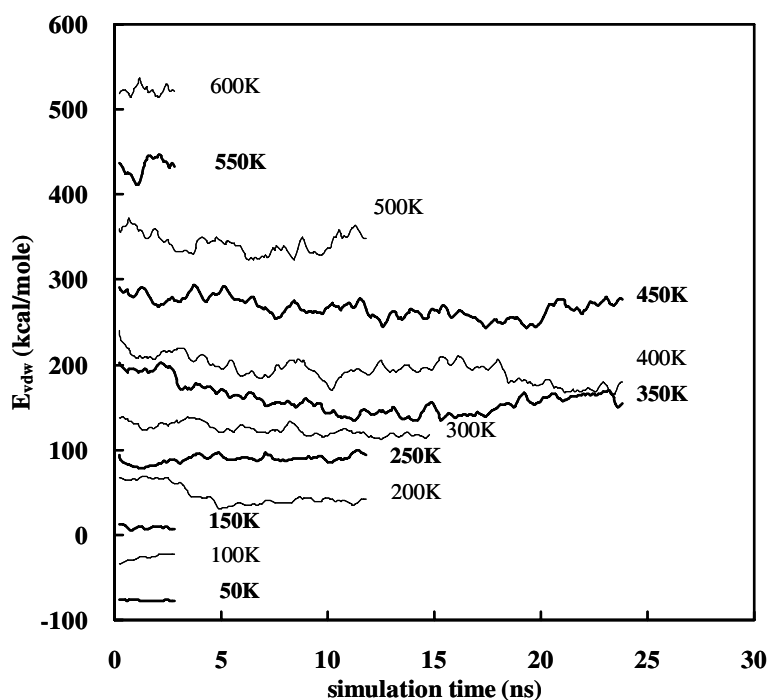
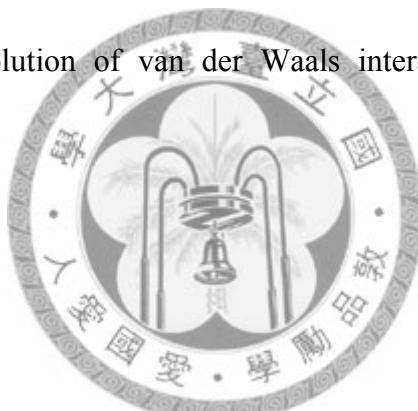


Figure 4.9 The time evolution of van der Waals interaction during relaxation at different temperature.



4.1.3 Discussion

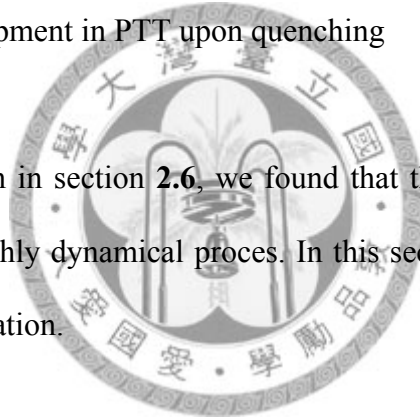
From above, it can be seen that for temperatures above 350 K (T_g) the densities (**Figure 4.1**) continue to rise and potential energy (**Figure 4.3**) to decrease with time; while below 350 K, both properties remain constant indicating the lost of mobility of the polymer chains. It is found that the variation in energy is dominated by the torsional angle rotation energy (**Figure 4.6**) and the van der Waals interaction (**Figure 4.9**), indicating that backbone rearrangement and chain packing are taking place. It is also interesting to note that the change in torsional angle rotation energy with time is different at 350K, 400K, and 450K. (Note that longer (24ns) simulations were performed for these three cases as they fall between T_g and T_m where nucleation process may take place.) These results indicate that the mechanism of the torsional angle

rotation in the crystallization could be different at various temperatures.

The increase of density for PTT at temperatures above 350 K is quite prominent. The variation in density shows a rapid increase at short time (< 5 ns) and then progresses at a slower rate. The rapid raising of density in short time may be a result of thermal relaxation after cooling, and the subsequent variation may indicate the progression of phase transition in long time. It should be noted that the simulated density of PTT melt at 600 K is 1.06 g/cc and the crystalline phase is 1.441 g/cc. The density values seen here indicate that the systems are still largely in an amorphous state.

4.2 Structure development in PTT upon quenching

Base on the definition in section 2.6, we found that the formation and growth of nucleus precursors is a highly dynamical proces. In this section, we would analyze the progress of precursor formation.



4.2.1 Precursor fraction

Base on **Equation 2.14**, the time evolution and the temperature dependence of the fraction of precursor in PTT samples quenched to different temperatures (350K to 450K) are presented in **Figure 4.10** and **Figure 4.11**. The results of double sized of system (8 chains of PTT molecular, each having 27 repeat units), which have the similar shop of the curves, are also shown is **Figure 4.12** and **Figure 4.13**.

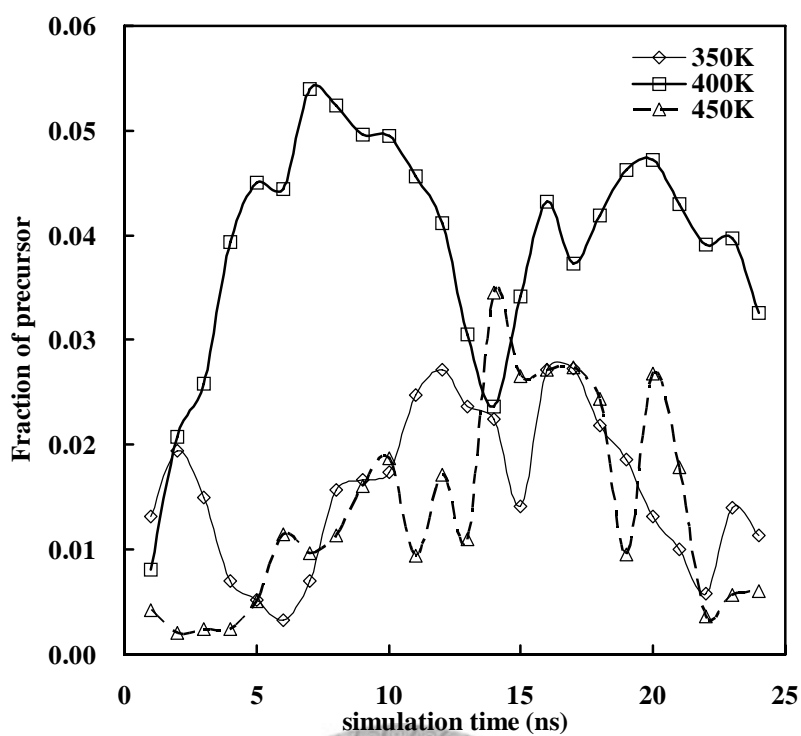


Figure 4.10 The variation of the amount of the precursor (defined in equation 2.14) with time at 350, 400, and 450K. (27x4)

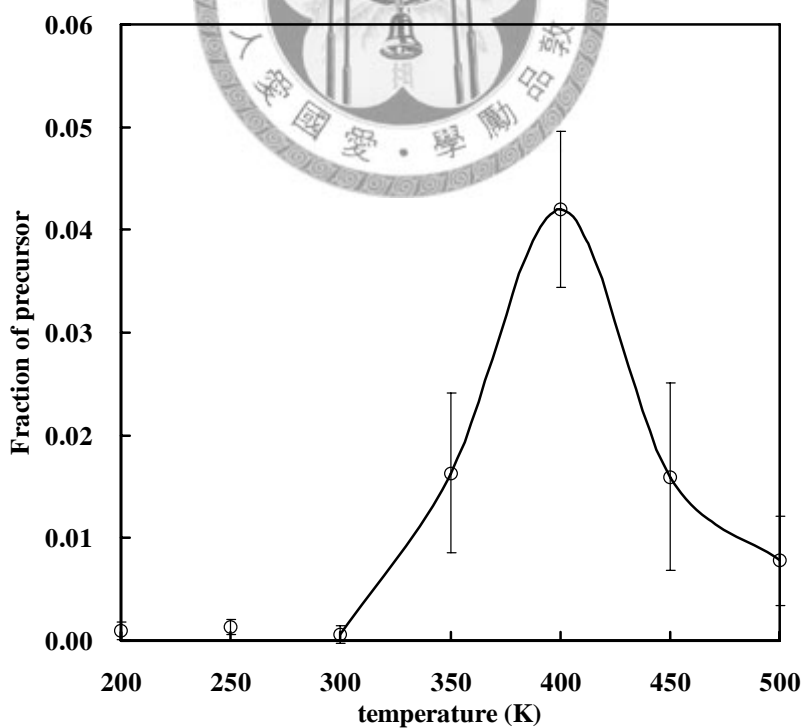


Figure 4.11 The variation of the average amount of the precursor (defined in equation 2.14) with temperature. (27x4)

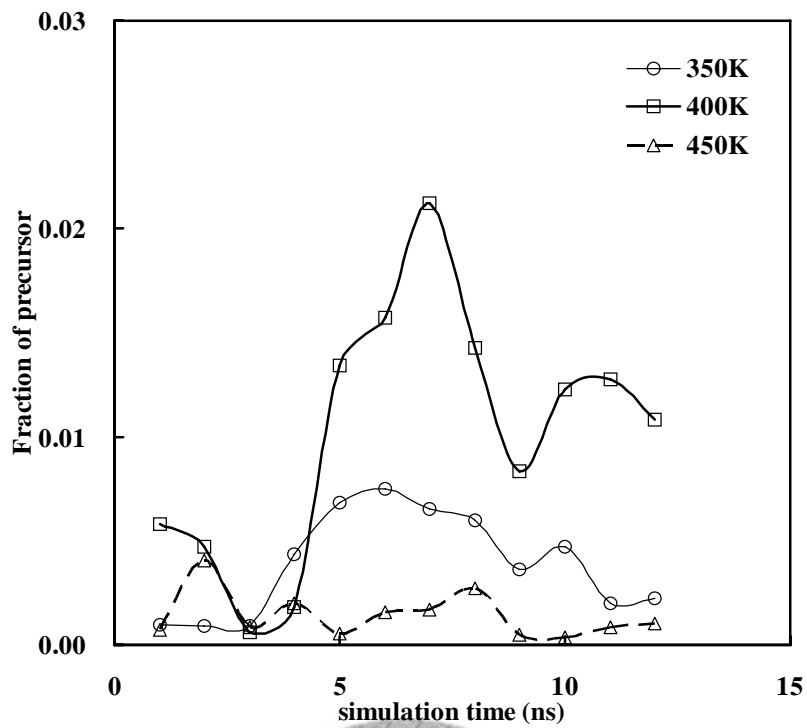


Figure 4.12 The variation of the amount of the precursor (defined in equation 2.14) with time at 350, 400, and 450K. (27x8)

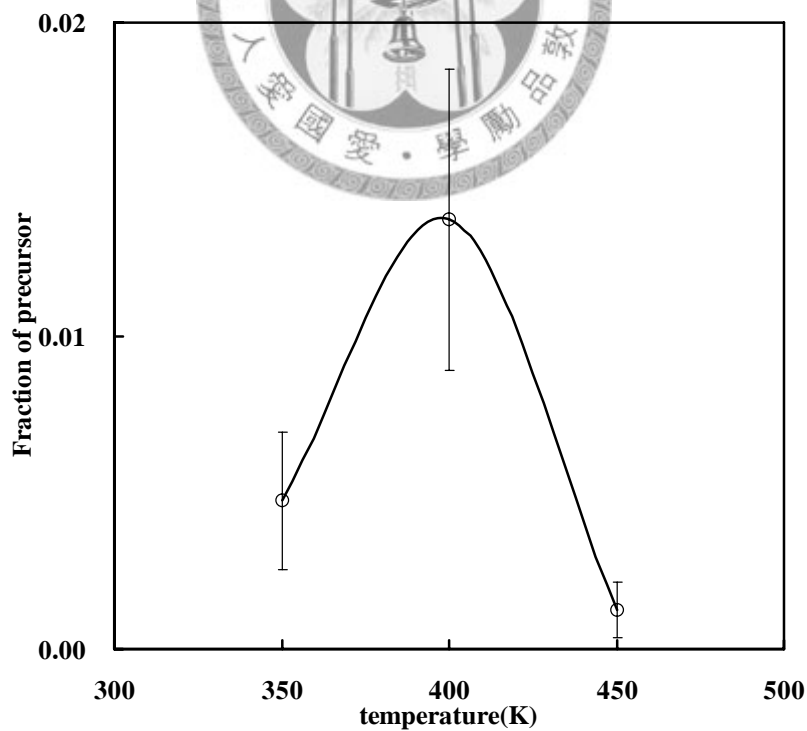


Figure 4.13 The variation of the average amount of the precursor (defined in equation 2.14) with temperature. (27x8)

4.2.2 Degree of order of the system

In this section, the spatial and orientational order of the quenched PTT samples is analyzed by RDF (Figure 4.14), atomic density in one dimension (Figure 4.15), and orientation factor (Figure 4.16); nevertheless, there is no obvious change in these results.

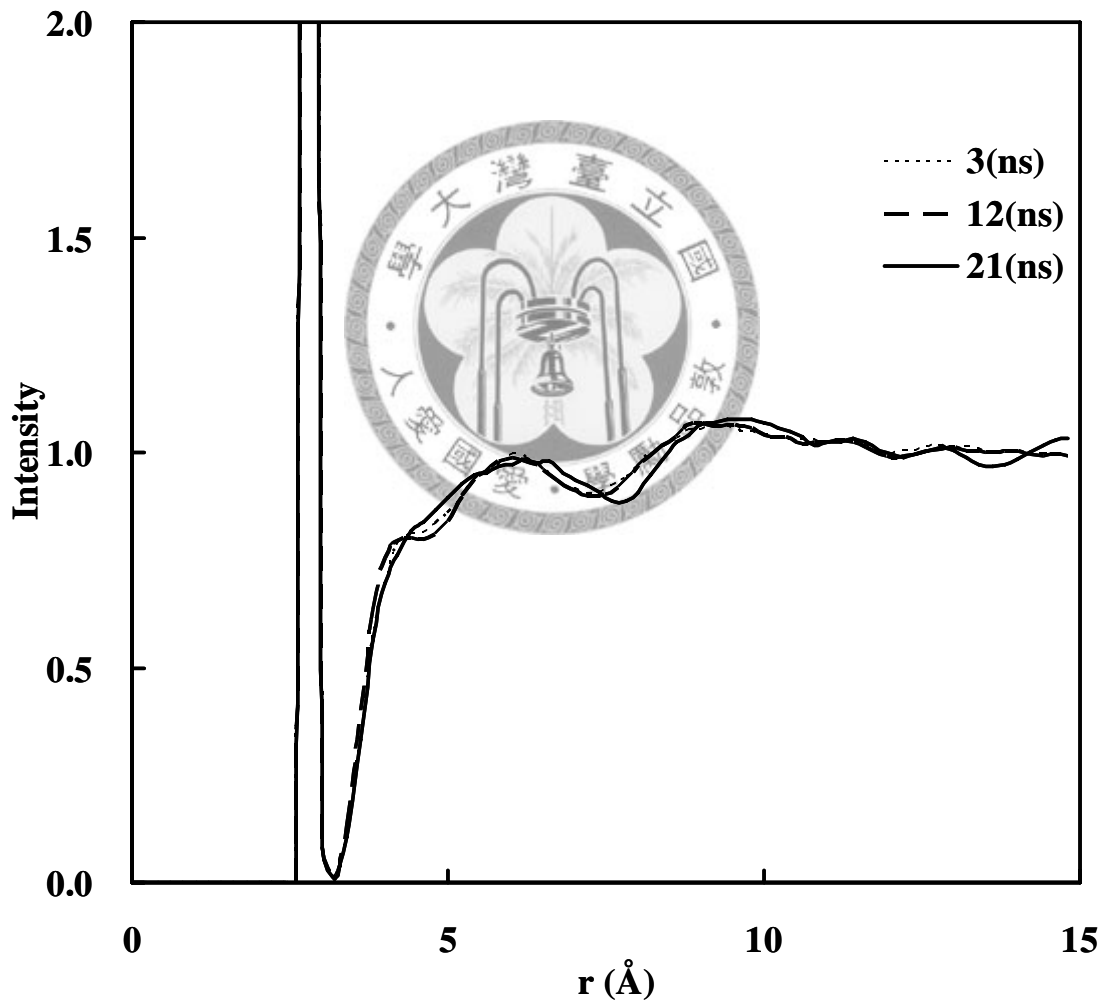


Figure 4.14 The RDF of the quenched PTT state at 400K.

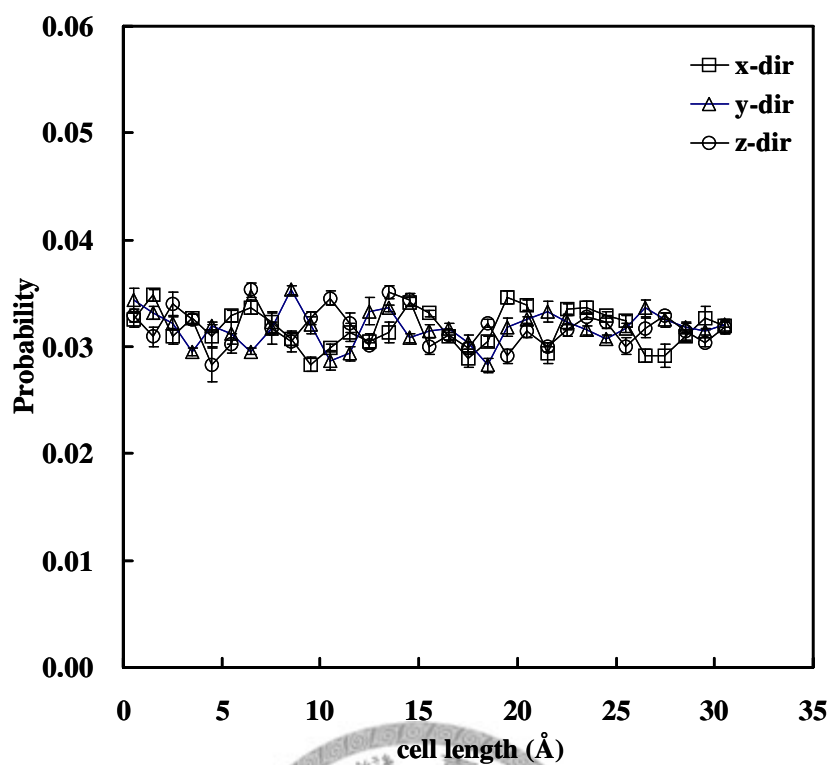


Figure 4.15 The probability of the atoms in the PTT quenched state at 400K.

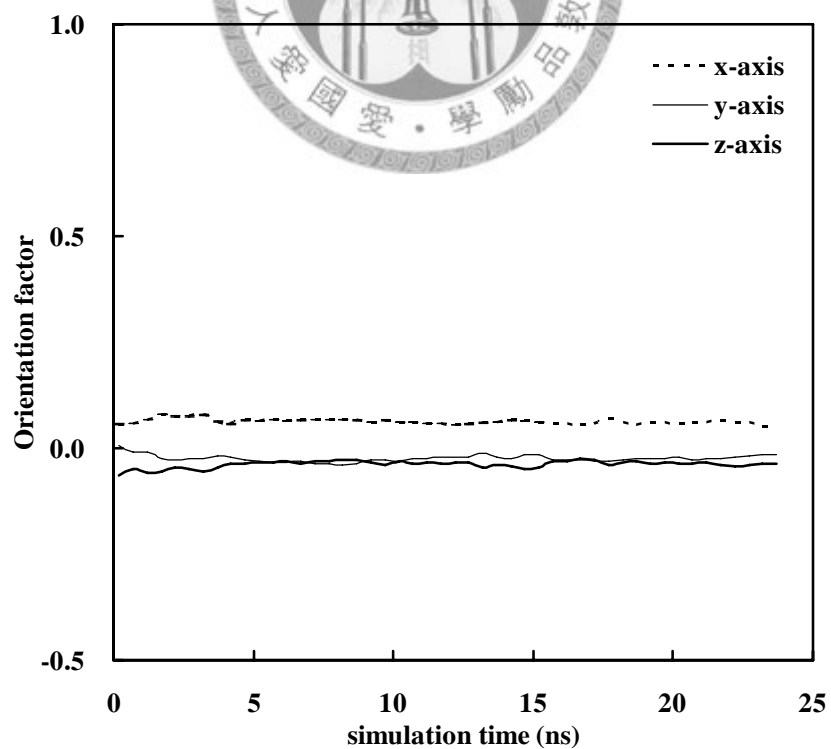


Figure 4.16 The orientation factor in the PTT quenched state at 400K.

4.2.3 Discussion

From the results of the degree of order in 400K, no obvious change is found in RDF during the simulation time. The probability of atoms appear in each position remains the same, and the orientation factor are almost zero in three directions. This indicate that there is no large scale structure appear during simulation process. In order to study the locally structure in the bulk of quenched PTT.

In contrast, the segment analysis does show the formation of parallel clusters within the system. In the liquid state (600 K) there are constant formation and disintegration of small clusters ($s=2, 3, 4,$ and 5) via segment vibration and collisions, i.e., these clusters are short-lived. As the system is quenched below T_m , these some segments may agglomerate or deposit on a nearby cluster to form larger sized precursors. In the subsequent NPT runs, these precursors may grow, break down to small clusters, or dissolve back to the amorphous phase. Both the growth and disintegration of precursors are observed in this stage, however, the net effect (for a certain sized cluster to grow or dissolve) depends on the temperature and the size of the precursor (as it should be driven by thermodynamic equilibrium). As the temperature falls below T_g , small precursors become long-lived, however, most of them lose sufficient mobility to overcome barriers which prevents the formation and growth of larger precursors. As a consequence, we observe the presence of precursors peaks at a temperature between T_g and T_m .

From **Figure 4.10**, one can observe a clear trend of rapid enhancement of fraction of precursor, especially near 400 K, at the beginning of thermal equilibration. Afterwards, the amount of precursors present starts to fluctuate. **Figure 4.11** shows the

average amount of precursors as a function of temperature. Strikingly the temperature dependence of the fraction of precursor curve resembles that of crystallization rate for common polymers, i.e., having a maximum between T_g and T_m . This indicates that the existence of nucleus precursors plays an important role in the crystallization process.

4.3 Structure development within Nucleus precursor

The structure development of the precursors as a result of the interplay between the van der Waals and torsional forces can be better understood by analyzing the precursor size, radial distribution function (RDF), and torsional angle distributions of each individual precursor identified from section 4.3.1. In this section, we would identify the precursors in each sample and try to understand the relation among them.

4.3.1 Structure identification

According to the definition of nucleus precursor, a numbers of precursors can be identified. We show the number of precursors, and some of their basic properties at temperatures from 300K to 450 K are summarized in **Table 4.1**. In general 2 to 3 precursors can be found in each sample (containing 108 segments) and most of them continue to grow throughout the duration of our simulation (the time evolution of the precursor size at different temperatures is shown in **Figure 5.23 ~ 5.26**). The precursors identified from the NPT simulation at 400K and 6 time instants are illustrated in **Figure 4.17**. One can easily visualize the formation of the precursors.

Table 4.1 The number and size of individual precursors identified in isothermal crystallization.

Temperature (K)	Number of precursors [†]	Simulation length (ns)
300	3 (5,5,5)	15
350	3 (9,6,5)	24
400	2 (9,6)	24
450	3 (7,7,6)	24

[†]Shown in the parenthesis are the maximum size s observed for each precursor.

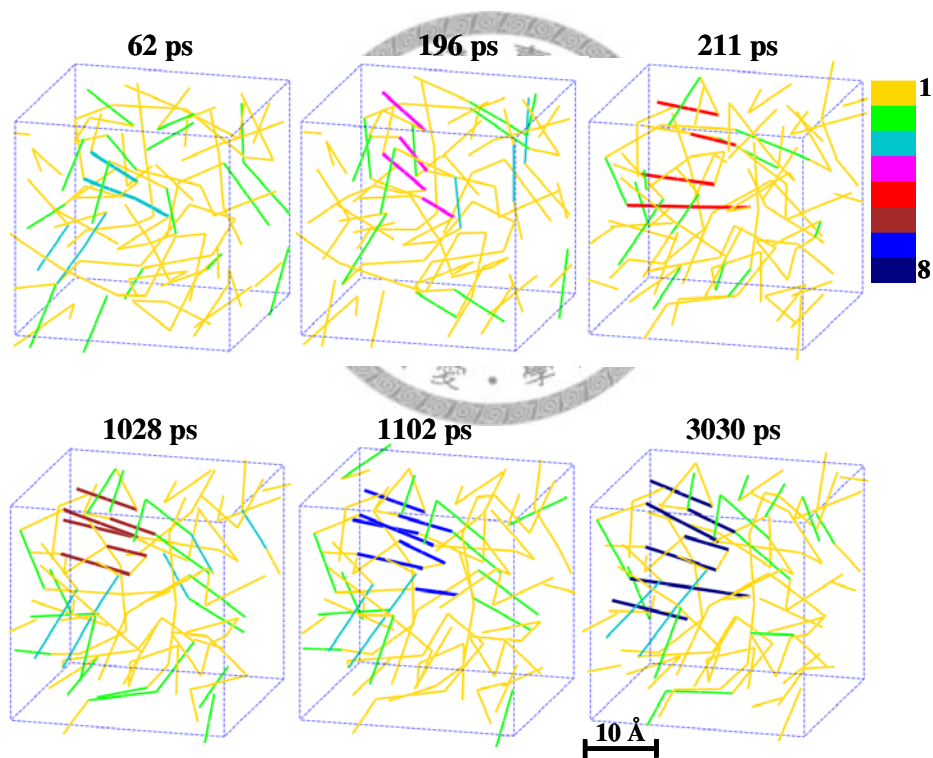


Figure 4.17 Illustration of the growth of nucleus precursor from melted state at 400 K. A color scale is used for better discrimination of the size of precursors.

4.3.2 Radial distribution function

The RDF calculated from the 1, 4 carbon atoms on the aromatic ring (See **Figure 1.3b**) is used to quantify the segment packing within the precursors (thus, the three type, 1,1 pairs, 4,4 pairs, and 1,4 pairs are considered). In order to identify the characteristic band of the RDF in the amorphous phase, we analyze the crystalline phase first. From **Figure 4.18**, the first peak (2.85 Å) indicates the distance of the 1, 4 carbons on the same ring; the second and third peaks would merge at ~4.11 Å, when the system melts to the amorphous state. The RDF of each precursor from the NPT simulation at 300K, 350K, 400K, and 450K (shown in **Table 4.1**) are presented in **Figure 4.19**, **Figure 4.20**, **Figure 4.21**, and **Figure 4.22**, respectively. The time evolution of the intensities of RDF at 4.11 Å for PTT precursors quenched to 300K, 350K, 400K, and 450K are shown in **Figure 4.23**, **Figure 4.24**, **Figure 4.25**, and **Figure 4.26**, respectively. The value of intensity is the time average over a period of 1 ns. (Note we only show the results of the maximum precursor of each temperature Besides, the results of double-sized systems are shown in **Appendix B**)

For example, the calculation of RDF only use the segments in the largest cluster (s=9) at 400K. Because the volume fraction of the 9 segments is about 8.7% (9/104, 26 segments in one chain), above 90% of the cell space considers as vacuum in RDF calculation. Thus, the value of the intensity is below 1 in the range of 20-30 Å, but the value of the base intensity goes to 1 at long range. We can estimate the length scale of the cluster is about 14 Å (44% (cube root of 8.7%) of the cell length), and the meaningful RDF in our analysis is small than the half of the cluster length (~7 Å).

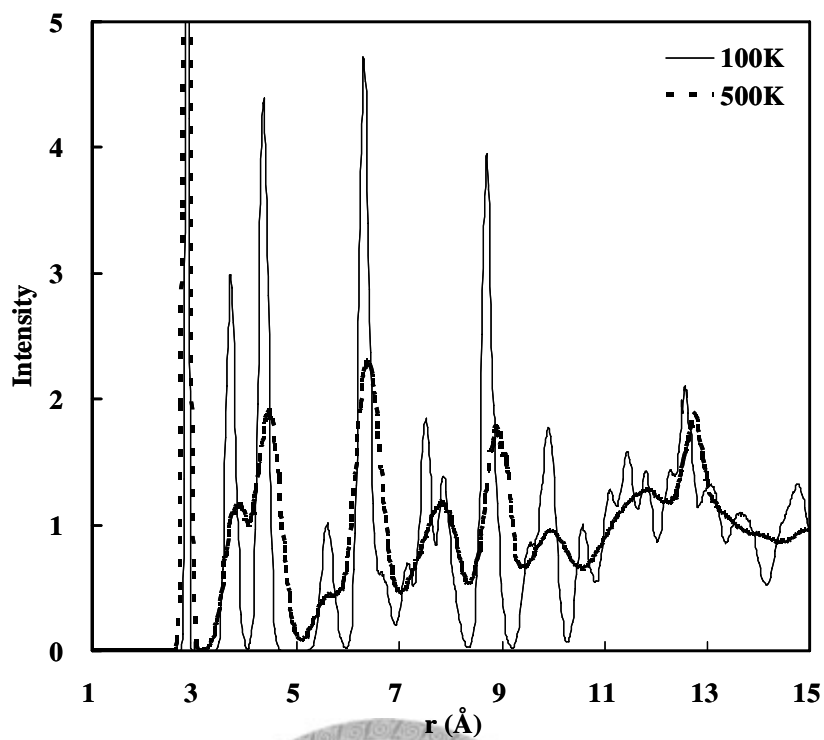


Figure 4.18 The RDF of 1,4 carbon atoms in crystalline PTT structure during a heating process.

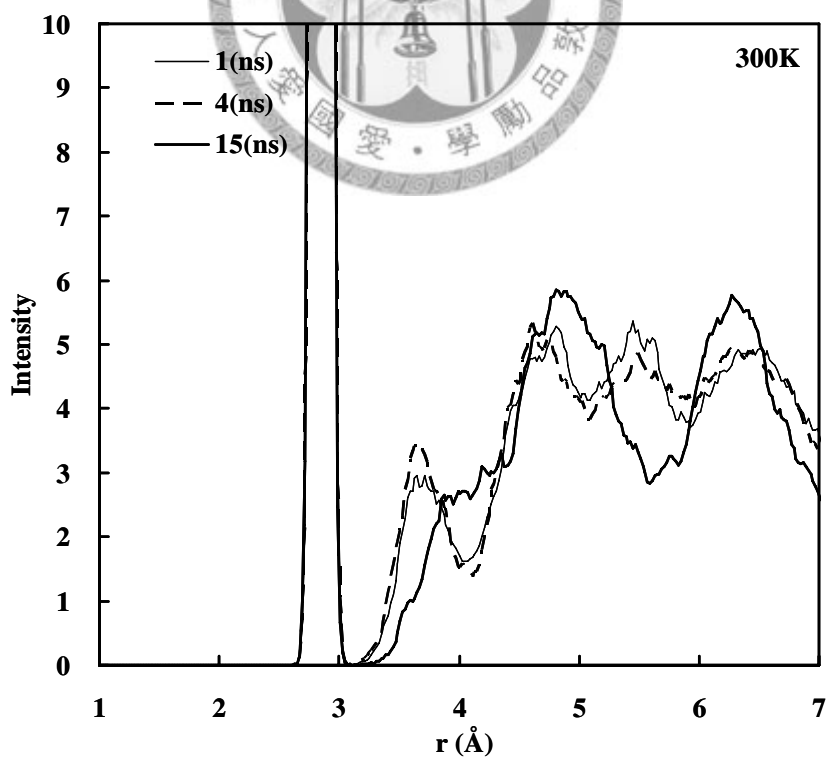


Figure 4.19 The RDF of precursor at 300K.

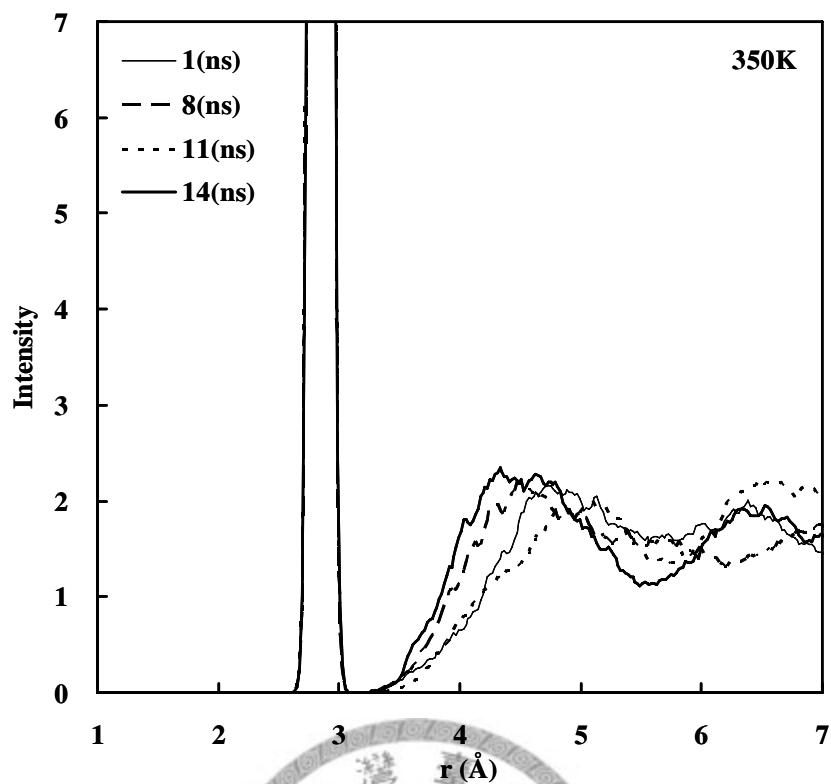


Figure 4.20 The RDF of precursor at 350K.

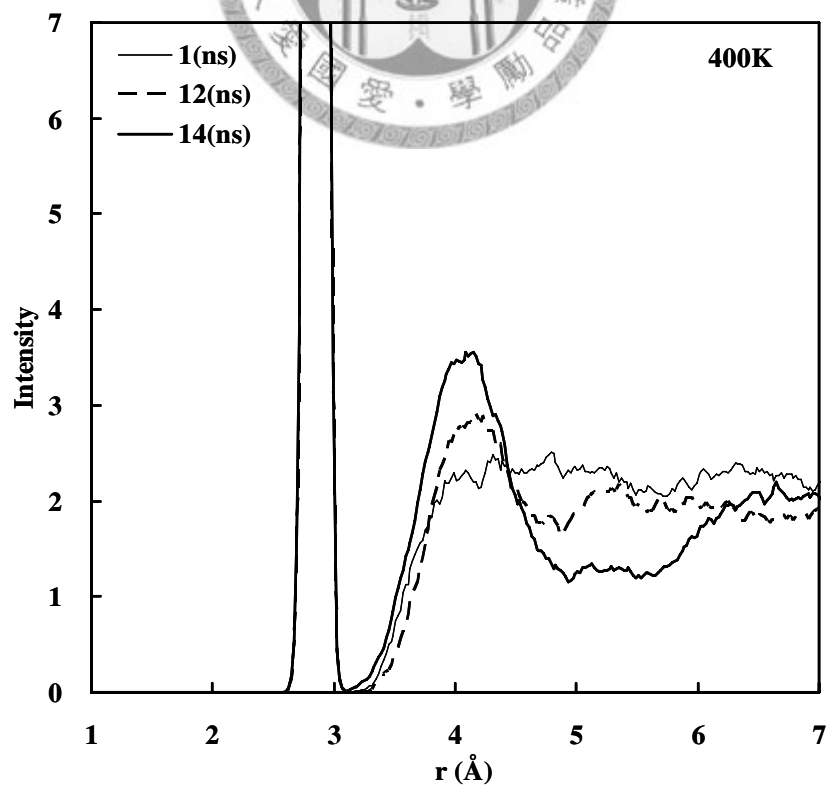


Figure 4.21 The RDF of precursor at 400K.

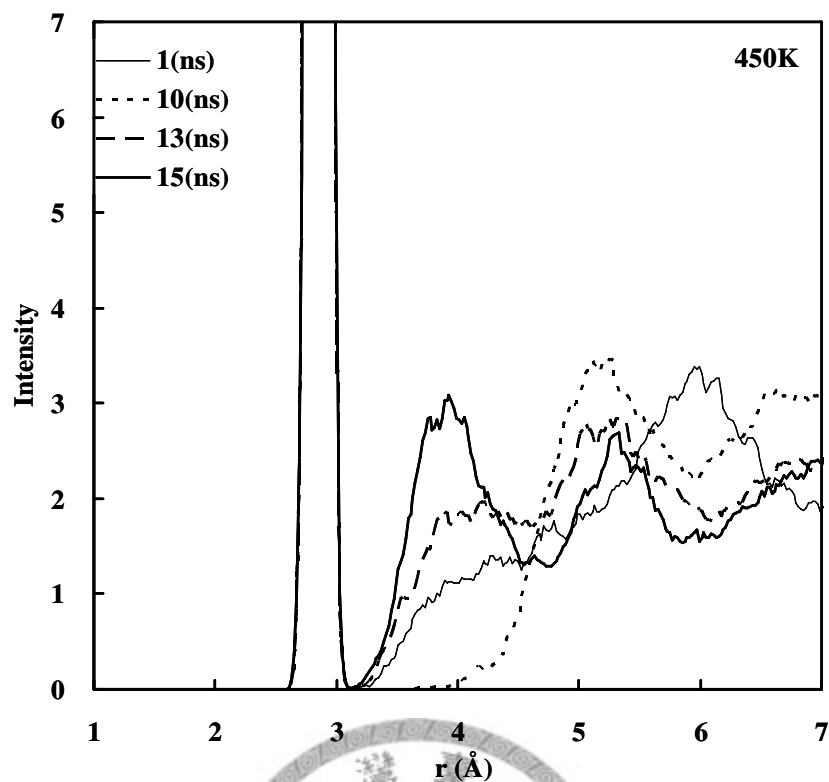


Figure 4.22 The RDF of precursor at 450K.

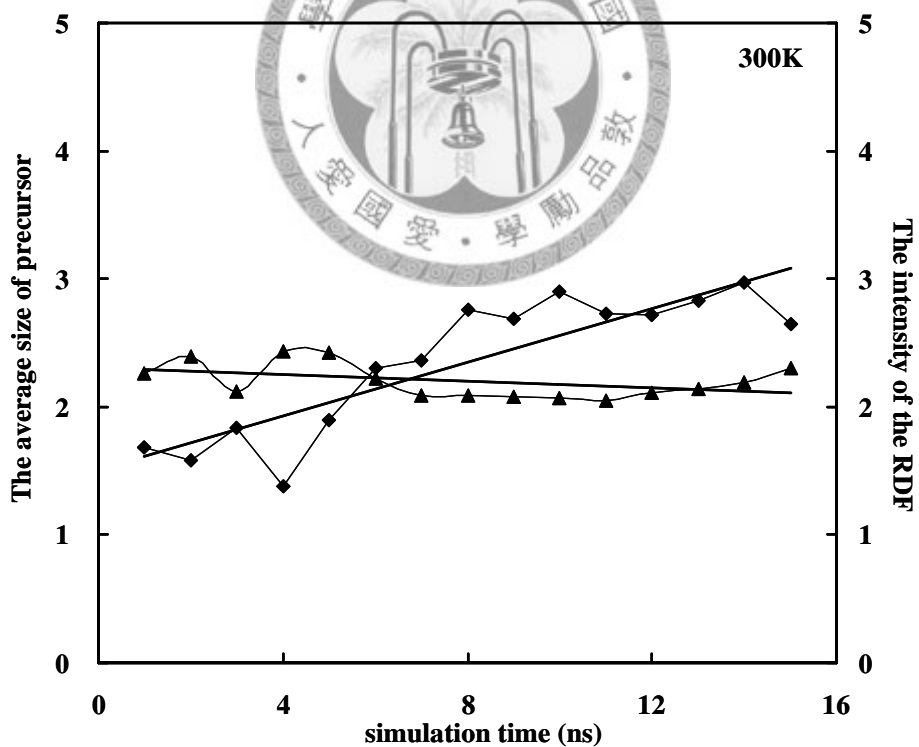


Figure 4.23 The time evolution of RDF intensity (4.11Å) (diamond) and the time averaged number of parallel segments contained in a representative precursor (triangle) at 300 K.

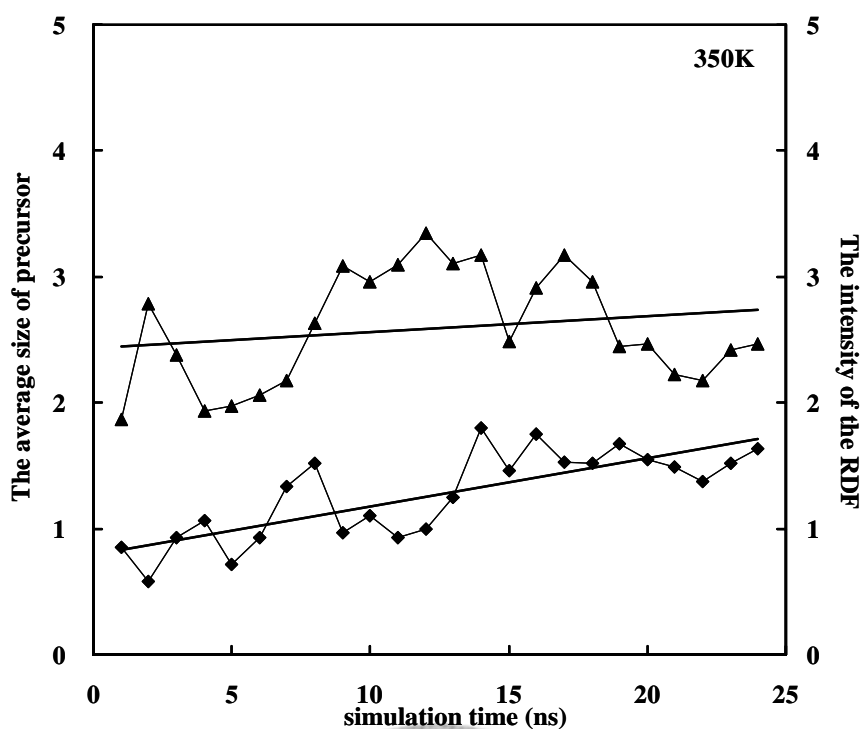


Figure 4.24 The time evolution of RDF intensity (4.11\AA) (diamond) and the time averaged number of parallel segments contained in a representative precursor (triangle) at 350 K.

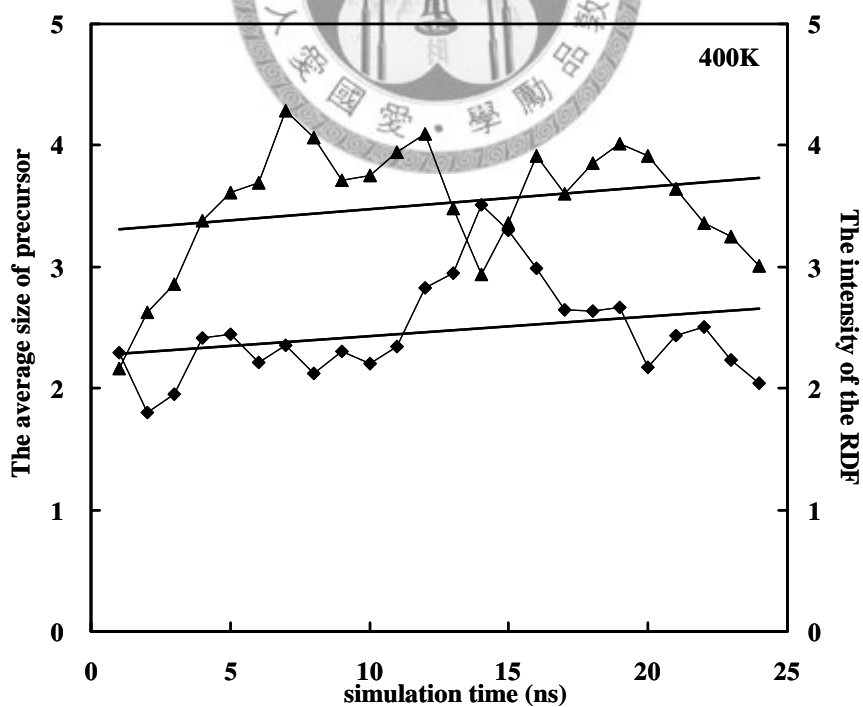


Figure 4.25 The time evolution of RDF intensity (4.11\AA) (diamond) and the time averaged number of parallel segments contained in a representative precursor (triangle) at 400 K.

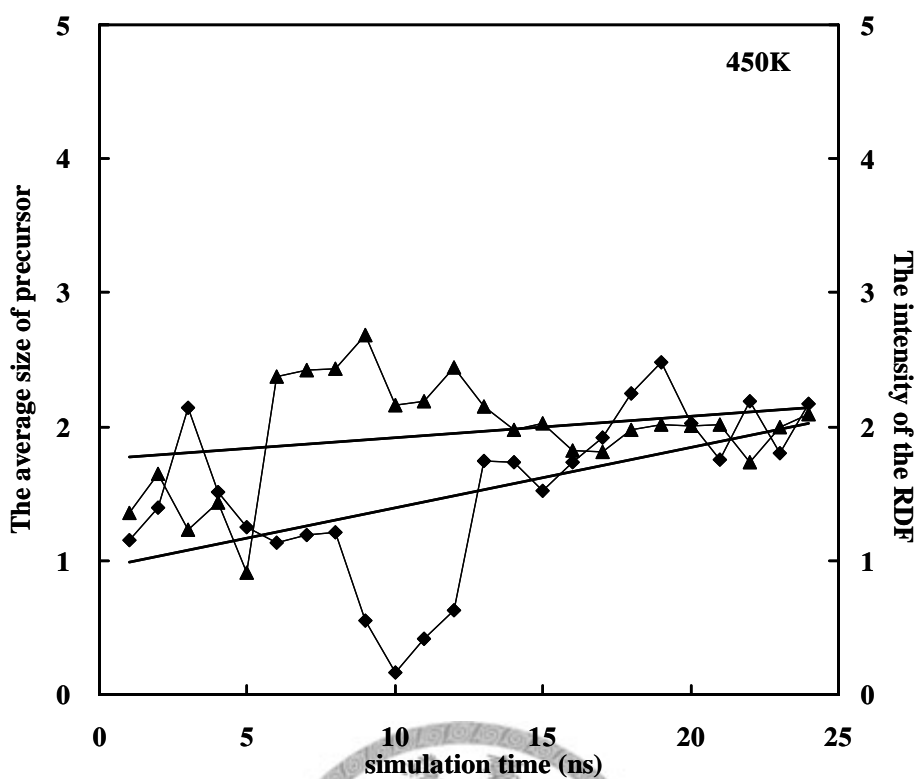


Figure 4.26 The time evolution of RDF intensity (4.11Å) (diamond) and the time averaged number of parallel segments contained in a representative precursor (triangle) at 450 K.

4.3.3 The average size of precursor

The time averaged number of parallel segments contained in a representative precursor, as identified in **Table 4.1**, is shown in **Figure 4.19 ~ 22**. The value of average size is the time average over a period of 1 ns.

4.3.4 Torsion angle distribution

The time variation of fractions of backbone torsions within each the precursor domain and outside of precursor are also presented in **Figure 4.27 ~ 30**. The percentage of ϕ_1 in trans and ϕ_2 in gauche states within all precursors are shown in **Figure 4.31**. The value of $\langle\phi\rangle$ is the time average of ϕ and ϕ' over a period of 1 ns.

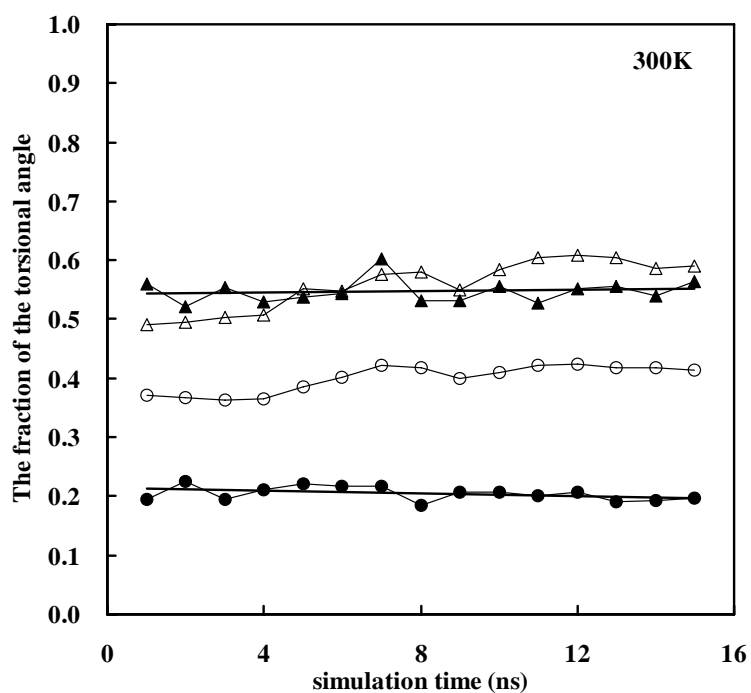


Figure 4.27 the backbone torsions $\langle\phi_1\rangle$ in trans (triangles) and $\langle\phi_2\rangle$ in gauche (circles) for segments in a precursor (closed symbols) and outside any precursor (open symbols) at 300 K.

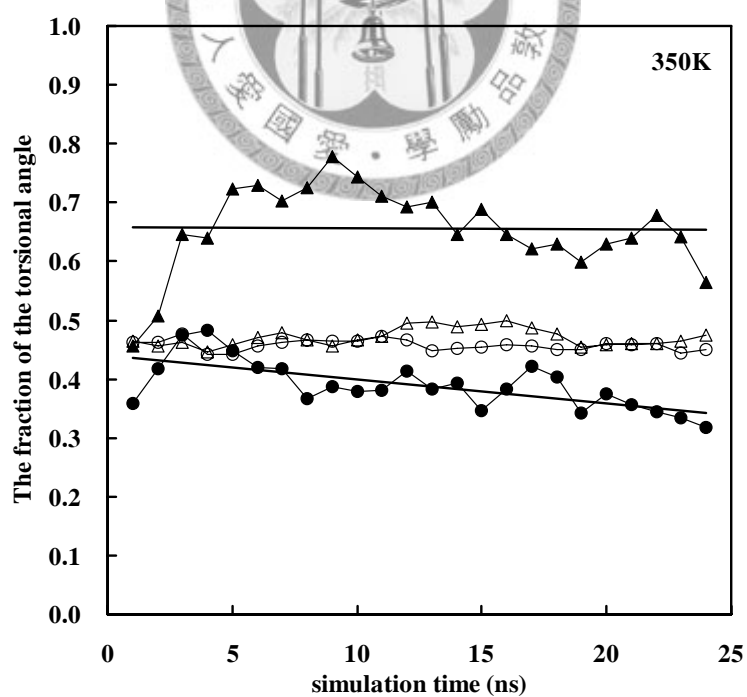


Figure 4.28 the backbone torsions $\langle\phi_1\rangle$ in trans (triangles) and $\langle\phi_2\rangle$ in gauche (circles) for segments in a precursor (closed symbols) and outside any precursor (open symbols) at 300 K.

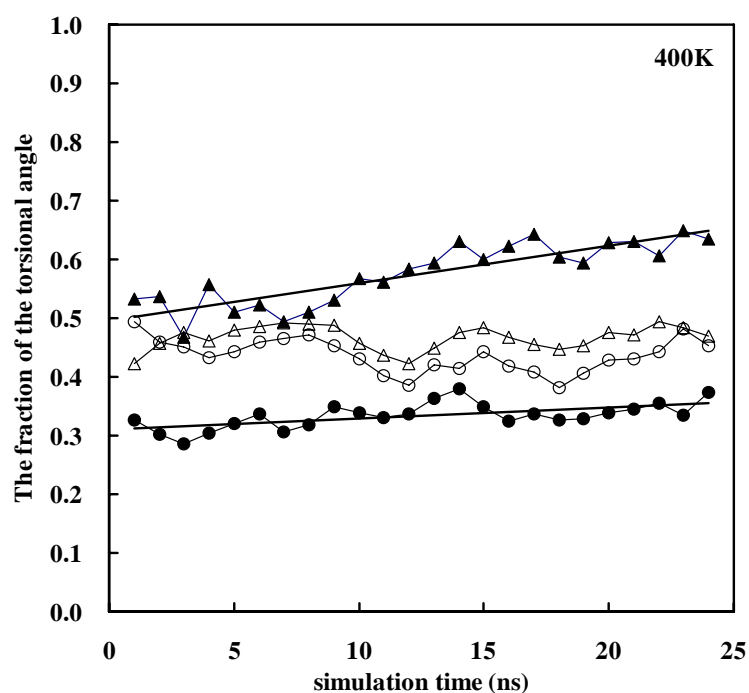


Figure 4.29 the backbone torsions $\langle\phi_1\rangle$ in trans (triangles) and $\langle\phi_2\rangle$ in gauche (circles) for segments in a precursor (closed symbols) and outside any precursor (open symbols) at 300 K.

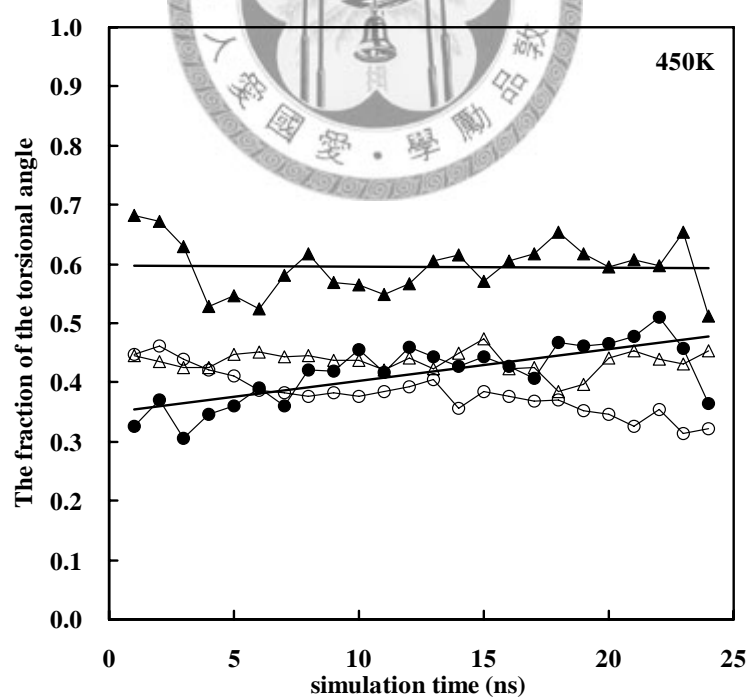


Figure 4.30 the backbone torsions $\langle\phi_1\rangle$ in trans (triangles) and $\langle\phi_2\rangle$ in gauche (circles) for segments in a precursor (closed symbols) and outside any precursor (open symbols) at 300 K.

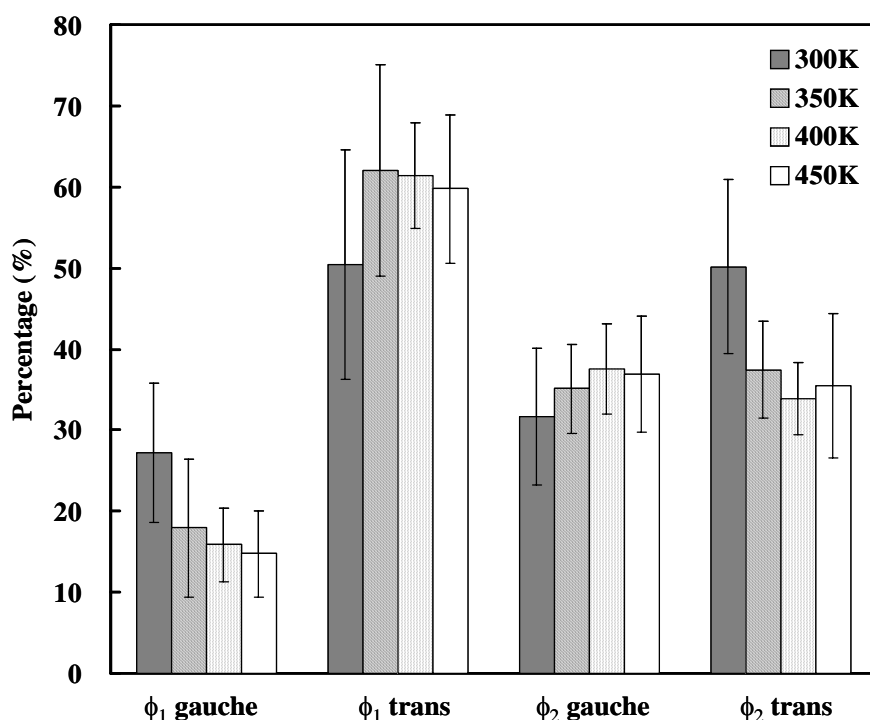


Figure 4.31 The percentage of these torsions in the trans and gauche states within all precursors.

4.3.5 Discussion

Although fluctuating, there is a general trend of enhancement of the peak intensity of RDF with time. The size evolutions of the same precursors are shown on the same plots for comparison. It can be seen that, while both properties increase with time, there is no direct correlation between them. The result indicates that better packing of the segments could sometimes be compromised as the precursor grows in size, and vice versa.

For segments within the precursors, the majority of $\langle\phi_1\rangle$ is in the trans state; however there is no clear preferred state for the more flexible $\langle\phi_2\rangle$, although at high temperatures the gauche state appears to slightly dominate. Moreover, it can be seen that for segments outside the precursors (open symbols), the backbone torsions seems to

be time invariant. In contrast, within the precursors (closed symbols), the backbone torsions may vary but not necessarily towards the t-g-g-t conformation. This implies that the torsion forces may be compromised by the vdW forces as the precursor develops. It is also interesting to note that at low temperatures (e.g. 350K), the backbone torsions may be trapped in poor conformations as the segments have less kinetic energy to overcome the torsion barrier. However, at higher temperatures (400K, 450K) we often observe the increase of the t-g-g-t fraction as the segments have sufficient energy to overcome torsion barriers should it ever enters none t-g-g-t conformation due to vdW forces. In other words, with sufficient energy to overcome the torsional barriers, the conformation of the O-CH₂-CH₂-CH₂-O preferentially evolves towards the trans-gauche-gauche-trans (t-g-g-t) conformation which is favored for the formation of a more compact nucleus.



5 Stress-Induced Crystallization

In this chapter, we focus on the stress-induced crystallization. The effects from stress, strain rate, and temperature are discussed in this chapter. The analysis results of draw process are block averaged (for example: DR=2 is calculated the data from DR=1.5 to DR=2.5), and the results of thermal relaxation are calculated from average of 6 ns. All the results are given in tables while representative ones are shown in figures.

5.1 Bulk properties

We analyze the density and each kind of energy during the drawing processes, comparing the results of relaxation after drawing at different draw ratios (DR).

5.1.1 Density

The DR variation of density at different temperatures with draw speeds $1 \times 10^9 \text{ s}^{-1}$, $1 \times 10^{10} \text{ s}^{-1}$, $1 \times 10^{11} \text{ s}^{-1}$ are shown in **Figure 5.1**, **Figure 5.3**, and **Figure 5.5**, respectively; the temperature function of density at different DR with each draw speeds are shown in **Figure 5.2**, **Figure 5.4**, and **Figure 5.6**. Moreover, density depends on the draw speed at each constant DR and temperature, which are shown in **Figure 5.13**.

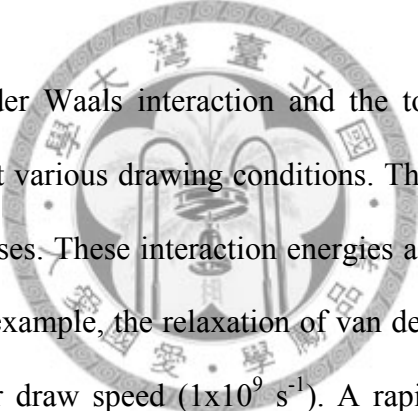
5.1.2 Energy

In all simulations, torsional energy, and non-bond interactions depend on the DR at each constant draw speed and temperature, but other components of potential energies are not. We show the temperature function of torsional energy (**Figure 5.7**, **Figure 5.9**, and **Figure 5.11**), and van der Waals interaction (**Figure 5.8**, **Figure 5.10**, and **Figure**

5.12) with each drawing speeds. Moreover, torsional energy, and non-band interactions also depend on the draw speed at each constant DR and temperature. We show the variation of the torsional and van der Waals at each drawing speeds in **Figure 5.13**.

5.1.3 Discussion

The density decreases fast in each simulation indicate that the defects (voids) in the bulk phase are created during the drawing processes. At high draw speeds ($1 \times 10^{10} \text{ s}^{-1}$, and $1 \times 10^{11} \text{ s}^{-1}$) and the temperatures below T_g the formation of defects is prominent; on the other hand, at the slower draw speeds ($1 \times 10^8 \text{ s}^{-1}$, and $1 \times 10^9 \text{ s}^{-1}$) and temperatures above T_g the system could relax to reduce the amount of defects.



The changes in van der Waals interaction and the torsional energy reflects the transition of the structure at various drawing conditions. The van der Waals interaction increases with DR in all cases. These interaction energies also have a significant effect in the system density. For example, the relaxation of van der Waals interaction leads to a constant density at lower draw speed ($1 \times 10^9 \text{ s}^{-1}$). A rapid augmentation of van der Waals interaction leads to a fast dropping in density at higher draw speed ($1 \times 10^{11} \text{ s}^{-1}$). Besides, the van der Waals interaction increases with temperature at constant DR. The enhancement of van der Waals interactions slows down at temperatures higher than T_g at lower draw speed. These results indicate that the mechanism of the chain packing is different in the various draw speeds and temperatures. This could be understood as a competition between thermal effect, which is prominent at slower draw speed and higher temperatures, and stress effect, which is prominent at faster draw speed and lower temperatures. On the other hand, the torsional energy decreases with DR at lower

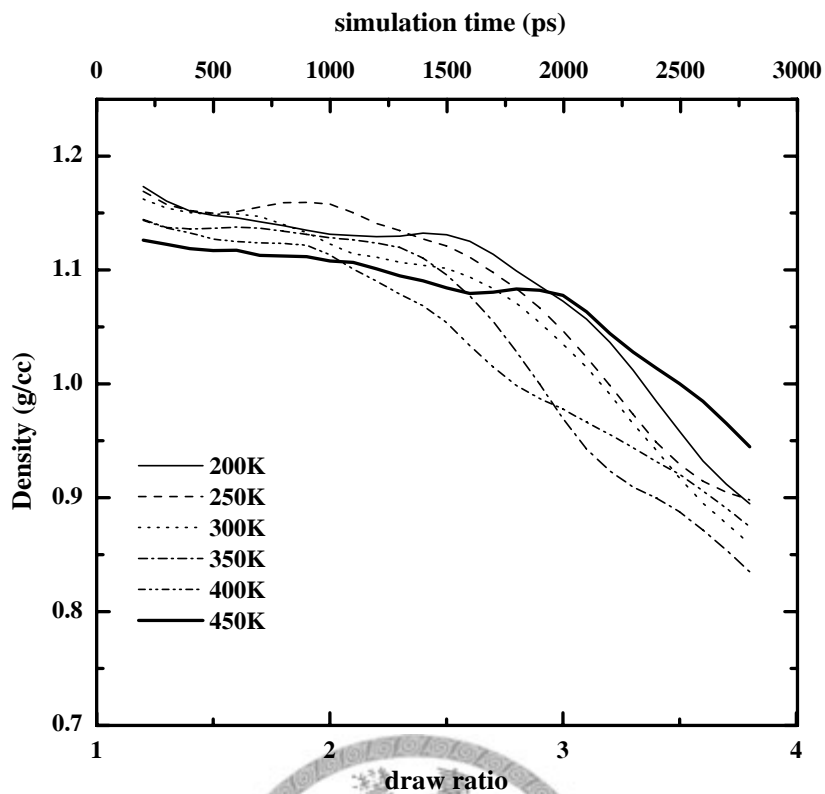


Figure 5.1 The DR variation of density at different temperatures with draw speed $1 \times 10^9 \text{ s}^{-1}$.

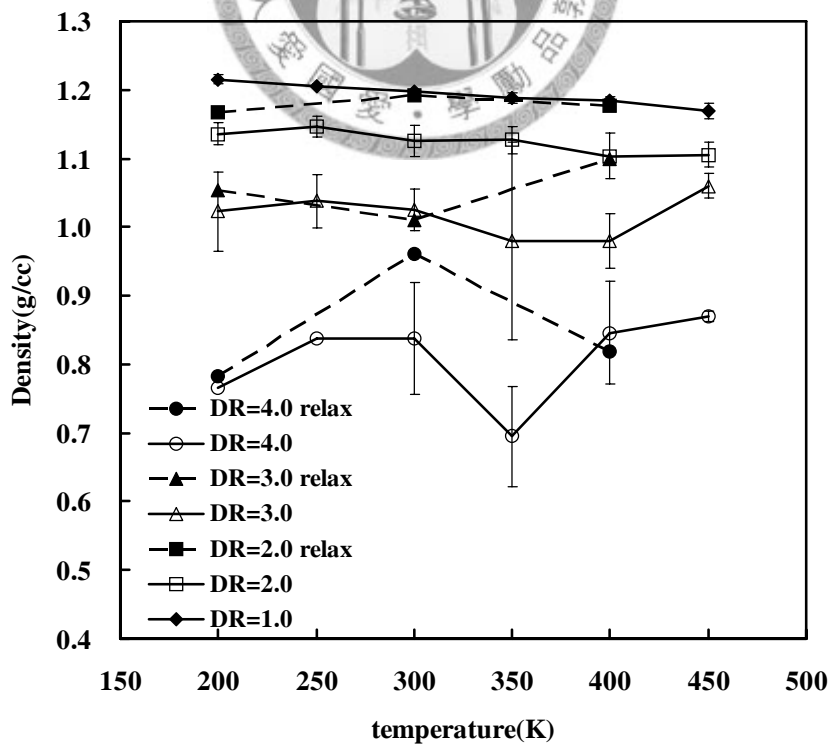


Figure 5.2 The temperature dependence of density at different DR with draw speed $1 \times 10^9 \text{ s}^{-1}$.

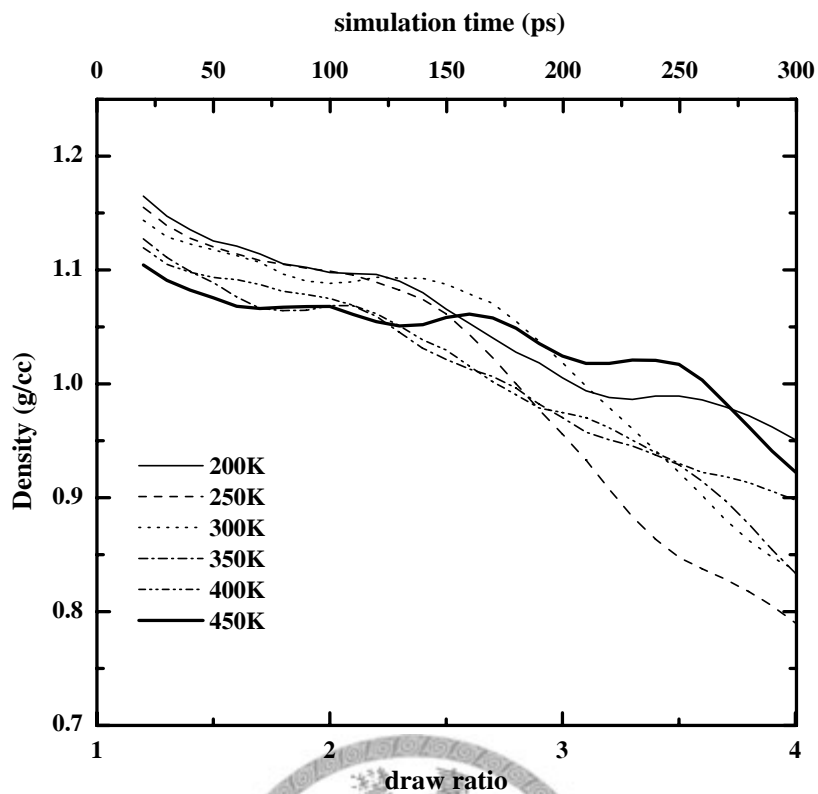


Figure 5.3 The DR variation of density at different temperatures with draw speed $1 \times 10^{10} \text{ s}^{-1}$.

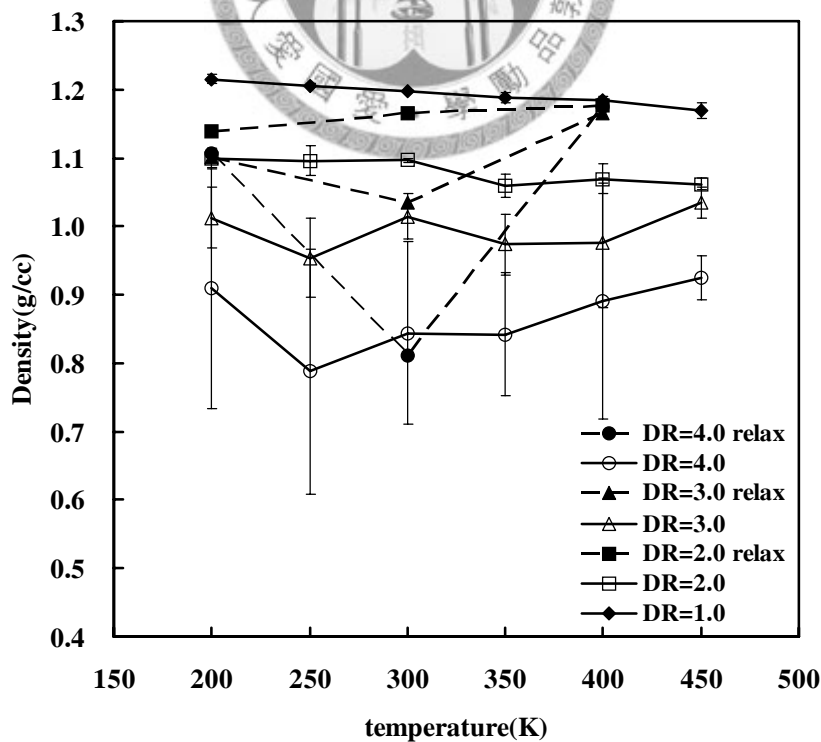


Figure 5.4 The temperature dependence of density at different DR with draw speed $1 \times 10^{10} \text{ s}^{-1}$.

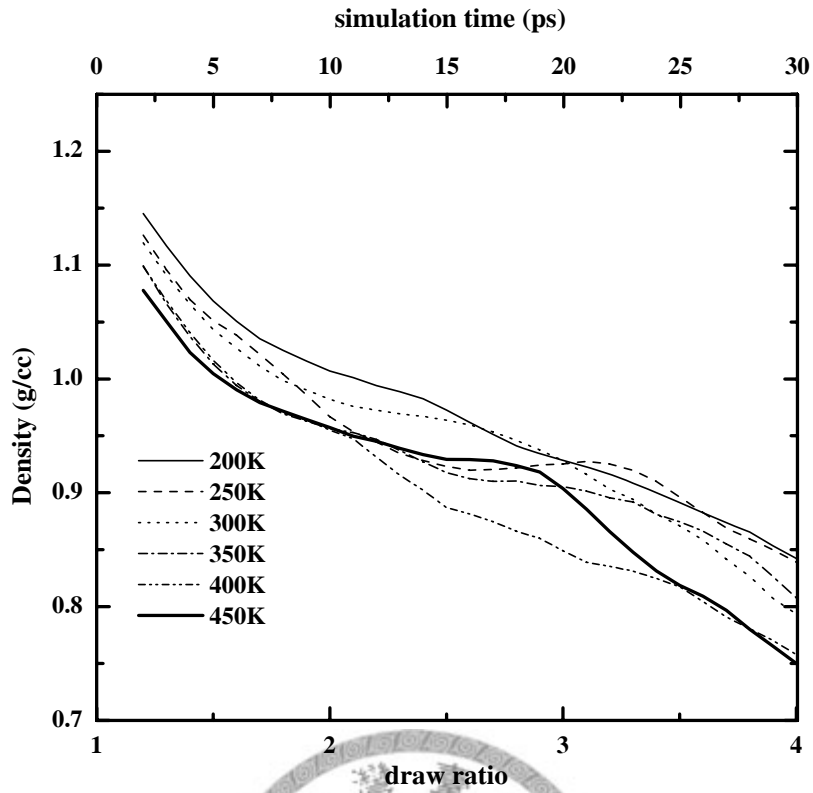


Figure 5.5 The DR variation of density at different temperatures with draw speed $1 \times 10^{11} \text{ s}^{-1}$.

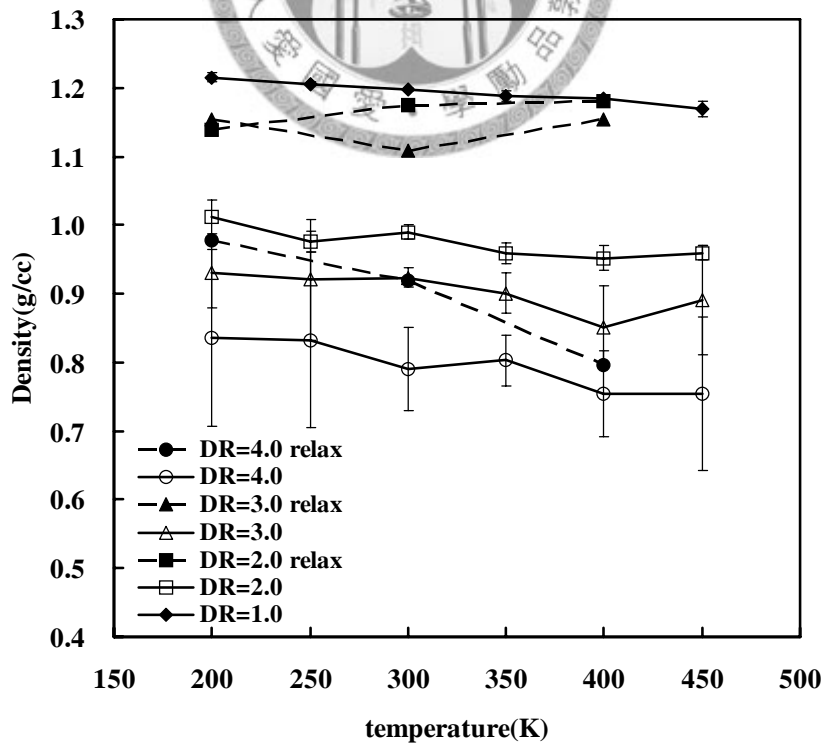


Figure 5.6 The temperature dependence of density at different DR with draw speed $1 \times 10^{11} \text{ s}^{-1}$.

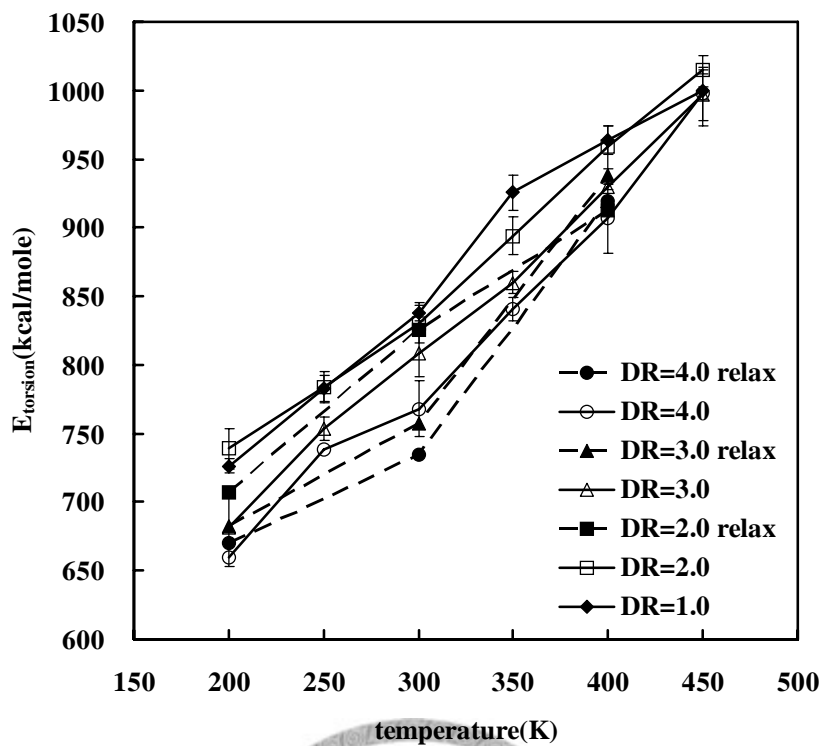


Figure 5.7 The temperature dependence of torsional energy at different DR with draw speed $1 \times 10^9 \text{ s}^{-1}$.

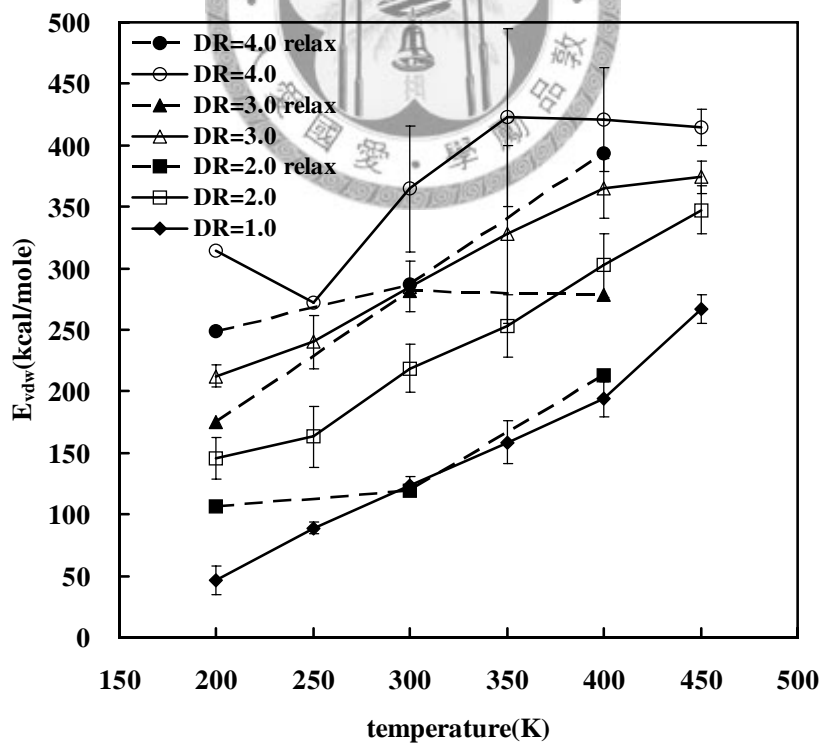


Figure 5.8 The temperature dependence of van der Waals interaction at different DR with draw speed $1 \times 10^9 \text{ s}^{-1}$.

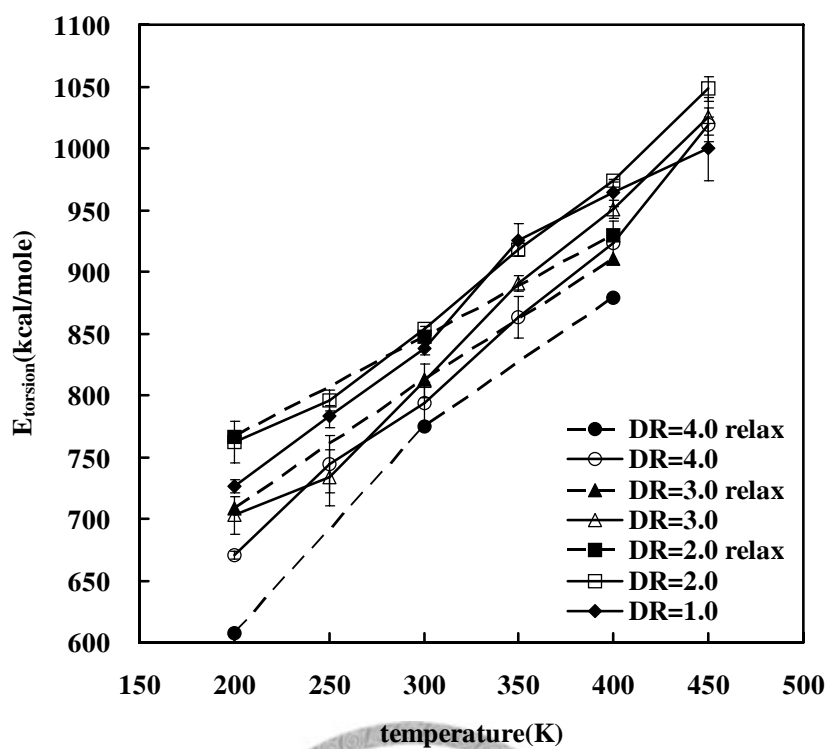


Figure 5.9 The temperature dependence of torsional energy at different DR with draw speed $1 \times 10^{10} \text{ s}^{-1}$.

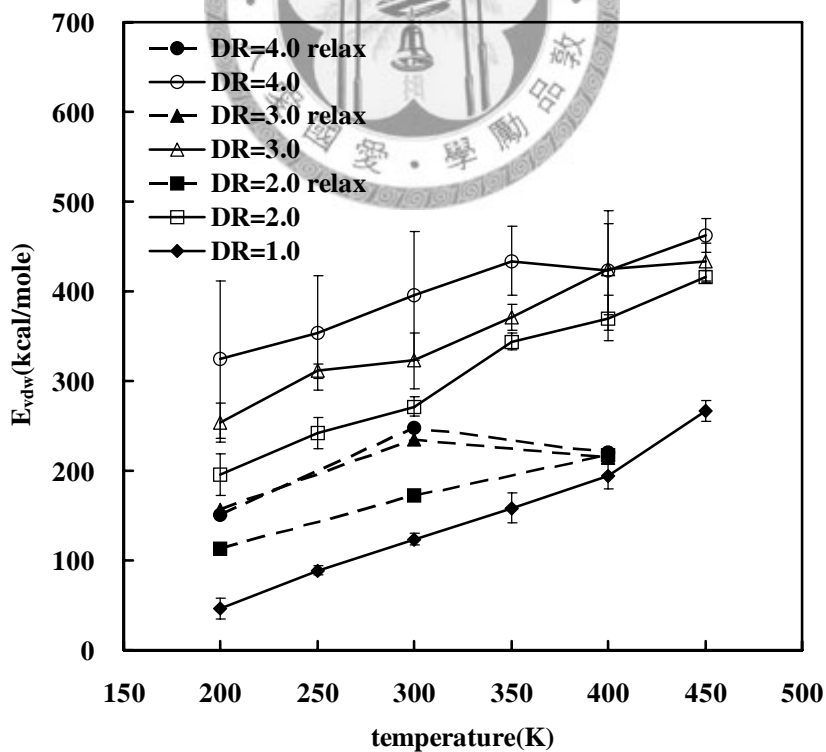


Figure 5.10 The temperature dependence of van der Waals interaction at different DR with draw speed $1 \times 10^{10} \text{ s}^{-1}$.

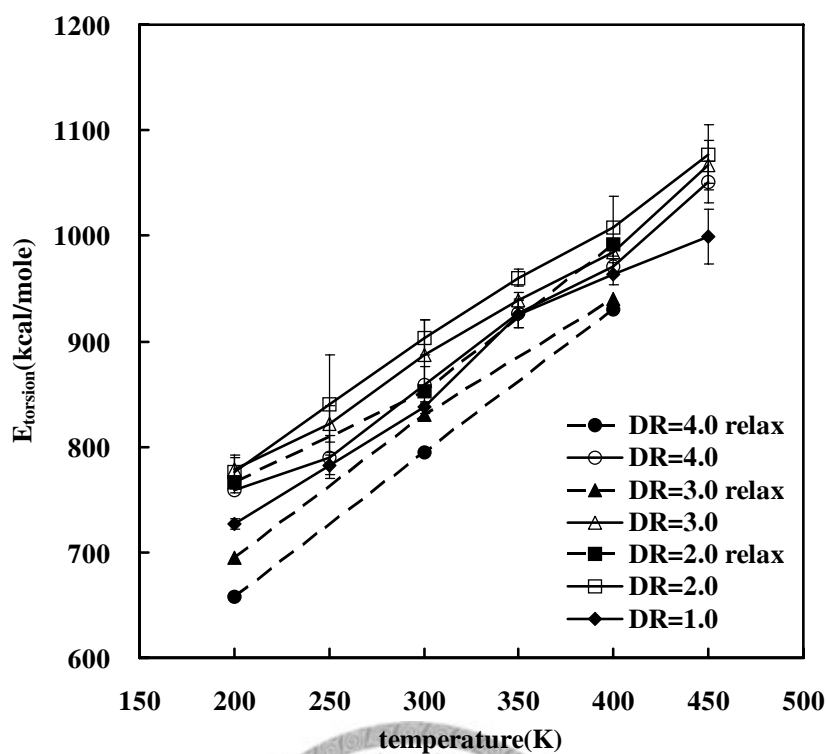


Figure 5.11 The temperature dependence of torsional energy at different DR with draw speed $1 \times 10^{11} \text{ s}^{-1}$.

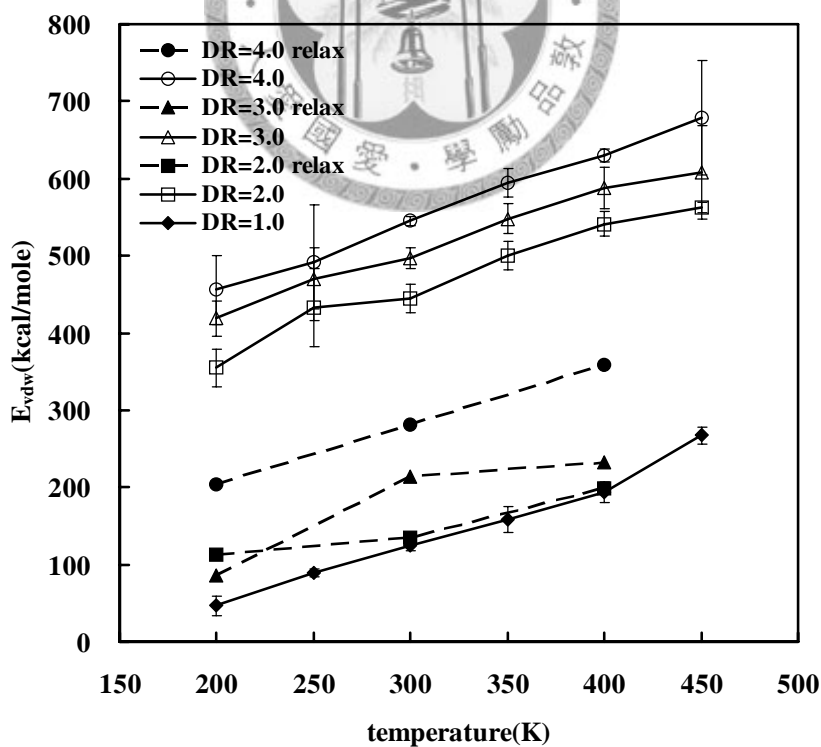


Figure 5.12 The temperature dependence of van der Waals interaction at different DR with draw speed $1 \times 10^{11} \text{ s}^{-1}$.

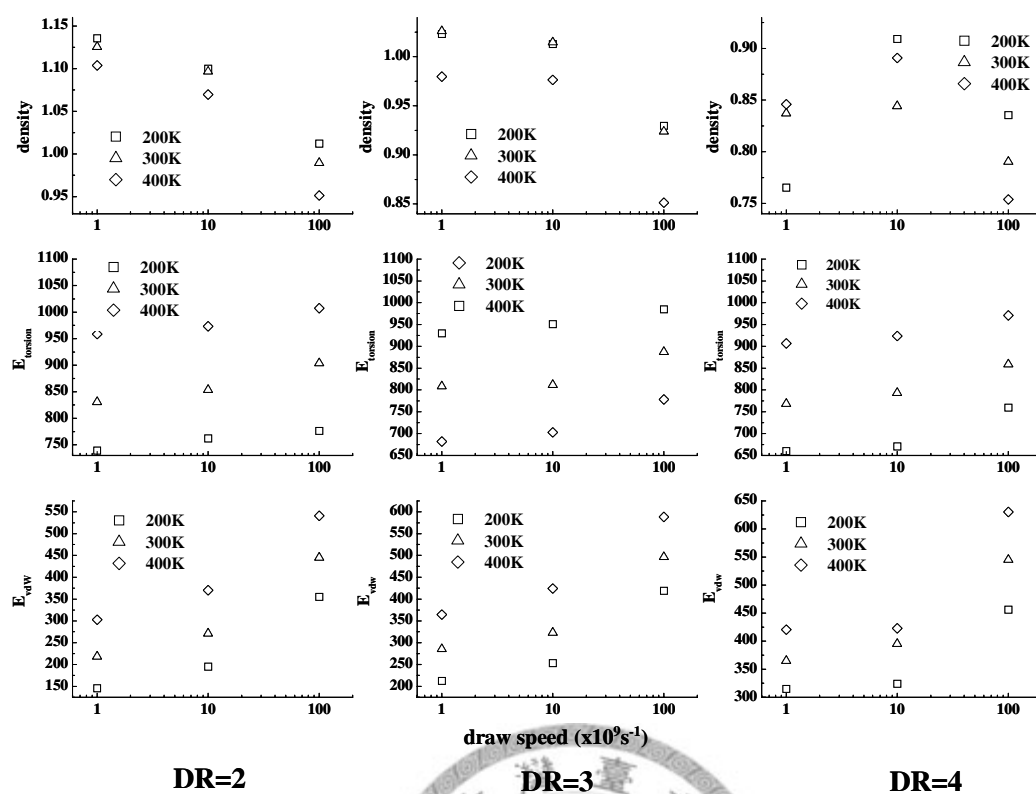


Figure 5.13 The draw speed dependence of density, torsional energy, and van der Waals interaction at different DR.

draw speeds ($1 \times 10^9 \text{ s}^{-1}$, and $1 \times 10^{10} \text{ s}^{-1}$), but fluctuates at the highest draw speed ($1 \times 10^{11} \text{ s}^{-1}$). It is almost a linear function of temperature at constant DR. These results support that the stress effect influences the backbone chain rotation much more than thermal effect.

The coulomb interaction is almost temperature independent. The larger deviation in energy (larger than 100 kcal/more) at higher DR (above DR = 4) indicates that the structure contains lots of defects. Besides, kinetic, bond, angle, and inversion energies all increase linearly with increasing temperature.

5.2 Structure development of the PTT upon drawing

The draw process would create the oriented structures and the amorphous polymer would become heterogenic. In this section we show the results of the structure development, including precursor fraction, degree of order, and torsional angle distribution.

5.2.1 Precursor fraction

In our simulation, the precursor, whose structure has been identified in section 2.6, has been described in various systems with different conditions of stress-induced crystallization. Table 5.4 to Table 5.6 show the fraction of precursor at different conditions. The temperature dependence of the fraction of precursors at DR=2, 3, and 4 in Figure 5.14, Figure 5.15, and Figure 5.16 with draw speed $1 \times 10^9 \text{ s}^{-1}$, $1 \times 10^{10} \text{ s}^{-1}$, and $1 \times 10^{11} \text{ s}^{-1}$, respectively.

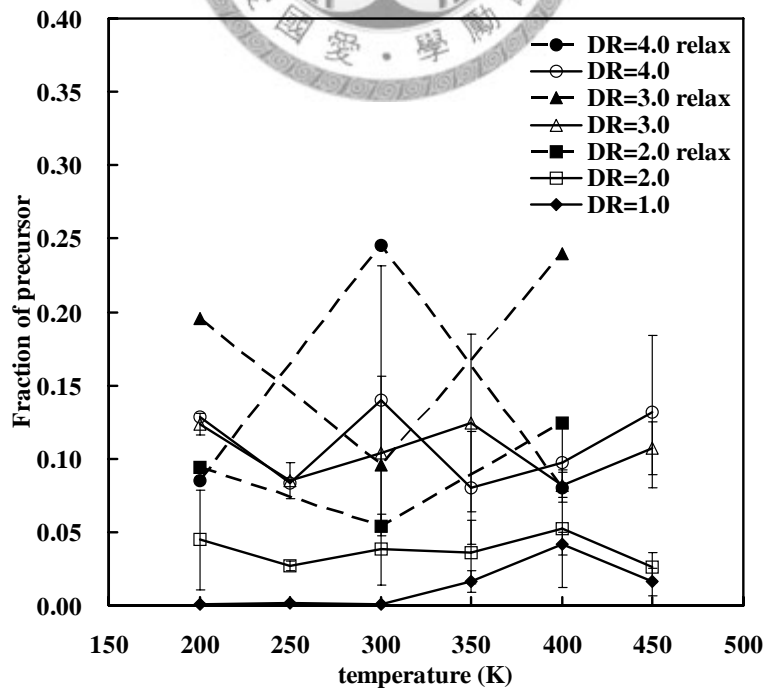


Figure 5.14 The temperature dependence of precursor fraction at different DR with draw speed $1 \times 10^9 \text{ s}^{-1}$.

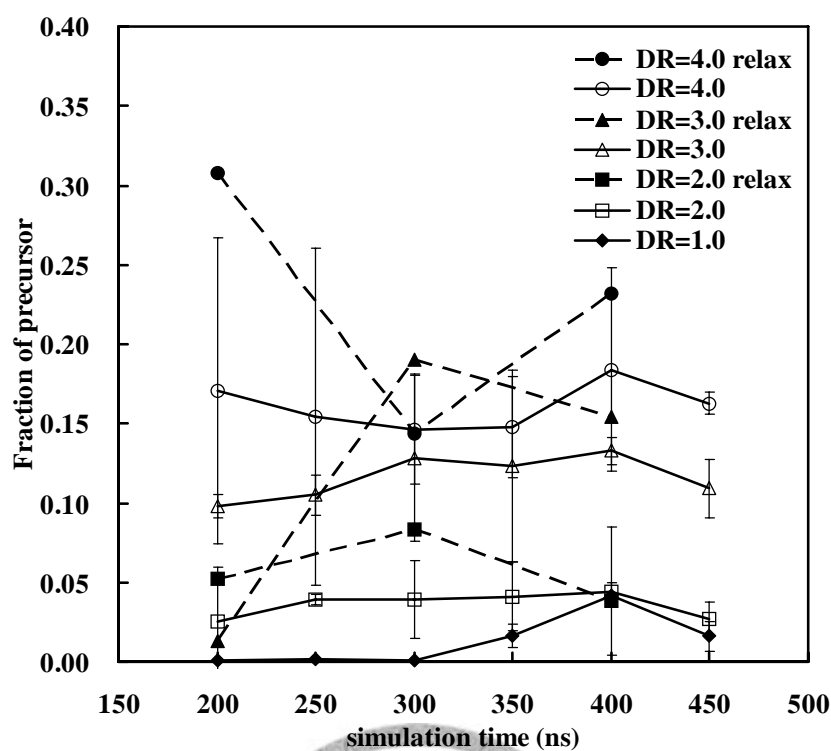


Figure 5.15 The temperature dependence of precursor fraction at different DR with draw speed $1 \times 10^{10} \text{ s}^{-1}$.

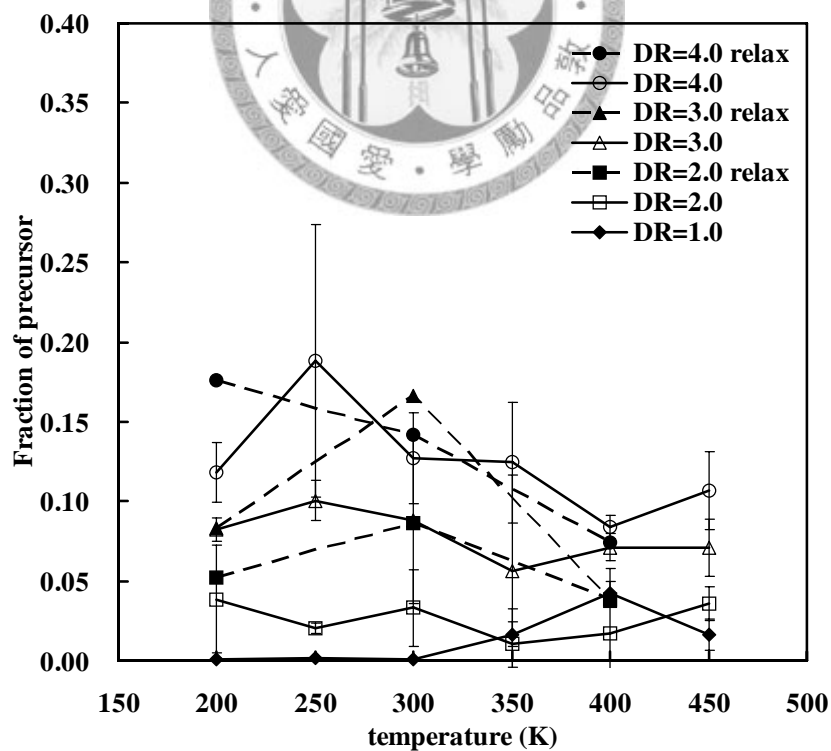


Figure 5.16 The temperature dependence of precursor fraction at different DR with draw speed $1 \times 10^{11} \text{ s}^{-1}$.

Table 5.1 The fraction of precursor with draw speed at $1 \times 10^9 \text{s}^{-1}$.

T (K)	DR=1		DR=1.5		DR=2		DR=2.5		DR=3		DR=3.5		DR=4	
	draw	relax	draw	relax	draw	relax	draw	relax	draw	relax	draw	relax	draw	relax
200	--	0.0008	0.0290	--	0.0446	0.0943	0.0657	--	0.1042	0.1951	0.1210	--	0.1230	0.0852
250	--	0.0046	0.0099	--	0.0270	0.0664	0.0642	--	0.0849	--	0.0848	--	0.0844	--
300	--	0.0011	0.0099	--	0.0383	0.0543	0.0765	--	0.1041	0.0955	0.1193	--	0.1397	0.2452
350	--	0.0159	0.0209	--	0.0363	0.0385	0.0820	--	0.1246	--	0.1469	--	0.1451	--
400	--	0.0389	0.0267	--	0.0527	0.1240	0.0754	--	0.0820	0.2393	0.0862	--	0.0977	0.0798
450	--	0.0138	0.0088	--	0.0259	0.0123	0.0648	--	0.1071	--	0.1348	--	0.1414	--

Table 5.2 The fraction of precursor with draw speed at $1 \times 10^{10} \text{s}^{-1}$.

T (K)	DR=1		DR=1.5		DR=2		DR=2.5		DR=3		DR=3.5		DR=4	
	draw	relax	draw	relax	draw	relax	draw	relax	draw	relax	draw	relax	draw	relax
200	--	0.0008	0.0196	--	0.0255	0.0524	0.0432	--	0.0977	0.0134	0.1500	--	0.1738	0.3075
250	--	0.0046	0.0119	--	0.0389	--	0.0786	--	0.1052	--	0.1321	--	0.1539	--
300	--	0.0011	0.0149	--	0.0392	0.0835	0.0903	--	0.1285	0.1905	0.1372	--	0.1461	0.1437
350	--	0.0159	0.0145	--	0.0410	--	0.0744	--	0.1232	--	0.1501	--	0.1477	--
400	--	0.0389	0.0127	--	0.0445	0.0381	0.0894	--	0.1330	0.1545	0.1613	--	0.1839	0.2316
450	--	0.0138	0.0090	--	0.0270	--	0.0689	--	0.1091	--	0.1440	--	0.1627	--

Table 5.3 The fraction of precursor with draw speed at $1 \times 10^{11} \text{s}^{-1}$.

T (K)	DR=1		DR=1.5		DR=2		DR=2.5		DR=3		DR=3.5		DR=4	
	draw	relax	draw	relax	draw	relax	draw	relax	draw	relax	draw	relax	draw	relax
200	--	0.0008	0.0228	--	0.0387	0.0524	0.0614	--	0.0820	0.0833	0.1053	--	0.1181	0.1759
250	--	0.0046	0.0155	--	0.0207	--	0.0415	--	0.1005	--	0.1660	--	0.1880	--
300	--	0.0011	0.0209	--	0.0332	0.0865	0.0598	--	0.0883	0.1664	0.1161	--	0.1270	0.1416
350	--	0.0159	0.0063	--	0.0109	--	0.0278	--	0.0562	--	0.0984	--	0.1244	--
400	--	0.0389	0.0068	--	0.0175	0.0381	0.0394	--	0.0710	0.0377	0.0807	--	0.0839	0.0740
450	--	0.0138	0.0191	--	0.0362	--	0.0545	--	0.0709	--	0.0918	--	0.1068	--

5.2.2 Degree of Order

We use the same analysis methods (DRF, and orientation factor) to understand the development of internal structures. **Figure 5.17**, **Figure 5.18**, and **Figure 5.19** show the results of RDF with draw speed $1 \times 10^9 \text{ s}^{-1}$, $1 \times 10^{10} \text{ s}^{-1}$, and $1 \times 10^{11} \text{ s}^{-1}$, respectively. **Figure 5.20** shows the orientation factor depend on DR.

5.2.3 Torsional angle transition

From section 1.5, we know that the mechanism of torsional angle transition during stress-induced crystallization is questionable. **Table 5.7~ Table 5.9** shows the fraction of trans and gauche state, and also shows the trans-to-gauche ratio in ϕ_1 and the gauche-to-trans ratio in ϕ_2 in different conditions. We show the percentage of trans state (in **Figure 5.21**, **Figure 5.22**, and **Figure 5.23**), percentage of gauche state (in **Figure 5.24**, **Figure 5.25**, and **Figure 5.26**), the trans-to-gauche ratio in ϕ_1 (in **Figure 5.27**, **Figure 5.28**, and **Figure 5.29**), and the gauche-to-trans ratio in ϕ_2 (in **Figure 5.30**, **Figure 5.31**, and **Figure 5.32**) depends on temperature at DR=2, 3, and 4 with draw speed $1 \times 10^9 \text{ s}^{-1}$, $1 \times 10^{10} \text{ s}^{-1}$, and $1 \times 10^{11} \text{ s}^{-1}$, respectively.

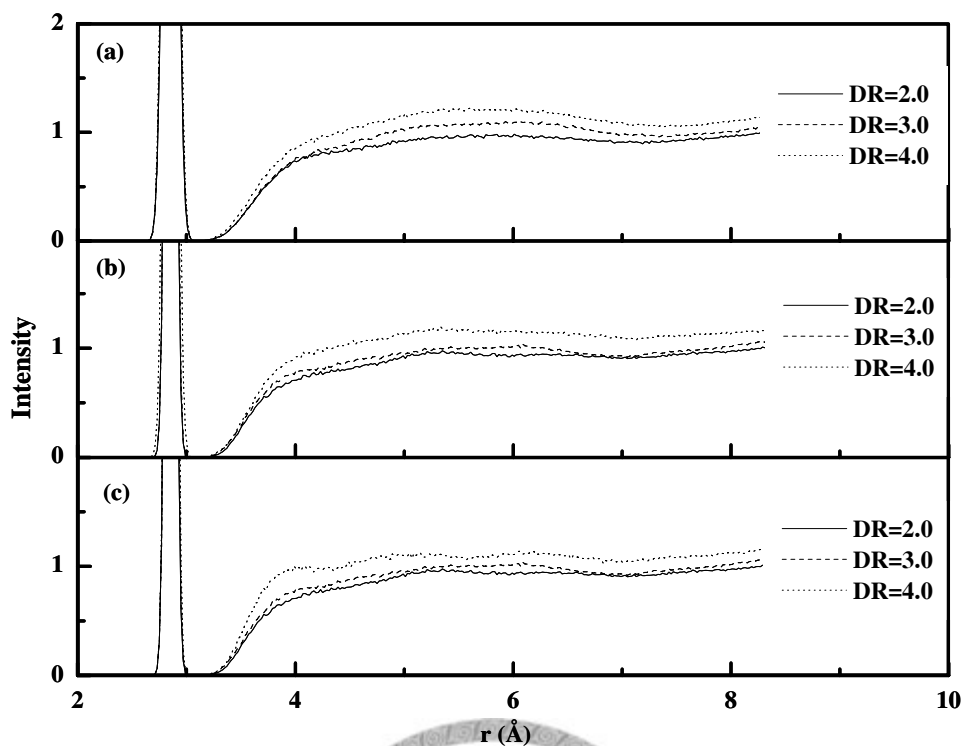


Figure 5.17 The DR variation of RDF at (a) 400K, (b) 300K, and (c) 200K with draw speed $1 \times 10^9 \text{ s}^{-1}$.

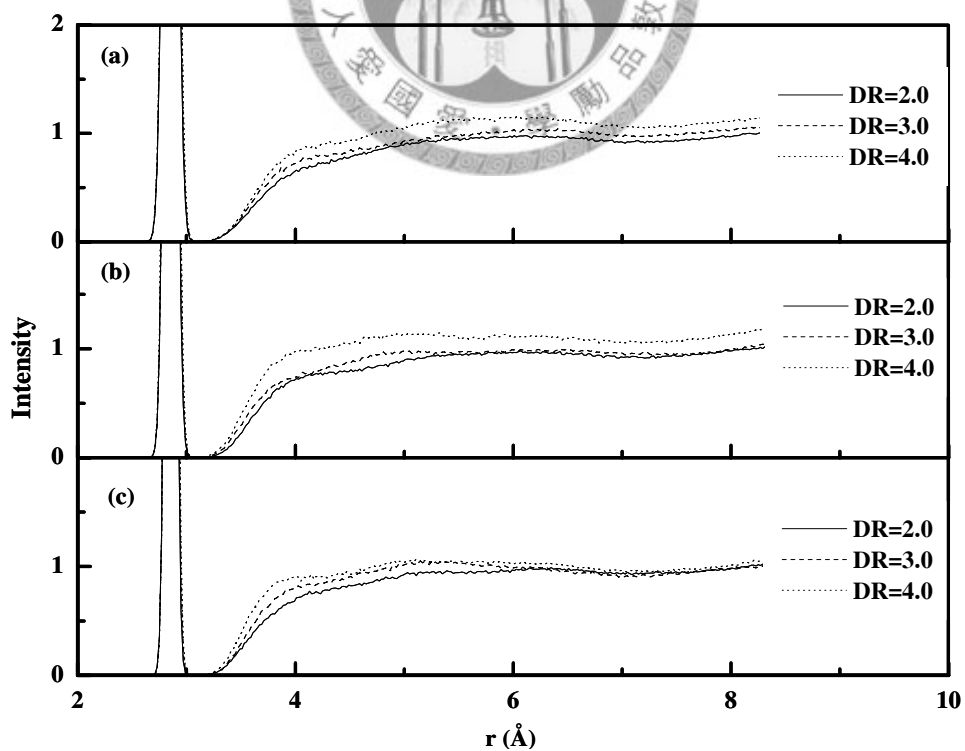


Figure 5.18 The DR variation of RDF at (a) 400K, (b) 300K, and (c) 200K with draw speed $1 \times 10^{10} \text{ s}^{-1}$.

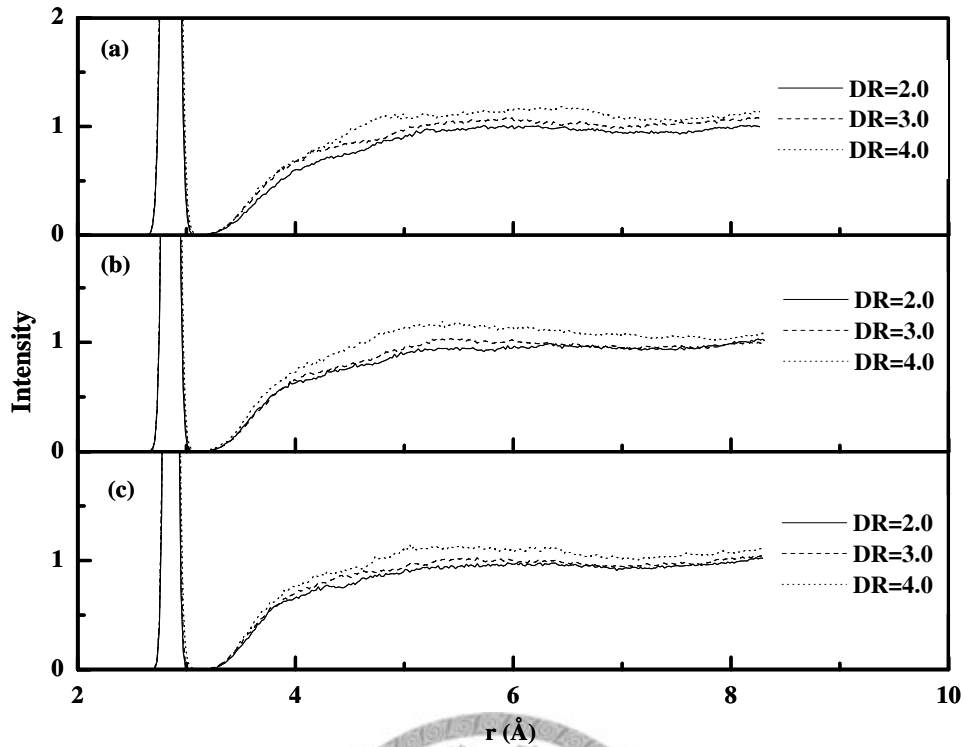


Figure 5.19 The DR variation of RDF at (a) 400K, (b) 300K, and (c) 200K with draw speed $1 \times 10^{11} \text{ s}^{-1}$.

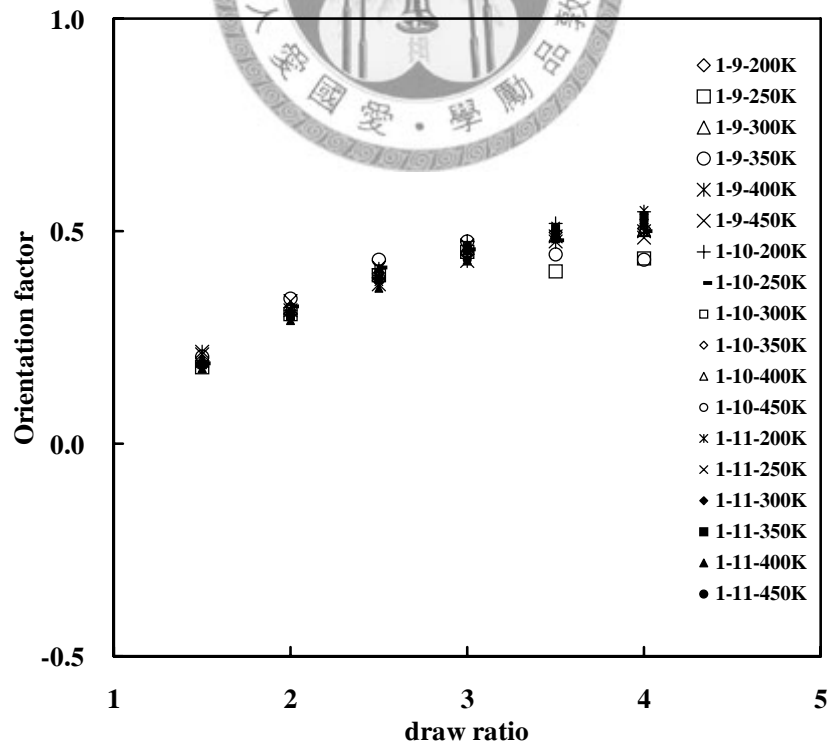


Figure 5.20 The results of orientation factor at various temperatures and DR.

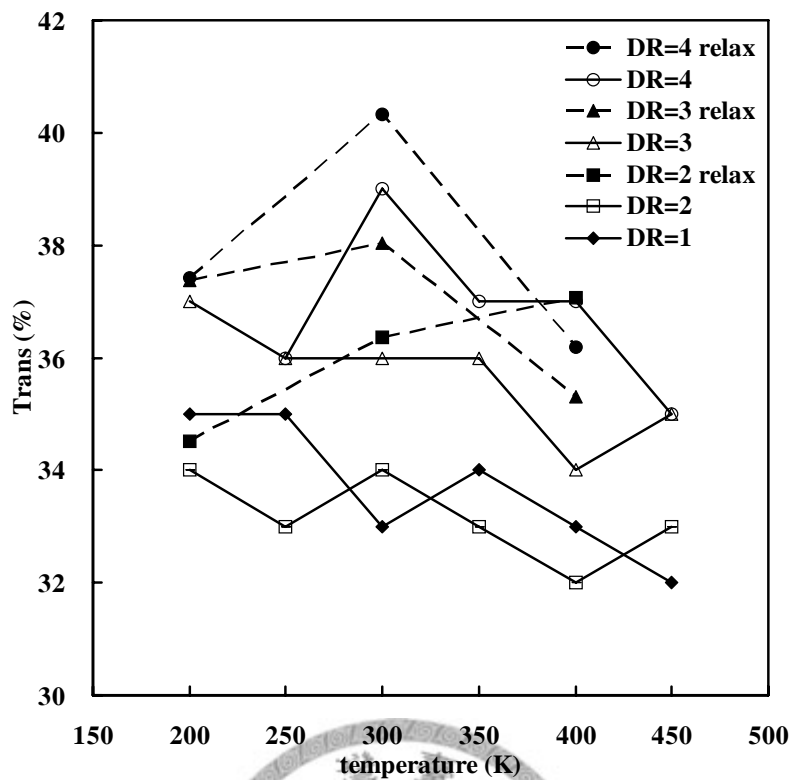


Figure 5.21 The percentage of trans state depends on temperature at DR=2, 3, and 4 with draw speed $1 \times 10^9 \text{ s}^{-1}$.

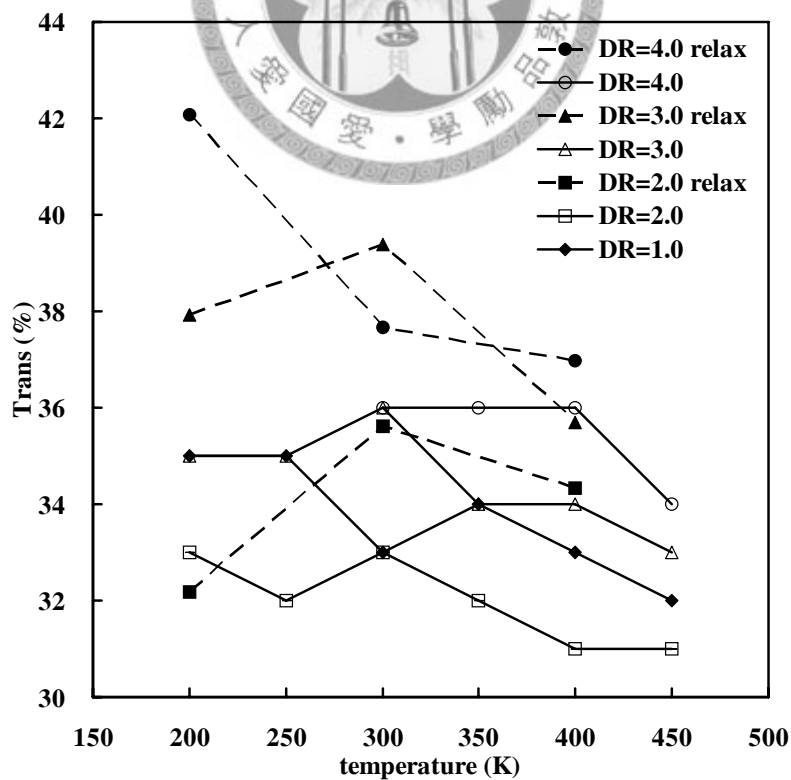


Figure 5.22 The percentage of trans state depends on temperature at DR=2, 3, and 4 with draw speed $1 \times 10^{10} \text{ s}^{-1}$.

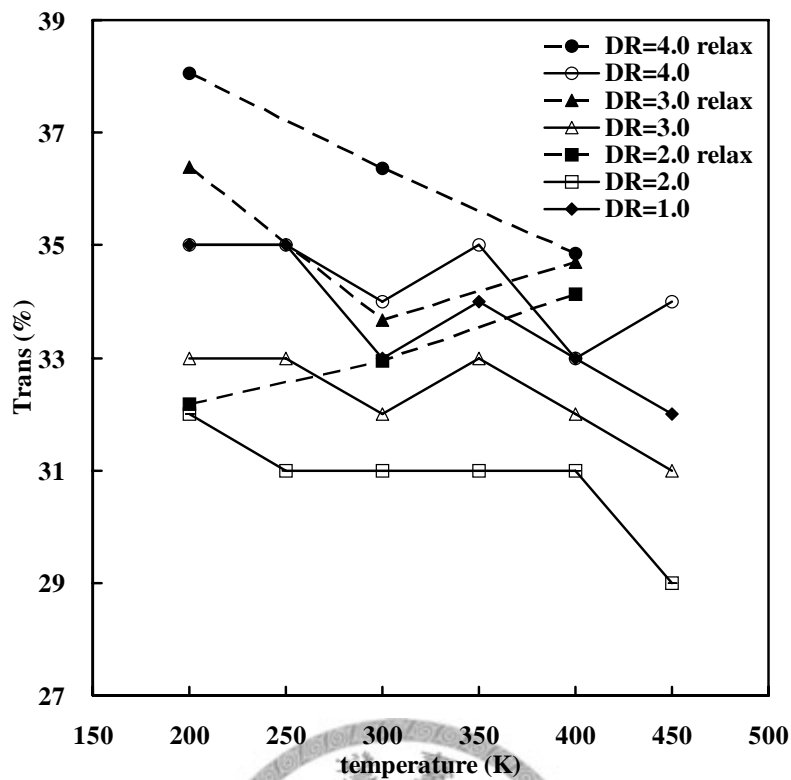


Figure 5.23 The percentage of trans state depends on temperature at DR=2, 3, and 4 with draw speed $1 \times 10^{11} \text{ s}^{-1}$.

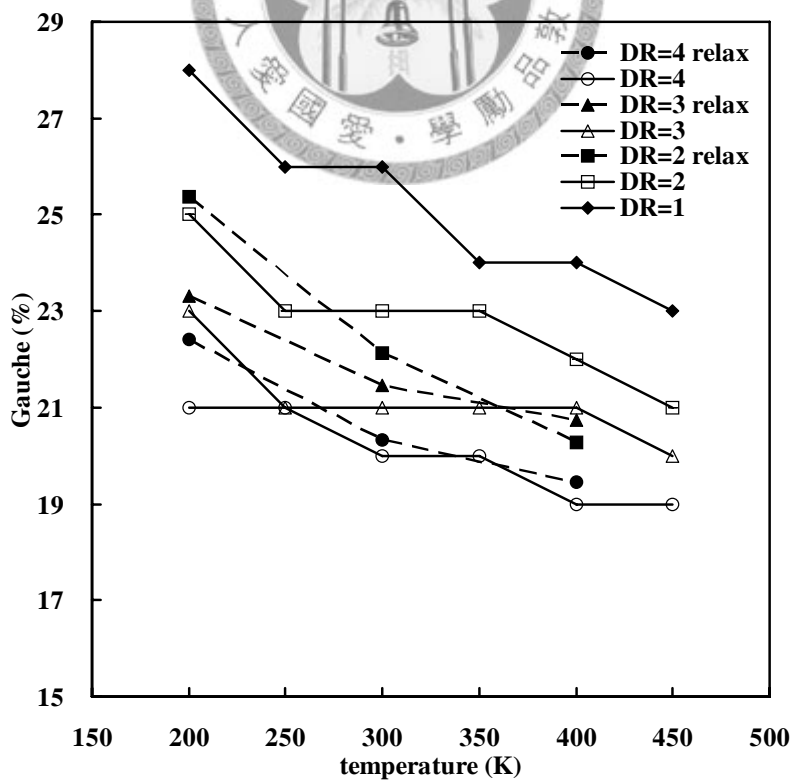


Figure 5.24 The percentage of gauche state depends on temperature at DR=2, 3, and 4 with draw speed $1 \times 10^9 \text{ s}^{-1}$.

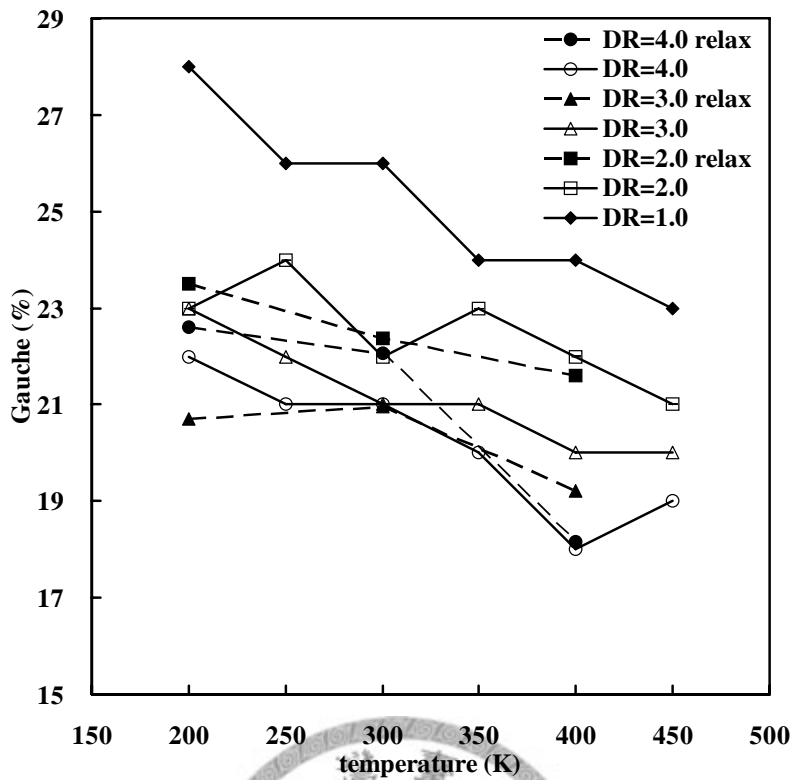


Figure 5.25 The percentage of gauche state depends on temperature at DR=2, 3, and 4 with draw speed $1 \times 10^{10} \text{ s}^{-1}$.

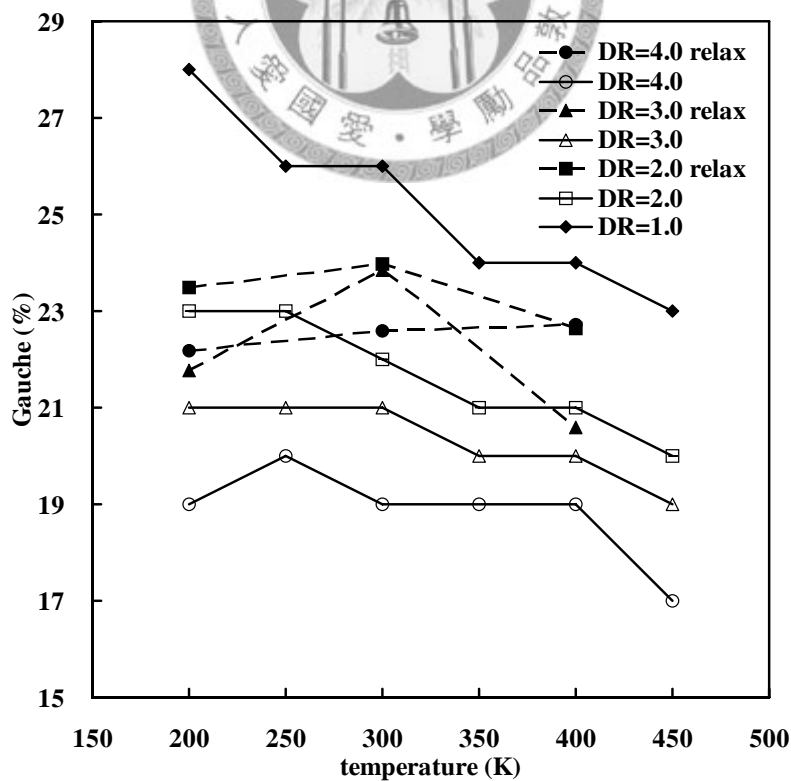


Figure 5.26 The percentage of gauche state depends on temperature at DR=2, 3, and 4 with draw speed $1 \times 10^{11} \text{ s}^{-1}$.

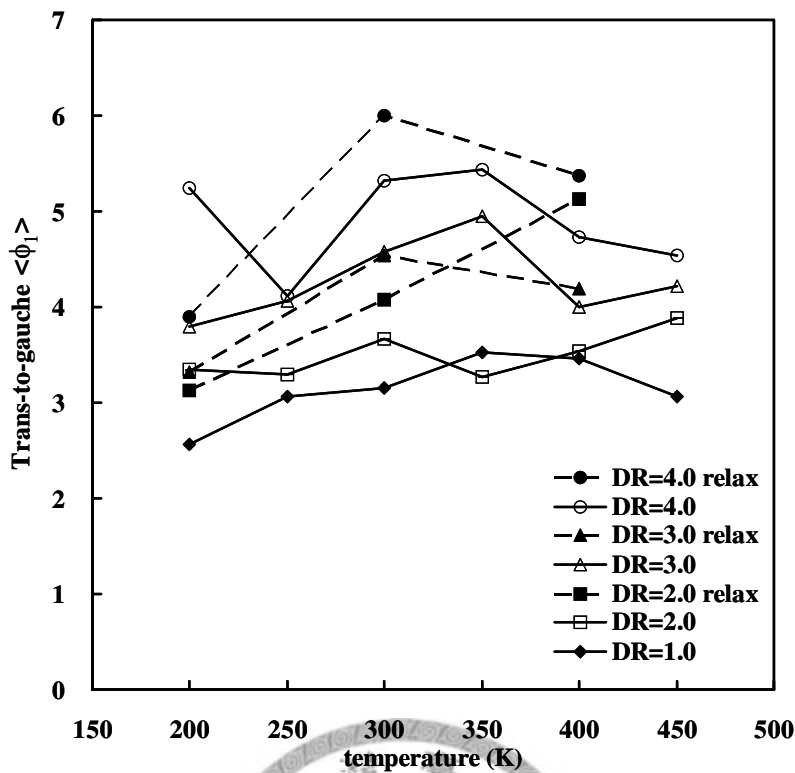


Figure 5.27 The trans-to-gauche ratio in ϕ_1 depends on temperature at DR=2, 3, and 4 with draw speed $1 \times 10^9 \text{ s}^{-1}$.

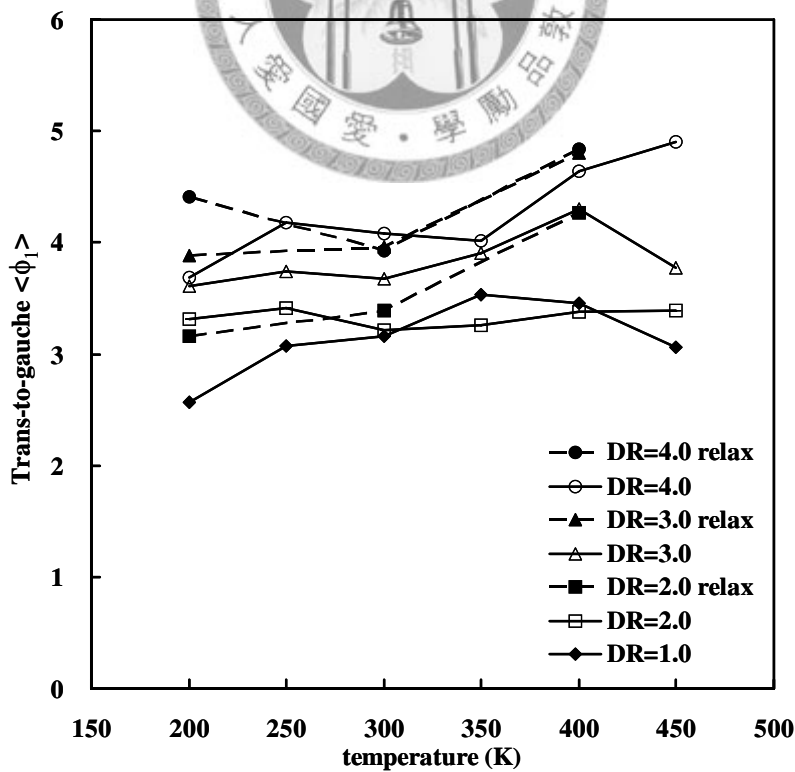


Figure 5.28 The trans-to-gauche ratio in ϕ_1 depends on temperature at DR=2, 3, and 4 with draw speed $1 \times 10^{10} \text{ s}^{-1}$.

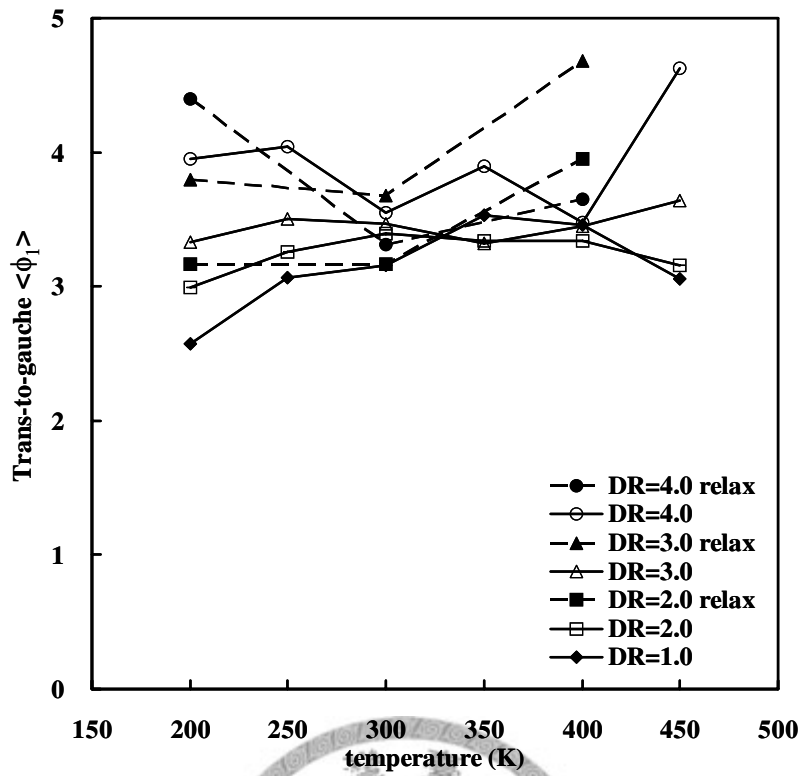


Figure 5.29 The trans-to-gauche ratio in ϕ_1 depends on temperature at DR=2, 3, and 4 with draw speed $1 \times 10^{11} \text{ s}^{-1}$.

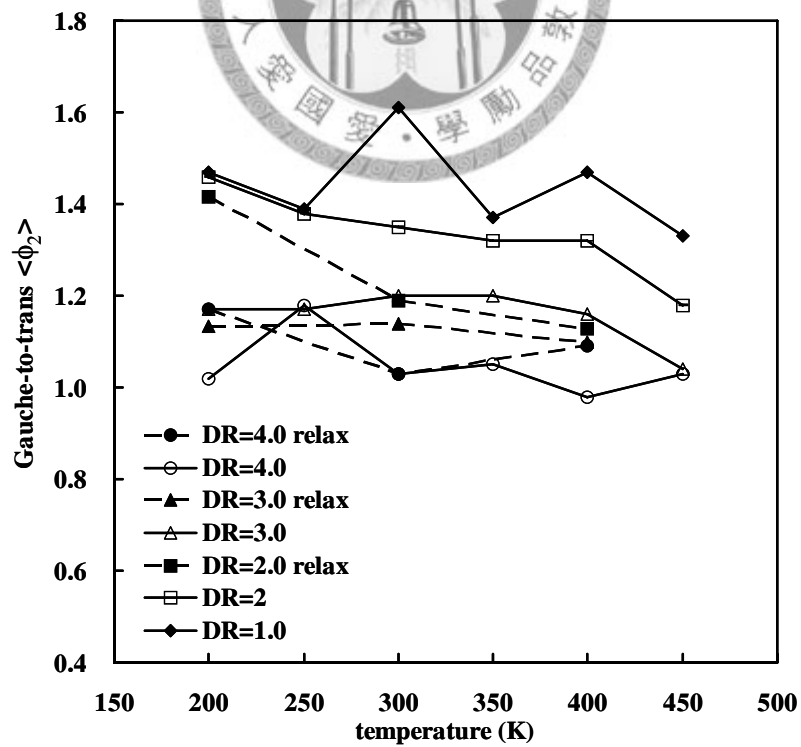


Figure 5.30 The gauche-to-trans ratio in ϕ_2 depends on temperature at DR=2, 3, and 4 with draw speed $1 \times 10^9 \text{ s}^{-1}$.

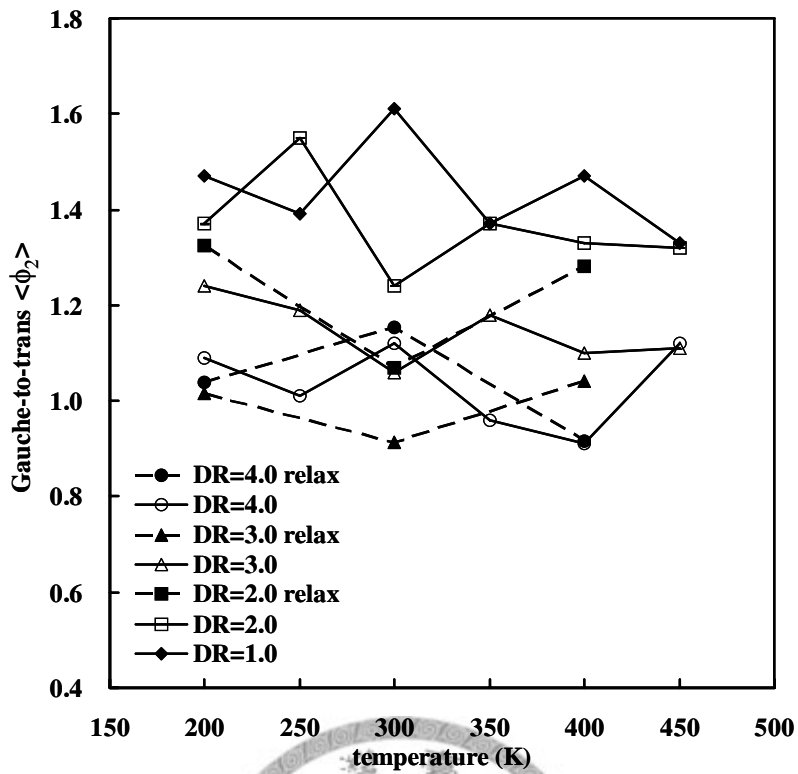


Figure 5.31 The gauche-to-trans ratio in ϕ_2 depends on temperature at DR=2, 3, and 4 with draw speed $1 \times 10^{10} \text{ s}^{-1}$.

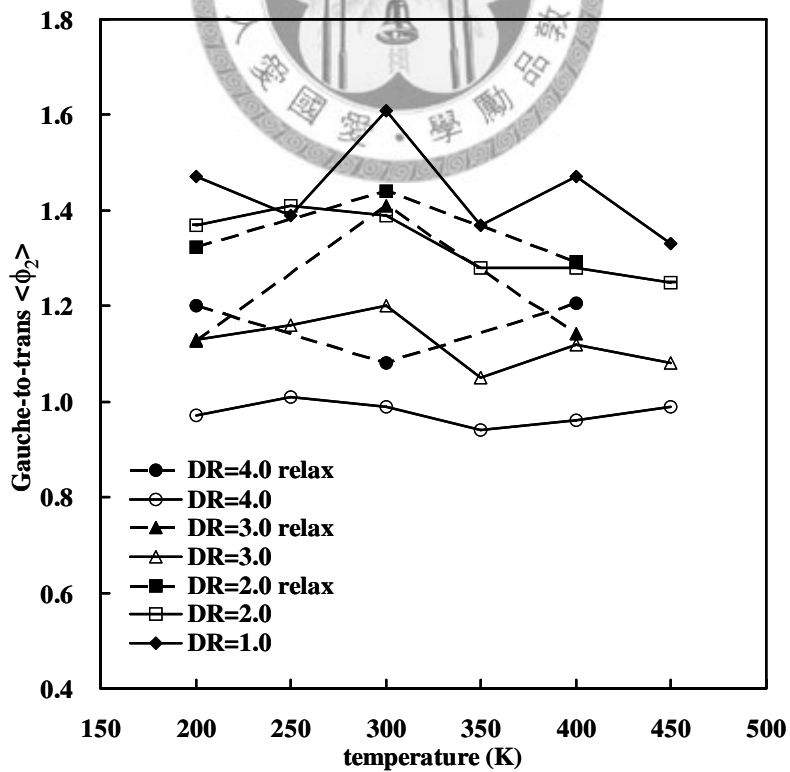


Figure 5.32 The gauche-to-trans ratio in ϕ_2 depends on temperature at DR=2, 3, and 4 with draw speed $1 \times 10^{11} \text{ s}^{-1}$.

Table 5.4 The index of torsional angle with draw speed at $1 \times 10^9 \text{s}^{-1}$.

T (K)	index	DR=1		DR=1.5		DR=2		DR=2.5		DR=3		DR=3.5		DR=4	
		draw	relax	draw	relax	draw	relax	draw	relax	draw	relax	draw	relax	draw	relax
200	trans (%)	--	35	33	--	34	34	35	--	36	37	33	--	41	37
	gauche (%)	--	28	26	--	25	26	24	--	23	23	22	--	21	22
	$\langle \phi_1 \rangle$ t/g	--	2.57	3.28	--	3.34	3.03	3.19	--	3.69	3.31	3.86	--	5.25	3.90
	$\langle \phi_2 \rangle$ g/t	--	1.47	1.66	--	1.46	1.42	1.25	--	1.17	1.13	0.99	--	1.02	1.17
250	trans (%)	--	35	32	--	33	--	35	--	36	--	32	--	36	--
	gauche (%)	--	26	25	--	23	--	22	--	21	--	21	--	21	--
	$\langle \phi_1 \rangle$ t/g	--	3.07	2.90	--	3.29	--	3.73	--	4.07	--	3.69	--	4.11	--
	$\langle \phi_2 \rangle$ g/t	--	1.39	1.54	--	1.38	--	1.25	--	1.17	--	1.01	--	1.18	--
300	trans (%)	--	33	33	--	34	36	35	--	36	38	38	--	39	40
	gauche (%)	--	26	24	--	23	22	22	--	21	21	22	--	20	20
	$\langle \phi_1 \rangle$ t/g	--	3.16	3.61	--	3.67	4.18	3.94	--	4.58	5.54	5.21	--	5.32	6.01
	$\langle \phi_2 \rangle$ g/t	--	1.61	1.51	--	1.35	1.19	1.25	--	1.20	1.14	1.12	--	1.03	1.03
350	trans (%)	--	34	32	--	33	--	35	--	36	--	36	--	38	--
	gauche (%)	--	24	24	--	23	--	21	--	21	--	21	--	20	--
	$\langle \phi_1 \rangle$ t/g	--	3.53	2.98	--	3.27	--	4.15	--	4.95	--	5.14	--	5.43	--
	$\langle \phi_2 \rangle$ g/t	--	1.37	1.41	--	1.32	--	1.23	--	1.20	--	1.15	--	1.05	--
400	trans (%)	--	33	31	--	32	37	34	--	34	35	36	--	37	36
	gauche (%)	--	24	24	--	22	20	21	--	21	21	21	--	19	19
	$\langle \phi_1 \rangle$ t/g	--	3.46	3.02	--	3.54	5.34	3.75	--	4.00	4.19	4.38	--	4.73	5.37
	$\langle \phi_2 \rangle$ g/t	--	1.47	1.43	--	1.32	1.14	1.24	--	1.16	1.10	1.06	--	0.98	1.09
450	trans (%)	--	32	32	--	33	--	34	--	35	--	35	--	35	--
	gauche (%)	--	23	22	--	21	--	20	--	20	--	20	--	19	--
	$\langle \phi_1 \rangle$ t/g	--	3.06	3.27	--	3.88	--	4.19	--	4.22	--	4.54	--	4.54	--
	$\langle \phi_2 \rangle$ g/t	--	1.33	1.30	--	1.18	--	1.07	--	1.04	--	1.08	--	1.03	--

Table 5.5 The index of torsional angle with draw speed at $1 \times 10^{10} \text{s}^{-1}$

T (K)	index	DR=1		DR=1.5		DR=2		DR=2.5		DR=3		DR=3.5		DR=4	
		draw	relax	draw	relax	draw	relax	draw	relax	draw	relax	draw	relax	draw	relax
200	trans (%)	--	35	33	--	33	32	34	--	35	38	36	--	37	42
	gauche (%)	--	28	25	--	23	23	23	--	23	21	23	--	22	23
	$\langle \phi_1 \rangle$ t/g	--	2.57	3.23	--	3.31	3.16	3.55	--	3.61	3.88	3.58	--	3.69	4.41
	$\langle \phi_2 \rangle$ g/t	--	1.47	1.52	--	1.37	1.32	1.31	--	1.24	1.02	1.15	--	1.09	1.04
250	trans (%)	--	35	32	--	32	--	34	--	35	--	36	--	37	--
	gauche (%)	--	26	25	--	24	--	23	--	22	--	22	--	21	--
	$\langle \phi_1 \rangle$ t/g	--	3.07	3.28	--	3.41	--	3.50	--	3.74	--	3.91	--	4.18	--
	$\langle \phi_2 \rangle$ g/t	--	1.39	1.67	--	1.55	--	1.31	--	1.19	--	1.12	--	1.01	--
300	trans (%)	--	33	33	--	33	36	34	--	36	39	36	--	36	38
	gauche (%)	--	26	23	--	22	22	21	--	21	21	21	--	21	22
	$\langle \phi_1 \rangle$ t/g	--	3.16	3.31	--	3.21	3.39	3.37	--	3.67	3.96	3.98	--	4.08	3.93
	$\langle \phi_2 \rangle$ g/t	--	1.61	1.37	--	1.24	1.07	1.11	--	1.06	0.91	1.10	--	1.12	1.15
350	trans (%)	--	34	31	--	32	--	32	--	34	--	35	--	36	--
	gauche (%)	--	24	24	--	23	--	22	--	21	--	21	--	20	--
	$\langle \phi_1 \rangle$ t/g	--	3.53	3.21	--	3.26	--	3.59	--	3.91	--	3.97	--	4.01	--
	$\langle \phi_2 \rangle$ g/t	--	1.37	1.54	--	1.37	--	1.27	--	1.18	--	1.04	--	0.96	--
400	trans (%)	--	33	30	--	31	34	32	--	34	36	35	--	36	37
	gauche (%)	--	24	23	--	22	22	21	--	20	19	20	--	18	18
	$\langle \phi_1 \rangle$ t/g	--	3.46	3.12	--	3.38	4.27	3.91	--	4.30	4.80	4.42	--	4.64	4.83
	$\langle \phi_2 \rangle$ g/t	--	1.47	1.44	--	1.33	1.28	1.21	--	1.10	1.04	1.00	--	0.91	0.92
450	trans (%)	--	32	30	--	31	--	32	--	33	--	33	--	34	--
	gauche (%)	--	23	22	--	21	--	20	--	20	--	20	--	19	--
	$\langle \phi_1 \rangle$ t/g	--	3.06	2.85	--	3.39	--	3.64	--	3.77	--	4.17	--	4.90	--
	$\langle \phi_2 \rangle$ g/t	--	1.33	1.33	--	1.32	--	1.19	--	1.11	--	1.13	--	1.12	--

Table 5.6 The index of torsional angle with draw speed at $1 \times 10^{11} \text{ s}^{-1}$

T (K)		DR=1		DR=1.5		DR=2		DR=2.5		DR=3		DR=3.5		DR=4	
		draw	relax	draw	relax	draw	relax	draw	relax	draw	relax	draw	relax	draw	relax
200	trans (%)	--	35	33	--	32	32	32	--	33	36	34	--	35	38
	gauche (%)	--	28	25	--	23	23	22	--	21	22	21	--	19	22
	$\langle \phi_1 \rangle$ t/g	--	2.57	2.96	--	2.99	3.16	3.14	--	3.33	3.79	3.67	--	3.95	4.39
	$\langle \phi_2 \rangle$ g/t	--	1.47	1.43	--	1.37	1.32	1.28	--	1.13	1.13	1.02	--	0.97	1.20
250	trans (%)	--	35	32	--	31	--	32	--	33	--	34	--	35	--
	gauche (%)	--	26	25	--	23	--	21	--	21	--	20	--	20	--
	$\langle \phi_1 \rangle$ t/g	--	3.07	3.01	--	3.26	--	3.35	--	3.50	--	3.84	--	4.04	--
	$\langle \phi_2 \rangle$ g/t	--	1.39	1.55	--	1.41	--	1.27	--	1.16	--	1.09	--	1.01	--
300	trans (%)	--	33	32	--	31	33	31	--	32	34	33	--	34	36
	gauche (%)	--	26	24	--	22	24	21	--	21	24	21	--	19	23
	$\langle \phi_1 \rangle$ t/g	--	3.16	3.25	--	3.39	3.17	3.48	--	3.47	3.68	3.41	--	3.55	3.31
	$\langle \phi_2 \rangle$ g/t	--	1.61	1.51	--	1.39	1.44	1.31	--	1.20	1.41	1.06	--	0.99	1.08
350	trans (%)	--	34	32	--	31	--	32	--	33	--	34	--	35	--
	gauche (%)	--	24	23	--	21	--	20	--	20	--	20	--	19	--
	$\langle \phi_1 \rangle$ t/g	--	3.53	3.37	--	3.34	--	3.24	--	3.32	--	3.56	--	3.90	--
	$\langle \phi_2 \rangle$ g/t	--	1.37	1.43	--	1.28	--	1.14	--	1.05	--	1.00	--	0.94	--
400	trans (%)	--	33	30	--	31	33	30	--	32	35	33	--	33	35
	gauche (%)	--	24	23	--	21	24	20	--	20	21	20	--	19	23
	$\langle \phi_1 \rangle$ t/g	--	3.46	3.13	--	3.34	3.95	3.44	--	3.45	4.68	3.44	--	3.48	3.65
	$\langle \phi_2 \rangle$ g/t	--	1.47	1.45	--	1.28	1.29	1.19	--	1.12	1.14	1.03	--	0.96	1.21
450	trans (%)	--	32	30	--	29	--	30	--	31	--	33	--	34	--
	gauche (%)	--	23	22	--	20	--	19	--	19	--	19	--	17	--
	$\langle \phi_1 \rangle$ t/g	--	3.06	2.98	--	3.16	--	3.46	--	3.64	--	4.03	--	4.63	--
	$\langle \phi_2 \rangle$ g/t	--	1.33	1.36	--	1.25	--	1.20	--	1.08	--	0.94	--	0.99	--

5.2.4 Discussion

The changes in bulk properties are observed during stress-induced crystallization in our simulation. The increase of amount of precursor increases in the draw process is much more remarkable than that in isothermal crystallization. Furthermore, the subsequent process of relaxation (after the drawing process) would improve the fraction of oriented precursors.

At small DR (DR=2), the fraction of precursors increases in all temperatures with slower draw speeds ($1 \times 10^9 \text{s}^{-1}$ and $1 \times 10^{10} \text{s}^{-1}$), but it decreases at temperatures 350K and 400K with higher draw speed ($1 \times 10^{11} \text{s}^{-1}$). At larger DR (DR>3), the saturation of induced precursor is observed in all temperature with the slowest draw speed ($1 \times 10^9 \text{s}^{-1}$); on the contrary, the development of precursor continues at the higher draw speed ($1 \times 10^{10} \text{s}^{-1}$ and $1 \times 10^{11} \text{s}^{-1}$). Besides, the orientation factor increases with DR, and the curves are similar in all situations, indicating that the orientation factor may be a function of draw ratio only. This implies that the stress-induced precursor is similar at the same DR with each draw speed. The several striking lower value points in **Figure 5.20**, which the draw speed are all $1 \times 10^9 \text{s}^{-1}$, support the saturation found in $1 \times 10^9 \text{s}^{-1}$, earlier than other higher draw speeds.

The subsequent thermal relaxation (following the drawing process) could stabilize and facilitate in the growth of oriented precursors. The results of fraction of precursor are also a function of temperature similar with the isothermal crystallization (See **Figure 4.13**), but the highest amount of precursor shift to lower temperature (300K with drawing vs 400 K without drawing). The local motion of polymer segments would be induced by uni-axis stress. (Note the maximum capacity of precursor formation should

be found between the temperature allowing for short range motion and that for entire chain motion.) Comparing the results of isothermal crystallization (**Figure 4.14**), the intensity of RDF at $\sim 4 \text{ \AA}$ obviously increases in all cases.

To understand the distribution of torsional angles of the PTT backbone (O-CH₂-CH₂-CH₂-O) in bulk phase, we analyze the percentage of the trans and gauche states during the stress-induced crystallization. Different behaviors observed at different draw speeds. The percentage of ϕ_1 and ϕ_2 in trans state fluctuates at small DR, and increases at larger DR with slower draw speed. At higher draw speeds, this percentage decreases at small DR and increases at larger DR. The percentage value rebounds to the original value with draw speed $1 \times 10^{11} \text{ s}^{-1}$. On the other hand, the percentage of gauche state decreases with DR at all draw speeds. During thermal relaxation, the percentage of the trans rebounds in all draw speeds, but that of gauche rebounds only in faster draw speed. These suggest that torsional angles change to transition state (i.e., angles region outside our definition in section **2.7 Definition of the torsion angle state**) in the beginning drawing process, and then become trans state at higher DR or under thermal relaxation.

Detailed analysis also are performed on the two feature torsions (ϕ_1 and ϕ_2) in the PTT backbone. It is found that the trans-to-gauche ratio in ϕ_1 increases rapidly (from 3 to 6) at lower drawing speed and higher temperatures; however, the increase is less significant at high drawing speed and low temperatures. In contrast, the gauche-to-trans ratio for ϕ_2 seems to be insensitive to processing conditions (varies from 1.6 to 0.8 regardless of drawing speeds). After thermal relaxation, the value of trans-to-gauche ratio in ϕ_1 improves significantly in the slower draw speeds, but remain almost constant

in the fastest draw speed. On the other hand, the gauche-to-trans ratio for ϕ_2 decreases at small DR with slower draw speeds ($1 \times 10^9 \text{s}^{-1}$ and $1 \times 10^{10} \text{s}^{-1}$), but increases at larger DR with faster draw speed.

Before drawing, the fraction of trans state is $\sim 34\%$, and that of gauche is $\sim 25\%$ in the bulk phase; the most populated conformations in ϕ_1 is trans, and that in ϕ_2 is gauche; i.e., the most populated conformations in the backbone torsions are t-g-g-t (ϕ_1 - ϕ_2 - ϕ_2 - ϕ_1). During draw process, the t-t-t-t conformation increases. Our results are in agreement with the result of Chuch's experimental observation[28]. The thermal relaxation would change the conformations in some of our simulations, but the changes are not obvious.

5.3 Structure development within oriented precursor.

The more detailed structure development of the oriented precursors as a result of the interplay between the van der Waals and torsional forces can be better understood by analyzing the precursor size, radial distribution function (RDF), and torsional angle distributions of each individual precursor identified from section 5.3.1.

5.3.1 Structure identification

We show the number of precursors, and some of their basic properties at temperatures from 300K to 450K with draw speed $1 \times 10^9 \text{s}^{-1}$, $1 \times 10^{10} \text{s}^{-1}$, and $1 \times 10^{11} \text{s}^{-1}$, are summarized in **Table 5.7**, **Table 5.8**, and **Table 5.9**.

Table 5.7 The number and size of individual precursors identified in stress-induced crystallization with draw speed $1 \times 10^9 \text{s}^{-1}$.

Temperature (K)	Number of precursor	Strains (%)
200	5(13,13,8,7,6)	300
250	3(14,8,6)	300
300	4(22,9,8,7)	300
350	3(29,13,7)	300
400	5(16,10,8,5,5)	300
450	4(17,12,9,5)	300



Table 5.8 The number and size of individual precursors identified in stress-induced crystallization with draw speed $1 \times 10^{10} \text{s}^{-1}$.

Temperature (K)	Number of precursor	Strains (%)
200	5(17,12,7,5,5)	300
250	5(22,9,5,5,5)	300
300	3(23,7,5)	300
350	4(20,10,9,7)	300
400	5(20,15,7,5,5,5)	300
450	3(25,12,7)	300

Table 5.9 The number and size of individual precursors identified in stress-induced crystallization with draw speed $1 \times 10^{11} \text{s}^{-1}$.

Temperature (K)	Number of precursor	Strains (%)
200	3(15,7,5)	300
250	4(20,7,7,6)	300
300	6(12,10,8,7,6,6)	300
350	3(14,9,7)	300
400	5(13,7,6,5,5)	300
450	3(19,8,7)	300



5.3.2 The RDF, average size, and torsional angle of precursors

In this section, the results of the maximum size of the precursor in each condition are analyzed using the same method as described in section 4.3. **Figures 5.33, 5.35, and 5.37** show the time evolution of RDF intensity at 4.11\AA , and the average size of precursor at 200K, 300K, and 400K, respectively, with a draw speed of $1 \times 10^9 \text{s}^{-1}$; **Figures 5.39, 5.41, and 5.43** show the results for draw speed $1 \times 10^{10} \text{s}^{-1}$; **Figures 5.45, 5.47, and 5.49** for draw speed $1 \times 10^{11} \text{s}^{-1}$. On the other hand, **Figures 5.34, 5.36, and 5.38** show the results of the fractions of backbone torsions in the oriented precursors at 200K, 300K, and 400K, respectively, with a draw speed $1 \times 10^9 \text{s}^{-1}$; **Figures 5.40, 5.42, and 5.44** show the results for draw speed $1 \times 10^{10} \text{s}^{-1}$; **Figures 5.46, 5.48, and 5.50** for draw speed $1 \times 10^{11} \text{s}^{-1}$. Moreover, the temperature dependence of the growth rate of precursor size (**Figure 5.51**) and that of transition rate of torsional angles (**Figure 5.52**) are analyzed by averaging all of oriented precursors at each temperature.

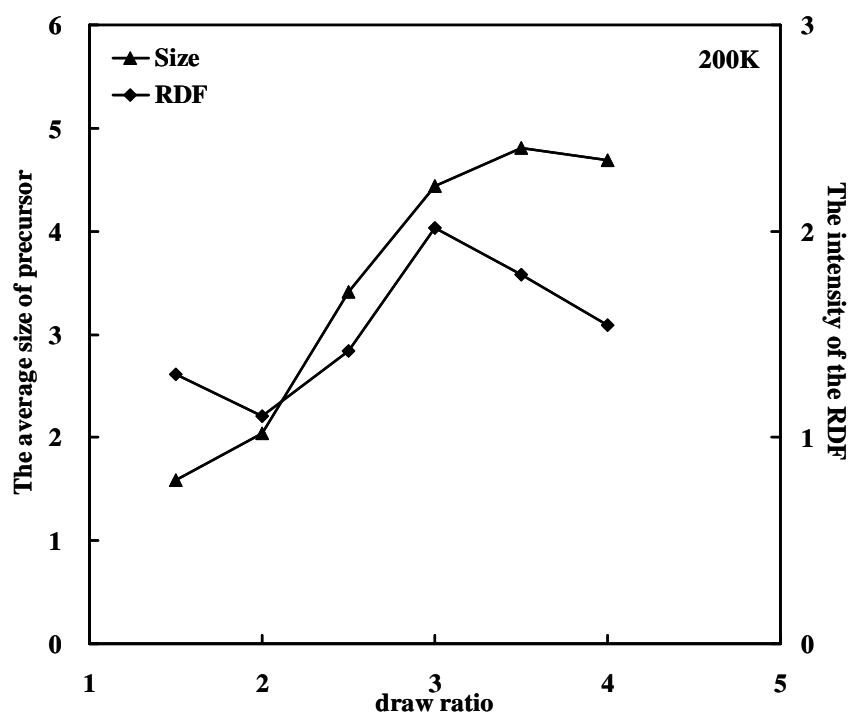


Figure 5.33 The time evolution of RDF intensity (4.11\AA) (diamond) and the time averaged number of parallel segments contained in a representative precursor (triangle) at 200 K with draw speed $1 \times 10^9 \text{s}^{-1}$.

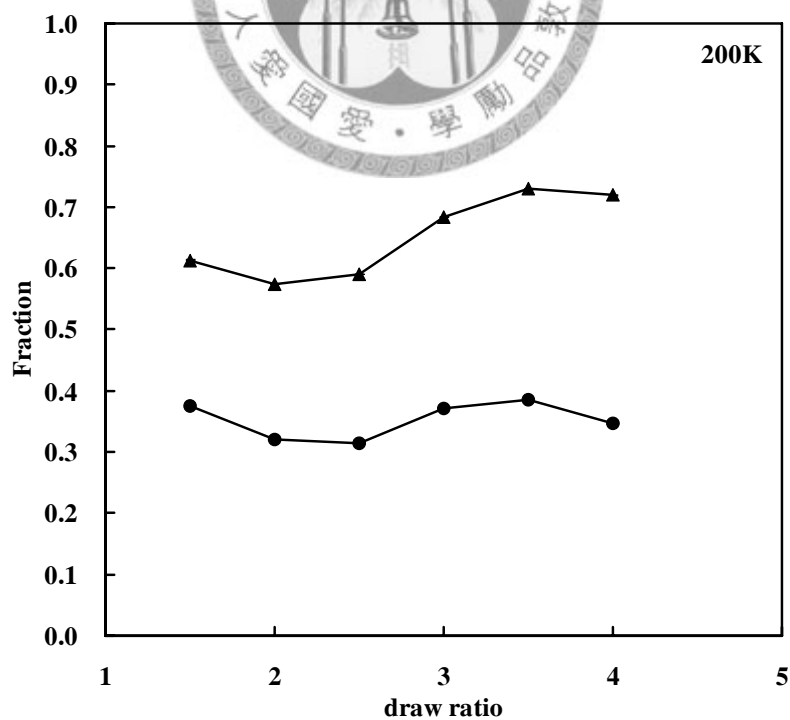


Figure 5.34 The backbone torsions $\langle \phi_1 \rangle$ in trans (triangles) and $\langle \phi_2 \rangle$ in gauche (circles) for segments in a precursor at 200K with draw speed $1 \times 10^9 \text{s}^{-1}$.

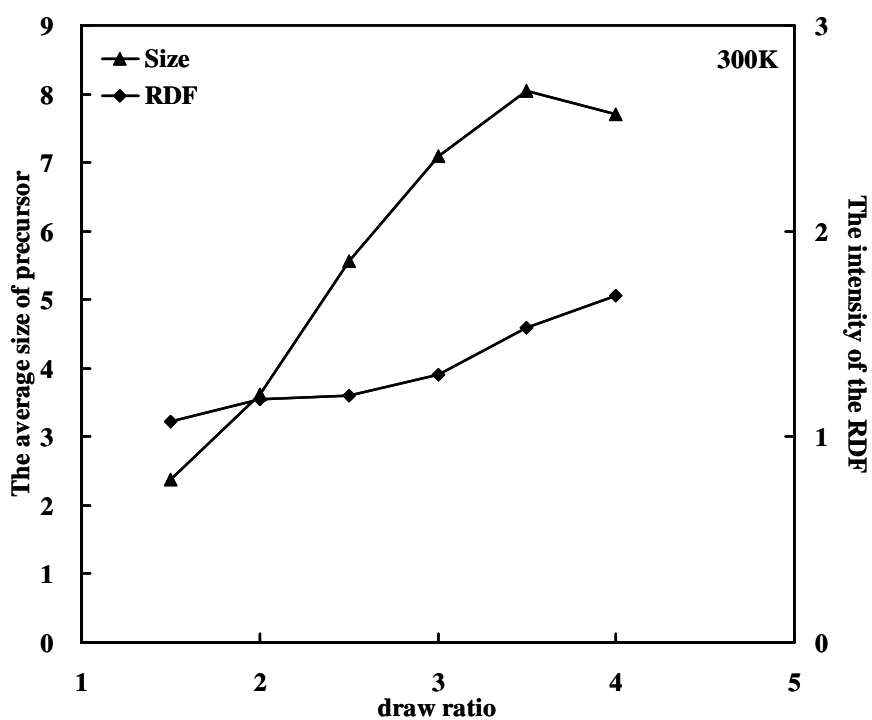


Figure 5.35 The time evolution of RDF intensity (4.11\AA) (diamond) and the time averaged number of parallel segments contained in a representative precursor (triangle) at 300 K with draw speed $1 \times 10^9 \text{s}^{-1}$.

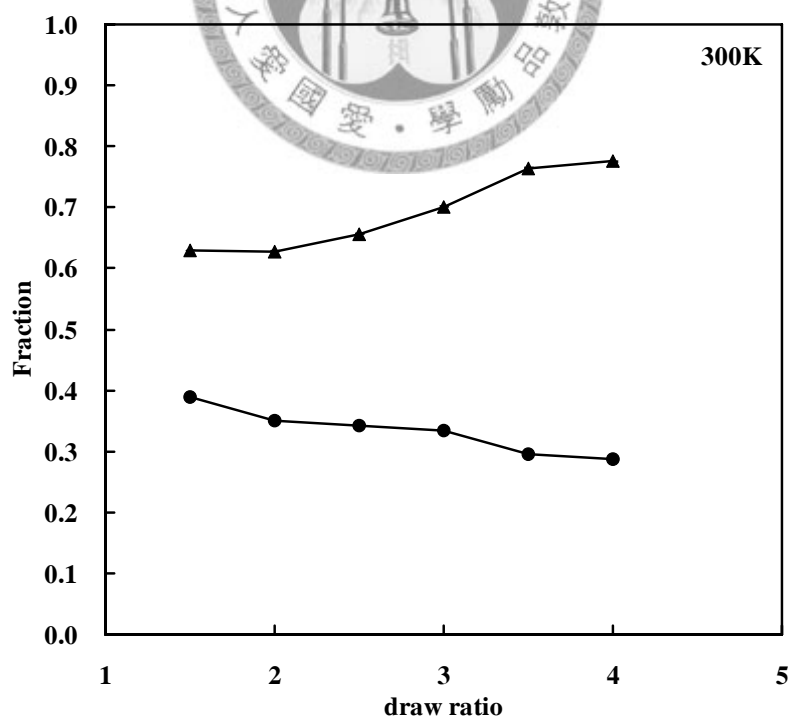


Figure 5.36 The backbone torsions $\langle \phi_1 \rangle$ in trans (triangles) and $\langle \phi_2 \rangle$ in gauche (circles) for segments in a precursor at 300K with draw speed $1 \times 10^9 \text{s}^{-1}$.

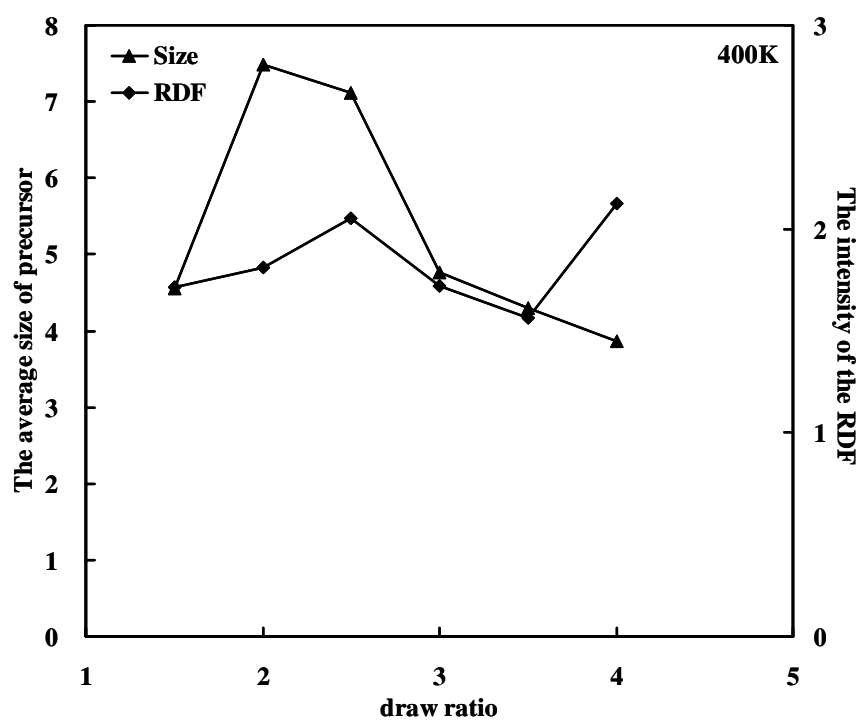


Figure 5.37 The time evolution of RDF intensity (4.11 Å) (diamond) and the time averaged number of parallel segments contained in a representative precursor (triangle) at 400 K with draw speed $1 \times 10^9 \text{ s}^{-1}$.

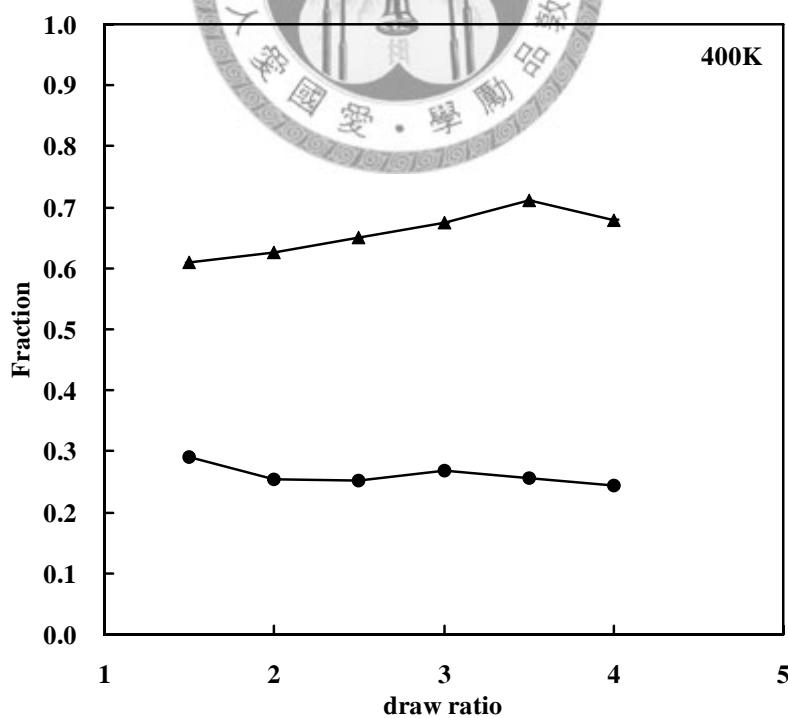


Figure 5.38 The backbone torsions $\langle \phi_1 \rangle$ in trans (triangles) and $\langle \phi_2 \rangle$ in gauche (circles) for segments in a precursor at 400K with draw speed $1 \times 10^9 \text{ s}^{-1}$.

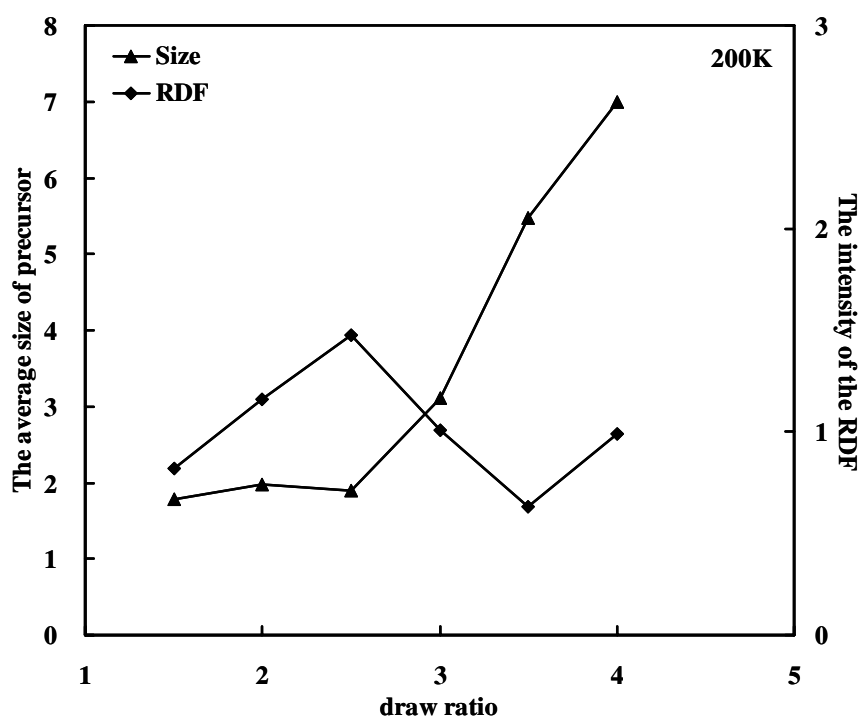


Figure 5.39 The time evolution of RDF intensity (4.11\AA) (diamond) and the time averaged number of parallel segments contained in a representative precursor (triangle) at 200 K with draw speed $1 \times 10^{10} \text{s}^{-1}$.

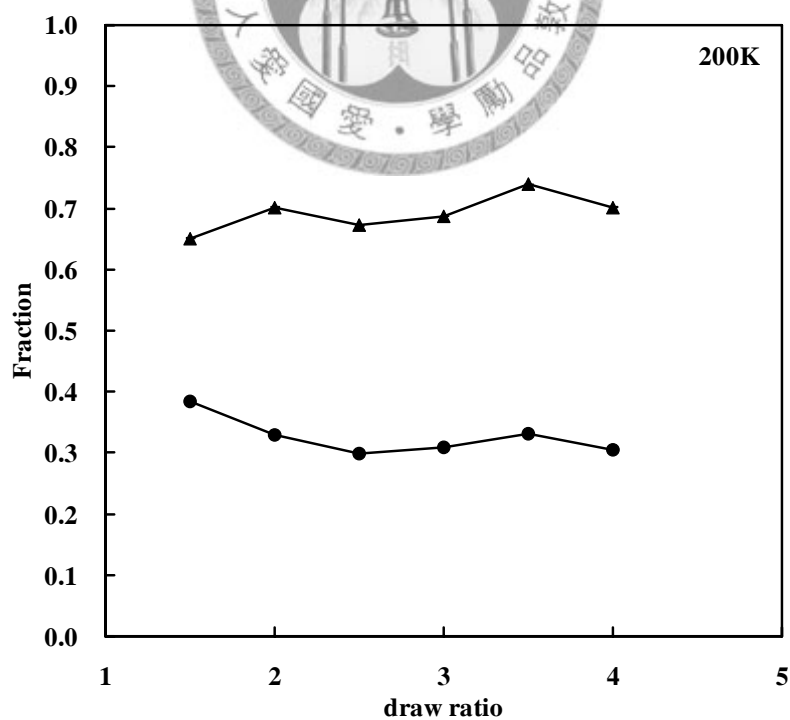


Figure 5.40 The backbone torsions $\langle \phi_1 \rangle$ in trans (triangles) and $\langle \phi_2 \rangle$ in gauche (circles) for segments in a precursor at 200K with draw speed $1 \times 10^{10} \text{s}^{-1}$.

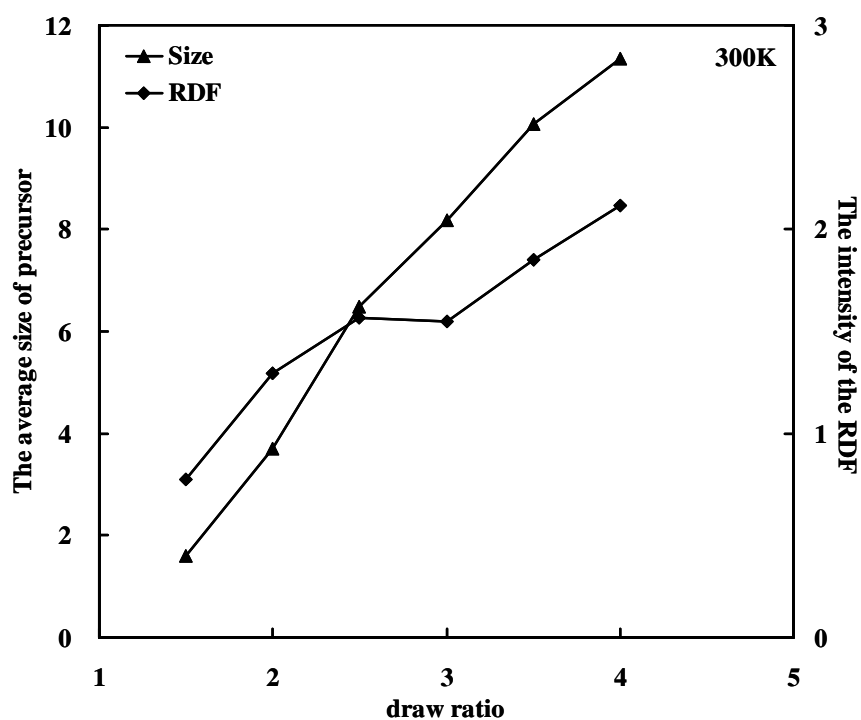


Figure 5.41 The time evolution of RDF intensity (4.11 Å) (diamond) and the time averaged number of parallel segments contained in a representative precursor (triangle) at 300 K with draw speed $1 \times 10^{10} \text{ s}^{-1}$.

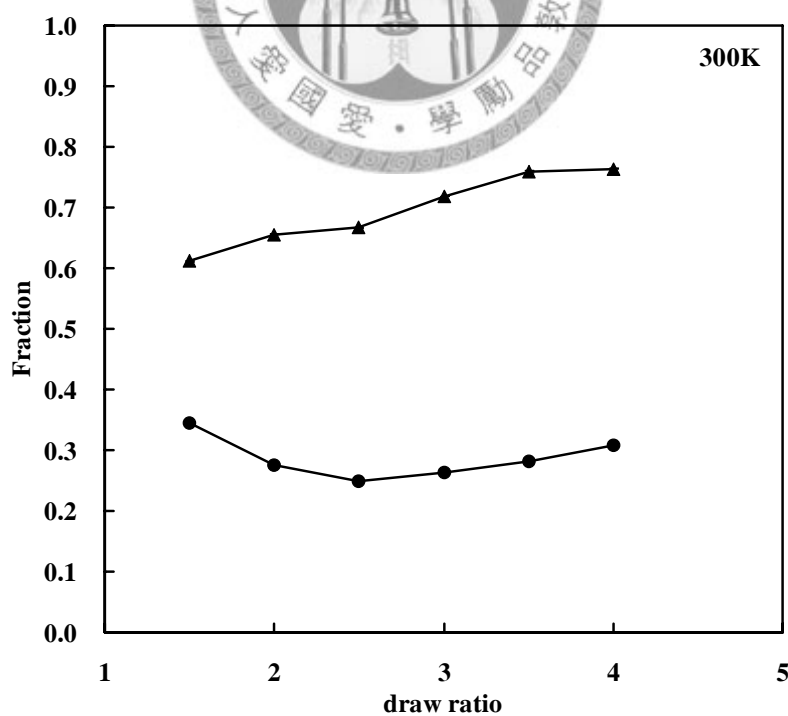


Figure 5.42 The backbone torsions $\langle \phi_1 \rangle$ in trans (triangles) and $\langle \phi_2 \rangle$ in gauche (circles) for segments in a precursor at 300K with draw speed $1 \times 10^{10} \text{ s}^{-1}$.

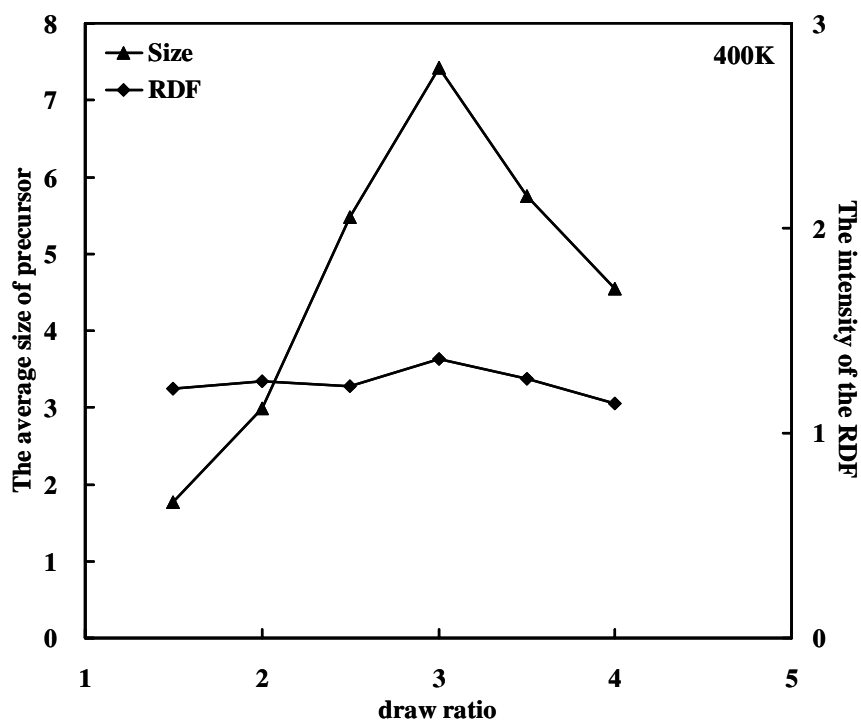


Figure 5.43 The time evolution of RDF intensity (4.11Å) (diamond) and the time averaged number of parallel segments contained in a representative precursor (triangle) at 400 K with draw speed $1 \times 10^{10} \text{s}^{-1}$.

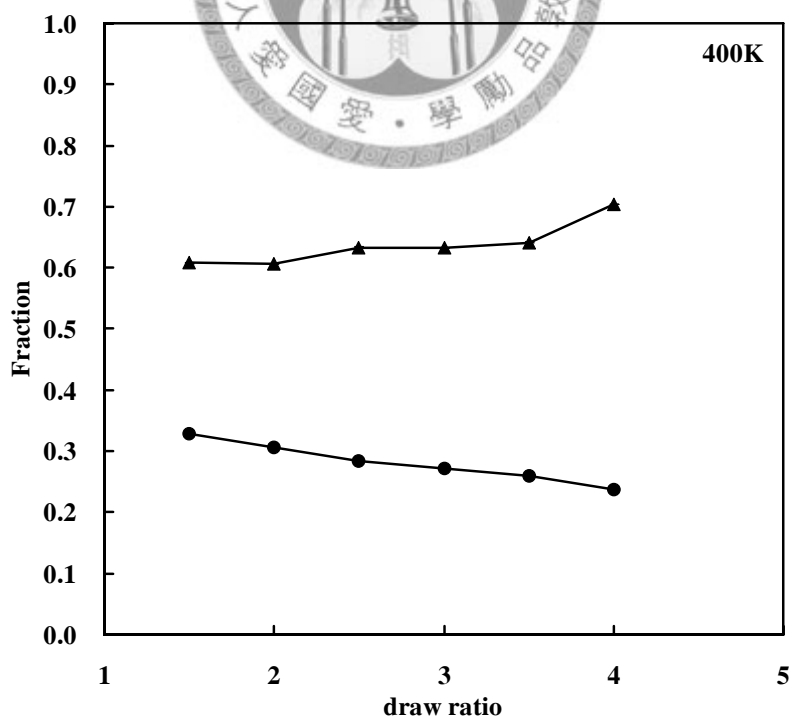


Figure 5.44 The backbone torsions $\langle \phi_1 \rangle$ in trans (triangles) and $\langle \phi_2 \rangle$ in gauche (circles) for segments in a precursor at 400K with draw speed $1 \times 10^{10} \text{s}^{-1}$.

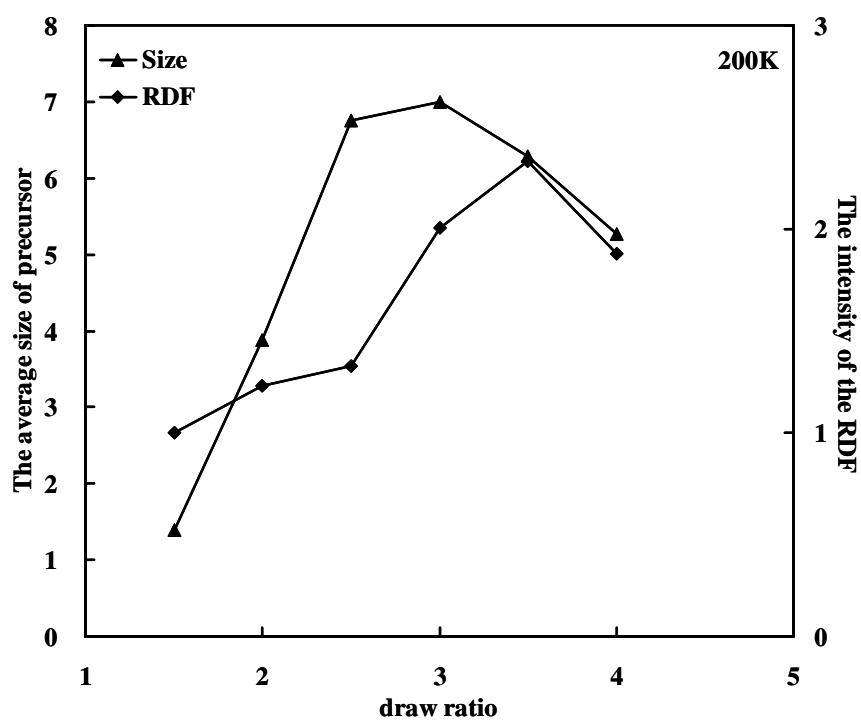


Figure 5.45 The time evolution of RDF intensity (4.11\AA) (diamond) and the time averaged number of parallel segments contained in a representative precursor (triangle) at 200 K with draw speed $1 \times 10^{11} \text{s}^{-1}$.

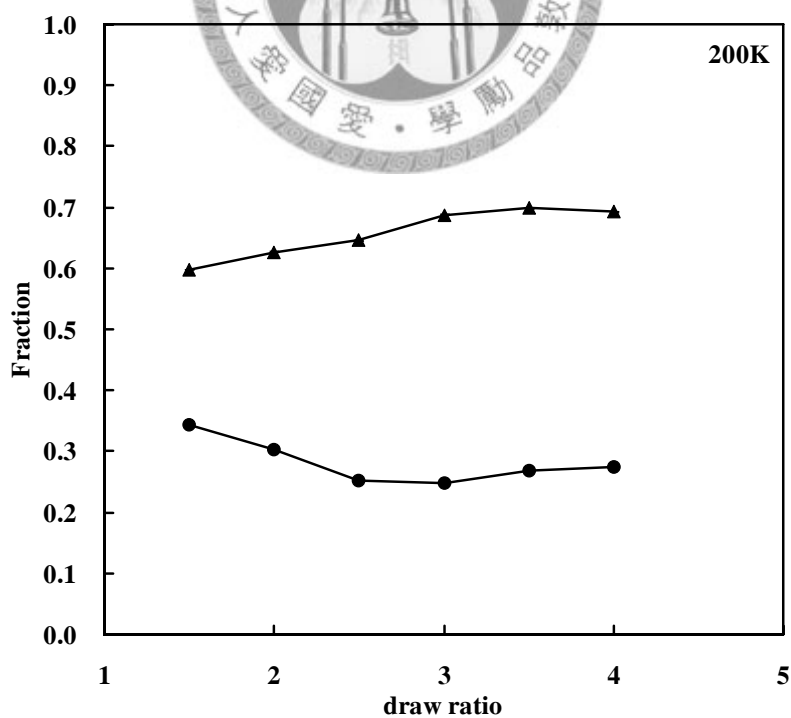


Figure 5.46 The backbone torsions $\langle \phi_1 \rangle$ in trans (triangles) and $\langle \phi_2 \rangle$ in gauche (circles) for segments in a precursor at 200K with draw speed $1 \times 10^{11} \text{s}^{-1}$.

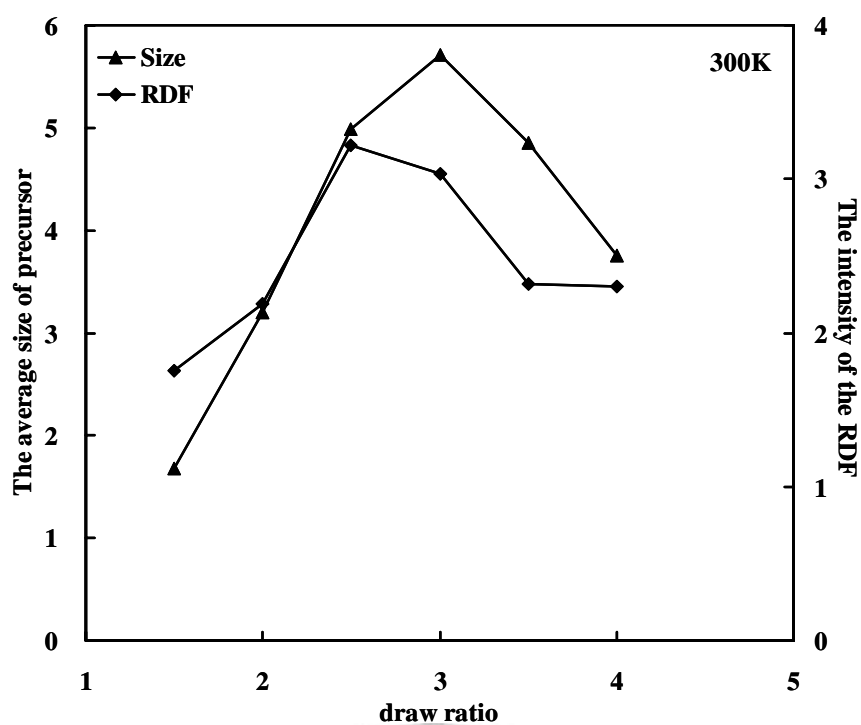


Figure 5.47 The time evolution of RDF intensity (4.11\AA) (diamond) and the time averaged number of parallel segments contained in a representative precursor (triangle) at 300 K with draw speed $1 \times 10^{11} \text{s}^{-1}$.

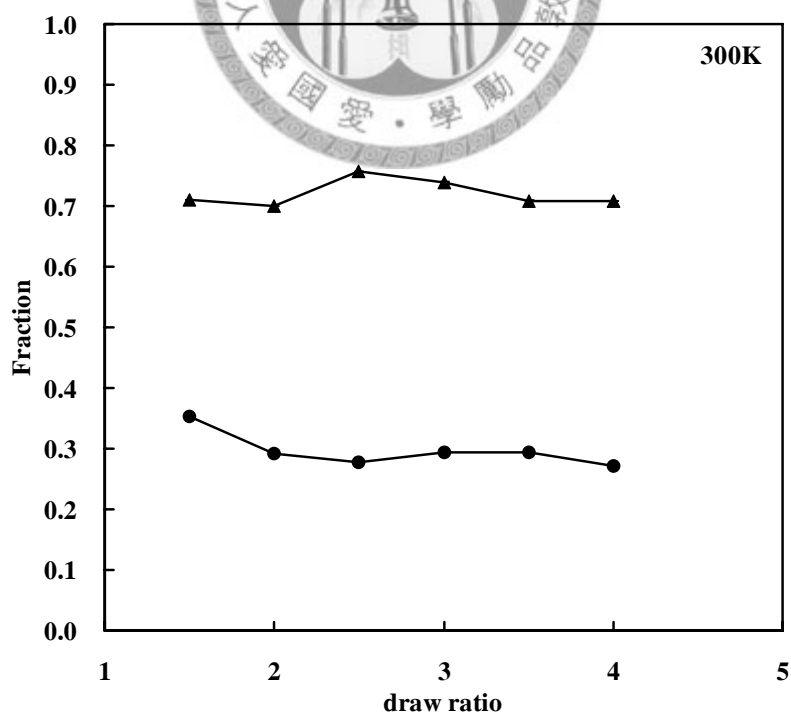


Figure 5.48 The backbone torsions $\langle \phi_1 \rangle$ in trans (triangles) and $\langle \phi_2 \rangle$ in gauche (circles) for segments in a precursor at 300K with draw speed $1 \times 10^{11} \text{s}^{-1}$.

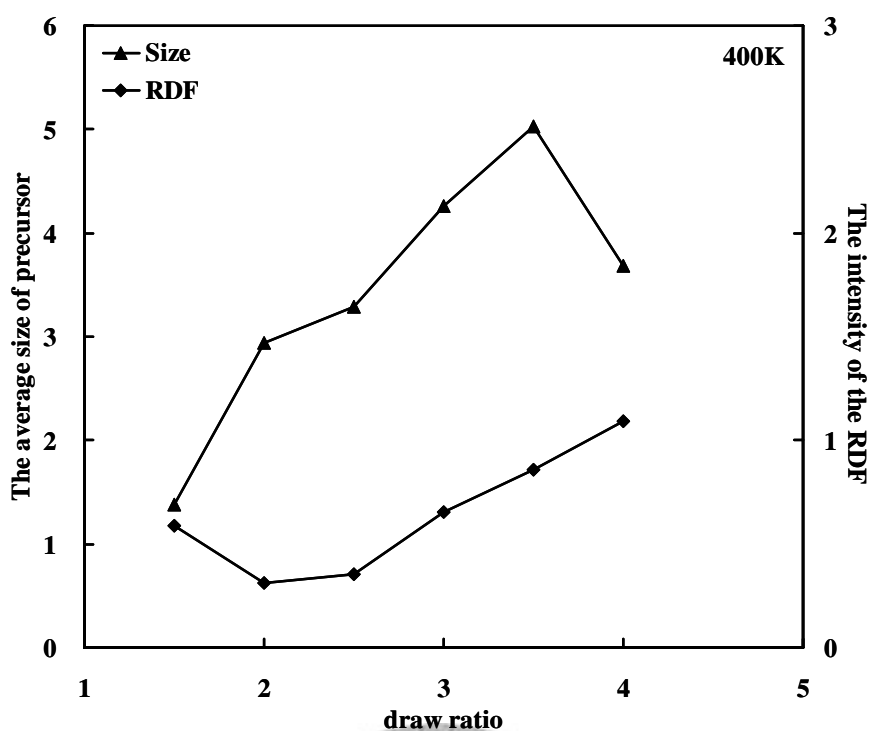


Figure 5.49 The time evolution of RDF intensity (4.11\AA) (diamond) and the time averaged number of parallel segments contained in a representative precursor (triangle) at 400 K with draw speed $1 \times 10^{11} \text{s}^{-1}$.

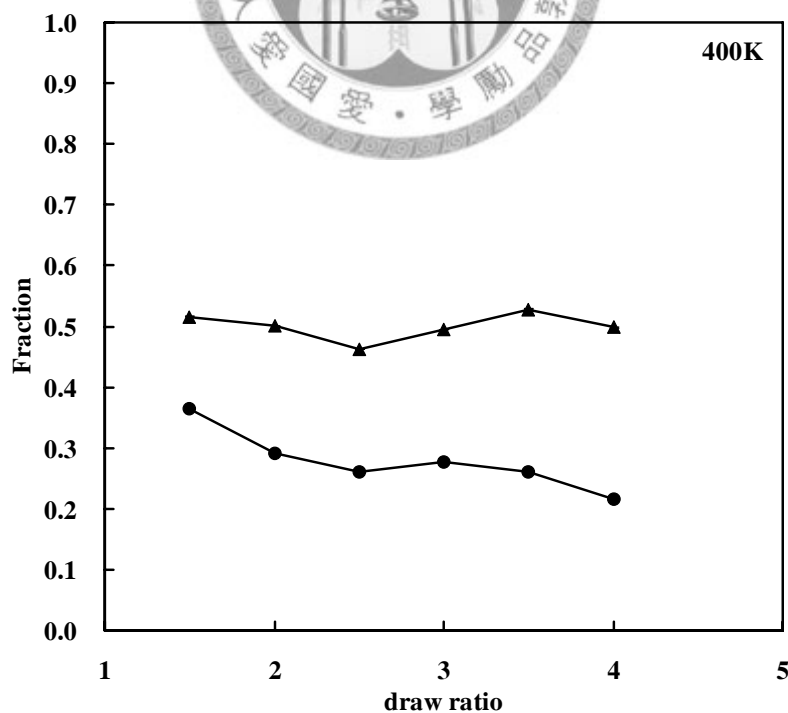


Figure 5.50 The backbone torsions $\langle \phi_1 \rangle$ in trans (triangles) and $\langle \phi_2 \rangle$ in gauche (circles) for segments in a precursor at 400K with draw speed $1 \times 10^{11} \text{s}^{-1}$.

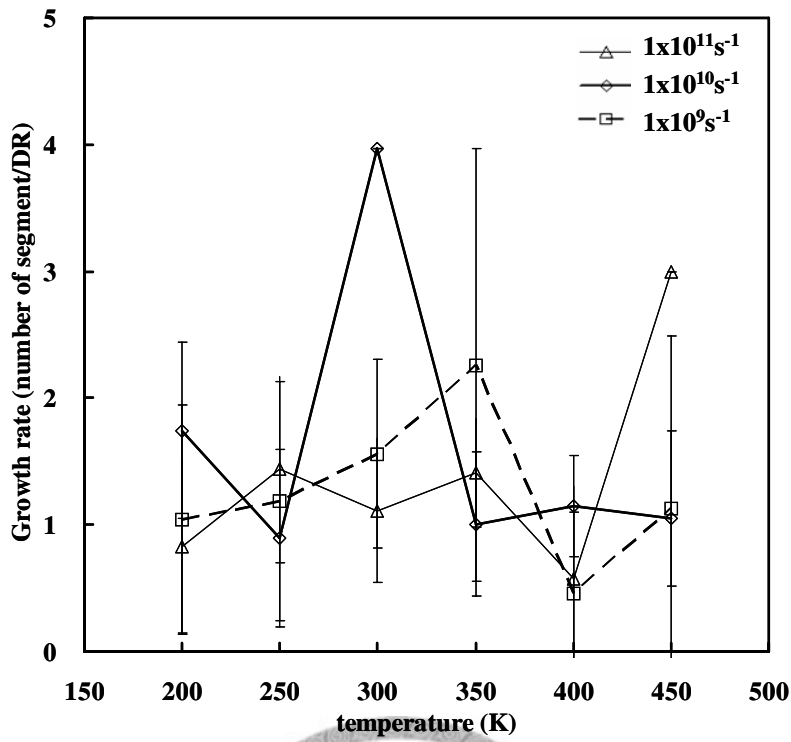


Figure 5.51 The temperature dependence of the growth rate of precursor size with different draw speeds.

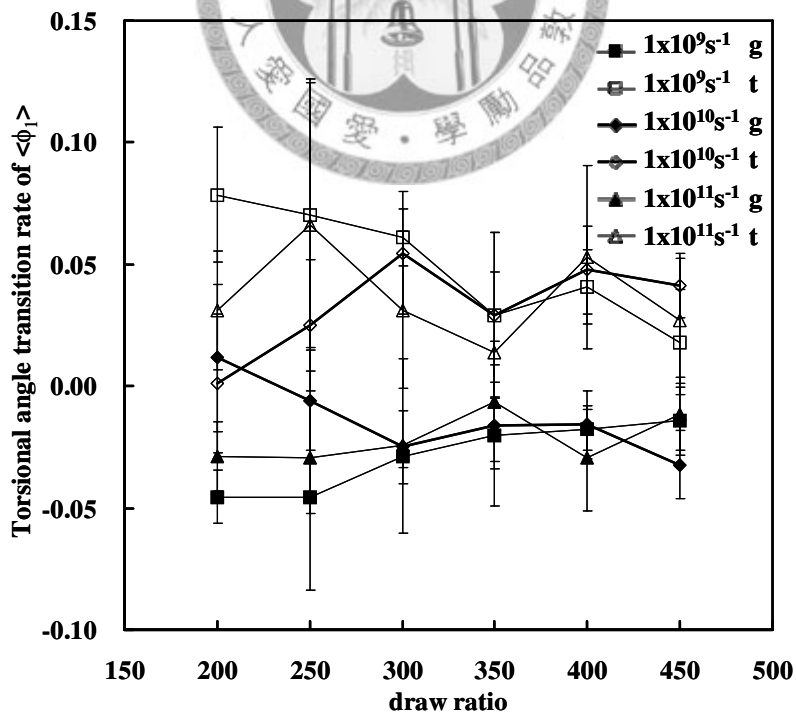


Figure 5.52 The temperature dependence of transition rate of torsional angle ϕ_1 with different draw speeds.

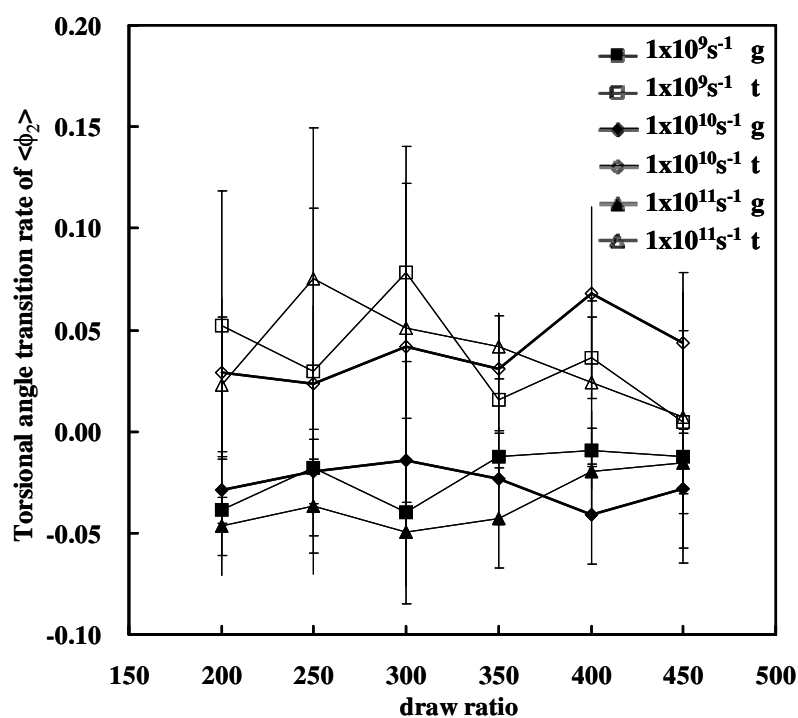


Figure 5.53 The temperature dependence of transition rate of torsional angle ϕ_2 with different draw speeds.



5.3.3 Discussion

In **Table 5.9** it is found that the number of precursors for system under stress is slightly higher than that in the case of isothermal crystallization. In addition, the stress-induced crystallization could create larger precursor in size than isothermal crystallization. Both factors lead to the much higher fraction of precursors in the stress-induced crystallization. The results of the average size of precursor agree with intensity of RDF at 4.11 \AA in each precursor. Most precursors grow with increasing DR until $DR \approx 3.5$ and their intensities of RDF show a similar behavior as DR. This indicates the highly oriented precursors are developing in stress-induced crystallization. Besides, these results suggest that the definition of precursor is adequate for identifying any local structure developed in the polymer systems. From **Figure 5.51**, the maximum

of the growth rate of oriented precursor occurs below the glass transition temperature, suggesting that that local motion of polymer segments would be induced by uni-axis stresses. The maximum growth rate appears at draw speed $1 \times 10^{10} \text{s}^{-1}$ and temperature region between 250K and 350K, implying the better condition of stress-induced crystallization are not the faster.

The states of backbone torsional angles in precursors evolve with DR differently in different processing conditions. The fraction of ϕ_1 in trans increases with DR, but the fraction of ϕ_2 in gauche decreases with DR in most precursors. The stress and thermal effects are different in these two torsional angles. Slower draw speed and lower temperature would improve the change of ϕ_1 to the trans state; on the other hand, the faster draw speed and medium temperatures would improve the change of ϕ_2 to the gauche state. Furthermore, the fraction of ϕ_1 in trans is very high (~70%) in each precursor, but the fraction of ϕ_2 in gauche only 20~30%. That indicates that the stress-induced transition in ϕ_2 is faster than that in ϕ_1 . In addition, the fraction of ϕ_2 in gauche fluctuates in some cases, indicating the torsional angle ϕ_2 would favorably move to the gauche after forcing to the trans state by the external stress.

6 Conclusion

We have successfully predicted the several physical properties (parameters of crystal structure, torsional angles in crystal structure, glass transition temperature, melting temperature, and Young's modulus) of the PTT polymer using modified Dreding force field. The formation of nuclei precursors in the induction period of isothermal crystallization of polymer from melt is observed in our simulation. Between T_g and T_m , the torsional and van der Waals forces drive the segments to form precursors consisting of parallel segments. The amount of precursors increases rapidly soon after the system is cooled and then fluctuates around some asymptotic value. During this later stage, it is found that the torsional distribution of the polymer backbone for segments within the precursor slowly rearranges to that in the crystalline state. In addition, the temperature variation of the amount of precursor resembles that of the crystallization rate between T_g and T_m . It is likely that the precursors will eventually evolve to compact nuclei for subsequent crystallization processes.

Based on the simulation results, we propose that nuclear precursors are formed in the induction period, prior to the appearance of nuclei during the crystallization process. The precursor has a high internal orientation order but is loosely packed. The precursors are constantly forming, growing, and disintegrating. The formation of precursors is mainly driven by van der Waals and torsional forces. These two forces may either collaborate or compete, resulting in the segment to reorganization to form a more compact cluster. Therefore, the precursors could eventually become compact nuclei for the subsequent crystallization process. However, the precursor internal structure development (e.g. torsional reorganization) takes place at a much slower rate (compared

to the formation of precursors), even the rearrangement of the torsional angle ϕ_2 would accelerate by stress. As a consequence, there observed (experimentally) a long induction period prior to the crystallization of polymers.

The formation of oriented precursor in the stress-induced crystallization is also observed in our simulation. The torsional and van der Waals forces are the dominant interactions, similar to the case observed in isothermal crystallization. The amount of stress-induced precursor increases in all regions of temperature. The maximum size of oriented precursor is larger than that created only by thermal stimulation. During stress-induced crystallization, the torsional distribution of the polymer backbone for segments rapidly rearrange to the t-t-t conformation in bulk phase. Within oriented precursors, the response of the torsional angle induced by stress is faster than that only induced by thermal stimulation, especially trans in ϕ_1 (the transition rate of trans state in ϕ_1 is faster than that of gauche state in ϕ_2).

In our simulation, the structures of precursor packing by polymer segments are observed in isothermal and stress-induced crystallization such as many simulation works, which use coarse-grained or bead-spring models. Furthermore, the atomic model supports us to understand more detailed development (such as torsional angle) and to approach the atomic mechanism of the polymer crystallization at very early state.

Appendix A

In this section, we show the value of parameters used in Dreiding force field. In our system, there are three kinds of atom (carbon, oxygen, and hydrogen) defined as different atomic force field types in **Table A.1** (according the atomic position shown as **Figure A.1**). Then, one can identify eight kinds of bond types (shown in **Table A.2**), three groups, overall 13 kinds) of angle types, 4 groups (overall 16 kinds) of torsion types, and inversion.



Figure A.1 The atomic position on the PTT polymer repeat unit.

Table A.1 The definition of each atom type in atomic model.

Atomic position	Atomic force field type
C1, C in ring	C_R
O2	O_R
C3,C4	C_3
O5	O_2
H, H end	H

Table A.2 The value of parameters of band energy in our simulation.

Type	$1/2K_b$ (Kcal/mole/Å ²)	R_0 (Å)
C_R, C_R	525	1.39
C_3, C_3	350	1.53
C_3, O_R	350	1.42
C_R, O_R	525	1.35
C_R, O_2	700	1.25
C_3, H_	350	1.09
C_R, H_	350	1.02
O_R, H	350	0.98

Table A.3 The value of parameters of angle energy in our simulation.

Type	$1/2K_\theta$ (Kcal/mole)	θ_0 (deg.)
X, C_R, X		
C_R, C_R, C_R	100	120
C_R, C_R, O_2	100	120
C_R, C_R, O_R	100	120
C_R, C_R, H_	100	120
O_2, C_R, H_(end)	100	120
O_R, C_R, O_2	100	120
X, C_3, X		
C_3, C_3, C_3	100	109.471
C_3, C_3, O_R	100	109.471
C_3, C_3, H_	100	109.471
O_R, C_3, H_	100	109.471
H_, C_3, H_	100	109.471
X, O_R, X		
C_R, O_R, C_3	100	120
C_3, O_R, H_	100	104.51

Table A.4 The value of parameters of torsion energy in our simulation.

Type	$1/2K_{\phi}$ (Kcal/mole)	n	d
X, C_R, C_R, X			
C_R, C_R, C_R, H_	25	1	2
C_R, C_R, C_R, C_R	25	1	2
H_, C_R, C_R, H_	25	1	2
C_R, C_R, C_R, O_2	10	1	2
C_R, C_R, C_R, O_R	10	1	2
C_R, C_R, C_R, H_ (end)	10	1	2
X, C_3, C_3, X			
H_, C_3, C_3, O_R	2	-1	3
O_R, C_3, C_3, C_3	2	-1	3
H_, C_3, C_3, H_	2	-1	3
H_, C_3, C_3, C_3	2	-1	3
X, C_R, O_R, X			
C_R, C_R, O_R, C_3	25	1	2
O_2, C_R, O_R, C_3	25	1	2
X, C_3, O_R, X			
C_3, C_3, O_R, C_R	2	-1	3
C_3, C_3, O_R, H_	2	-1	3
H_, C_3, O_R, H_	2	-1	3
H_, C_3, O_R, C_R	2	-1	3

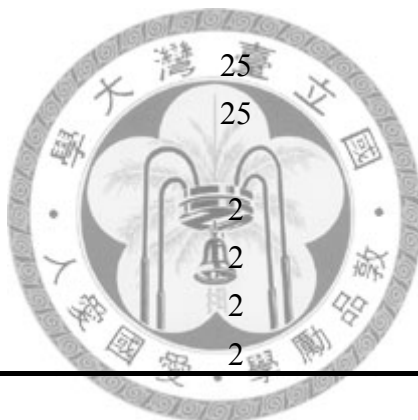


Table A.5 The value of parameters of inversion energy in our simulation.

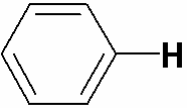
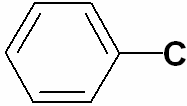
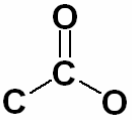
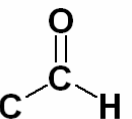
Type	$1/2K_{\psi}$ (Kcal/mole)	ψ_0
	40	0
	40	0
	40	0
	40	0

Table A.5 The value of parameters of Van der Waals interaction in our simulation.

Type	D_0	R_0	ζ
C_R	0.0951	3.8983	14.034
C_3	0.0951	3.8983	14.034
O_R	0.0957	3.4046	13.483
O_2	0.0957	3.4046	13.483
H_	0.0152	3.195	12.382
H (end)	0.0001	3.195	12.000

The cross-type coefficients of non-bond interaction are computed using the mixing rule:

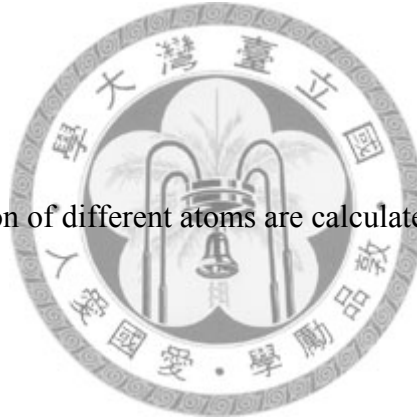
$$A_{ij} = \sqrt{A_{ii} \times A_{jj}} \quad (\text{A.1a})$$

$$B_{ij} = \sqrt{B_{ii} \times B_{jj}} \quad (\text{A.1b})$$

$$C_{ij} = \frac{C_{ii} + C_{jj}}{2} \quad (\text{A.1c})$$

and the non-bond interaction of different atoms are calculated as follow:

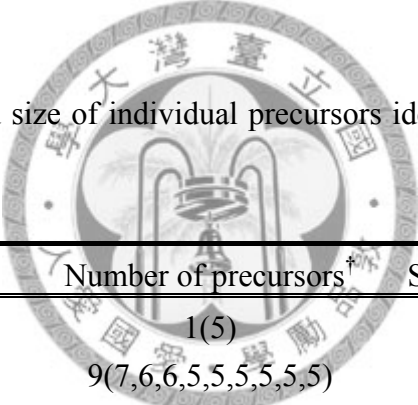
$$U_{ij} = A_{ij}e^{-C_{ij}r} - B_{ij}r^{-6} \quad (\text{A.2})$$



Appendix B

In Appendix B, we show the precursors which are detected in the double size system (eight chains in the amorphous state) during isothermal crystallization process. The number and size of individual precursors are shown in **Table B.1**. The intensity of the RDF, average size (**Figure B.1, B.3 and B.5**) and distribution of torsional angle (**Figure B.2, B.4, and B.6**) within the maximum size of precursor are shown at 350K, 400K, and 450K, respectively.

Table B.1 The number and size of individual precursors identified in MD simulations.
(27x8)



Temperature (K)	Number of precursors [†]	Simulation length (ns)
350	1(5)	12
400	9(7,6,6,5,5,5,5,5,5)	12
450	8(6,5,5,5,5,5,5,5)	12

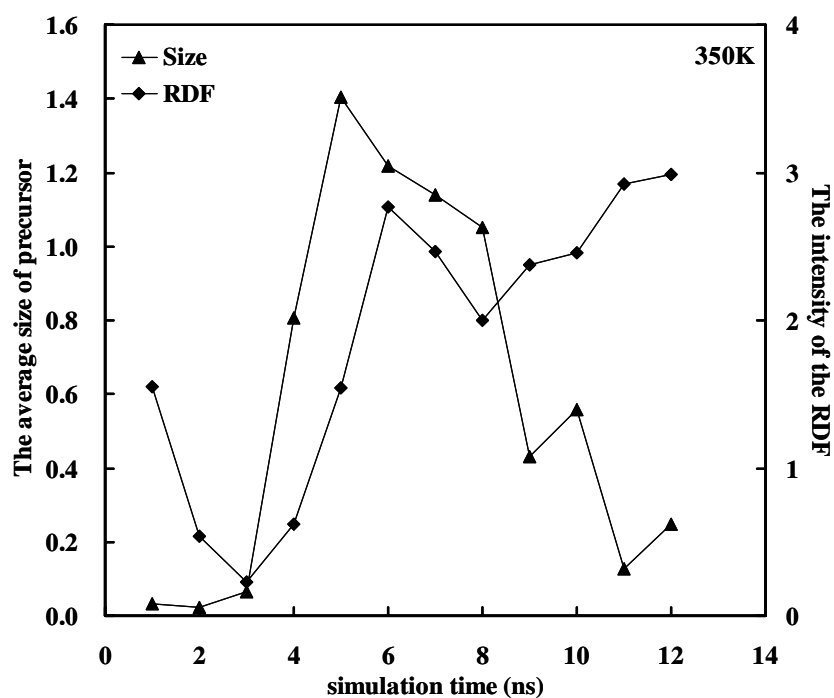


Figure B.1 The time evolution of RDF intensity (4.11Å) (diamond) and the time averaged number of parallel segments contained in a representative precursor (triangle) at 350 K. (27x8)

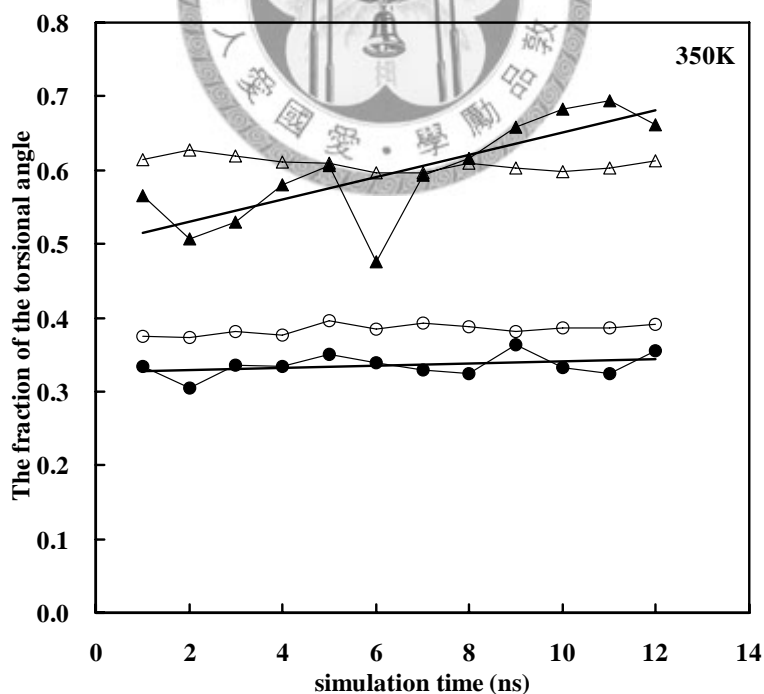


Figure B.2 the backbone torsions $\langle\phi_1\rangle$ in trans (triangles) and $\langle\phi_2\rangle$ in gauche (circles) for segments in a precursor (closed symbols) and outside any precursor (open symbols) at 350 K. (27x8)

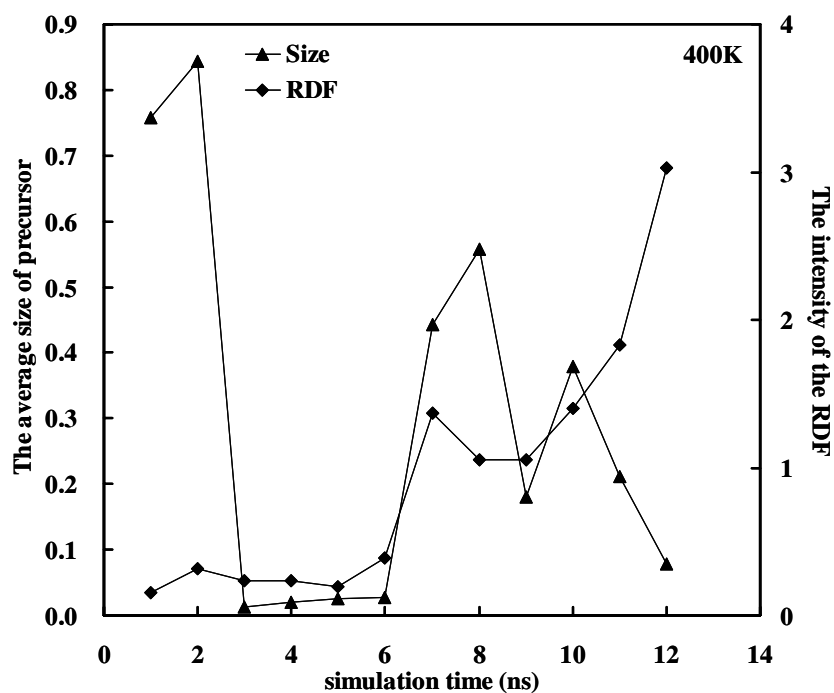


Figure B.3 The time evolution of RDF intensity (4.11Å) (diamond) and the time averaged number of parallel segments contained in a representative precursor (triangle) at 400 K. (27x8)

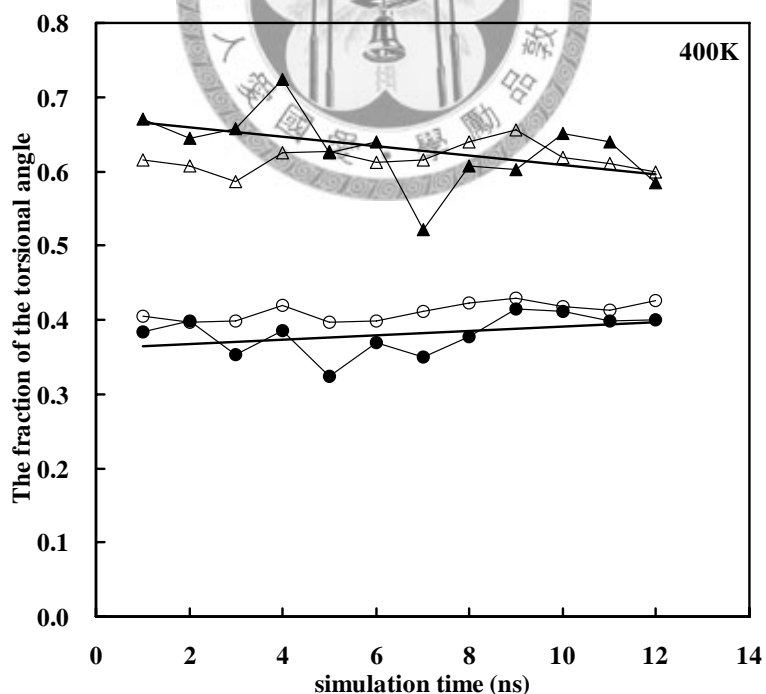


Figure B.4 the backbone torsions $\langle\phi_1\rangle$ in trans (triangles) and $\langle\phi_2\rangle$ in gauche (circles) for segments in a precursor (closed symbols) and outside any precursor (open symbols) at 350 K. (27x8)

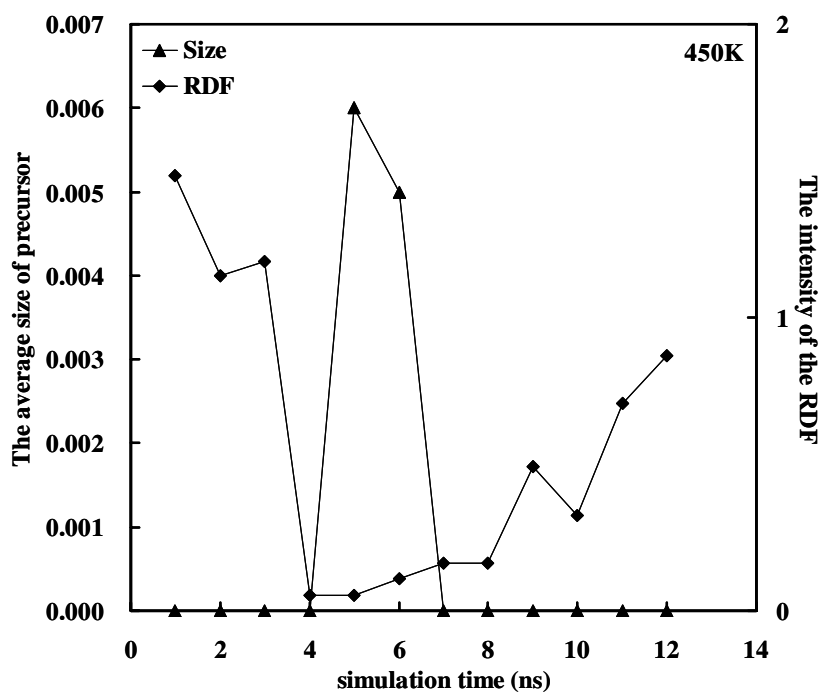


Figure B.5 The time evolution of RDF intensity (4.11Å) (diamond) and the time averaged number of parallel segments contained in a representative precursor (triangle) at 450 K. (27x8)

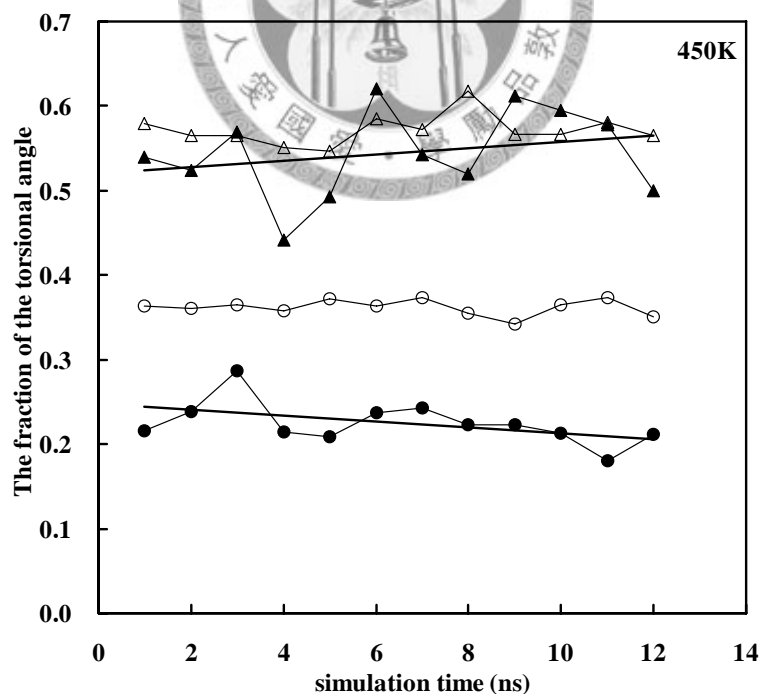


Figure B.6 the backbone torsions $\langle\phi_1\rangle$ in trans (triangles) and $\langle\phi_2\rangle$ in gauche (circles) for segments in a precursor (closed symbols) and outside any precursor (open symbols) at 350 K. (27x8)

Appendix C

In appendix C, we show the results of precursor formation in the system contenting 14 chains, each chain having 27 repeat units, during stress-induced crystallization. The number and size of individual precursors are shown in **Table C.1**, **C.2**, and **C.3** with draw speed $1 \times 10^{10} \text{s}^{-1}$, $5 \times 10^{10} \text{s}^{-1}$, and $1 \times 10^{11} \text{s}^{-1}$, respectively. **Figures C.1**, **C.3**, and **C.5** show the time evolution of RDF intensity at 4.11Å , and the average size of precursor at 200K, 300K, and 400K, respectively, with a draw speed of $1 \times 10^{10} \text{s}^{-1}$; **Figures C.7**, **C.9**, and **C.11** show the results for draw speed $5 \times 10^{10} \text{s}^{-1}$; **Figures C.13**, **C.15**, and **C.17** for draw speed $1 \times 10^{11} \text{s}^{-1}$. On the other hand, **Figures C.2**, **C.4**, and **C.6** show the results of the fractions of backbone torsions in the oriented precursors at 200K, 300K, and 400K, respectively, with a draw speed $1 \times 10^{10} \text{s}^{-1}$; **Figures C.8**, **C.10**, and **C.12** show the results for draw speed $5 \times 10^{10} \text{s}^{-1}$; **Figures C.14**, **C.16**, and **C.18** for draw speed $1 \times 10^{11} \text{s}^{-1}$.

Table C.1 The number and size of individual precursors identified in stress-induced crystallization with draw speed $1 \times 10^{10} \text{s}^{-1}$. (27x14)

Temperature (K)	Number of precursor	Strains (%)
200	10(42,16,14,9,7,7,6,6,5,5)	300
250	13(24,17,10,9,8,8,7,7,6,6,6,5,5)	300
300	17(20,17,14,13,10,9,7,7,6,6,6,6,5,5,5,5,5)	300
350	15(24,23,18,9,8,8,7,6,6,6,6,5,5,5,5)	300
400	15(33,13,11,9,9,7,6,6,5,5,5,5,5,5,5)	300
450	14(29,24,15,13,12,10,8,7,6,6,6,6,5,5)	300

Table C.2 The number and size of individual precursors identified in stress-induced crystallization with draw speed $5 \times 10^{10} \text{s}^{-1}$. (27x14)

Temperature (K)	Number of precursor	Strains (%)
200	13(25,12,10,8,7,7,7,6,5,5,5,5)	300
250	14(28,15,9,7,7,6,6,6,5,5,5,5,5,5).	300
300	7(35,23,8,8,6,6,5)	300
350	14(27,13,10,10,7,7,6,6,6,6,6,5,5,5)	300
400	12(32,11,11,10,10,8,8,7,6,5,5,5)	300
450	12(27,12,9,8,8,8,7,6,5,5,5)	300



Table C.3 The number and size of individual precursors identified in stress-induced crystallization with draw speed $1 \times 10^{11} \text{s}^{-1}$. (27x14)

Temperature (K)	Number of precursor	Strains (%)
200	12(28,8,7,7,6,6,5,5,5,5,5,5)	300
250	14(18,10,8,8,7,7,6,6,5,5,5,5,5,5)	300
300	8(31,12,12,11,10,7,5,5)	300
350	11(35,16,10,10,9,8,8,6,6,5,5)	300
400	12(27,12,10,6,6,6,6,6,5,5,5,5)	300
450	8(21,19,13,12,11,5,5,5)	300

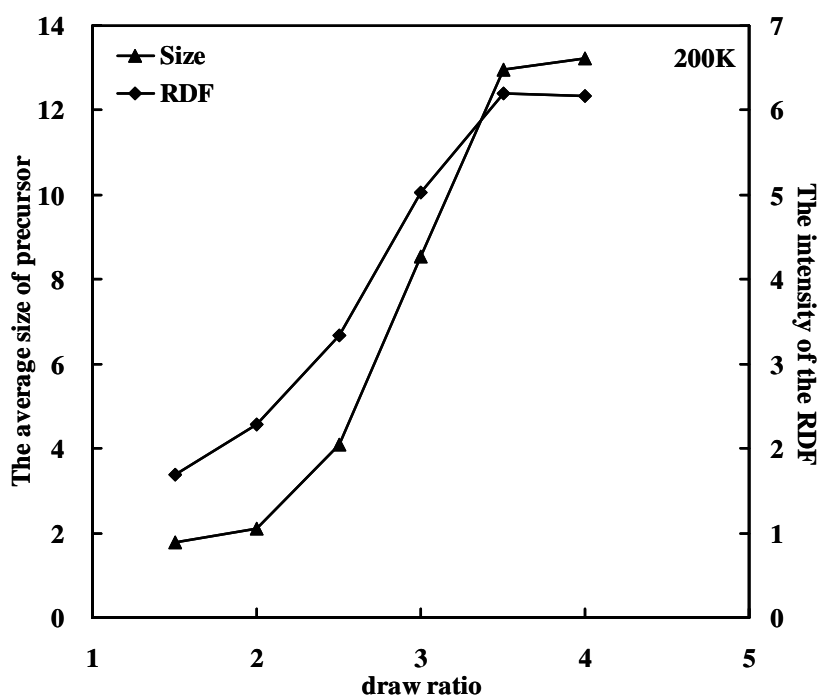


Figure C.1 The time evolution of RDF intensity (4.11Å) (diamond) and the time averaged number of parallel segments contained in a representative precursor (triangle) at 200 K with draw speed $1 \times 10^{10} \text{ s}^{-1}$. (27x14)

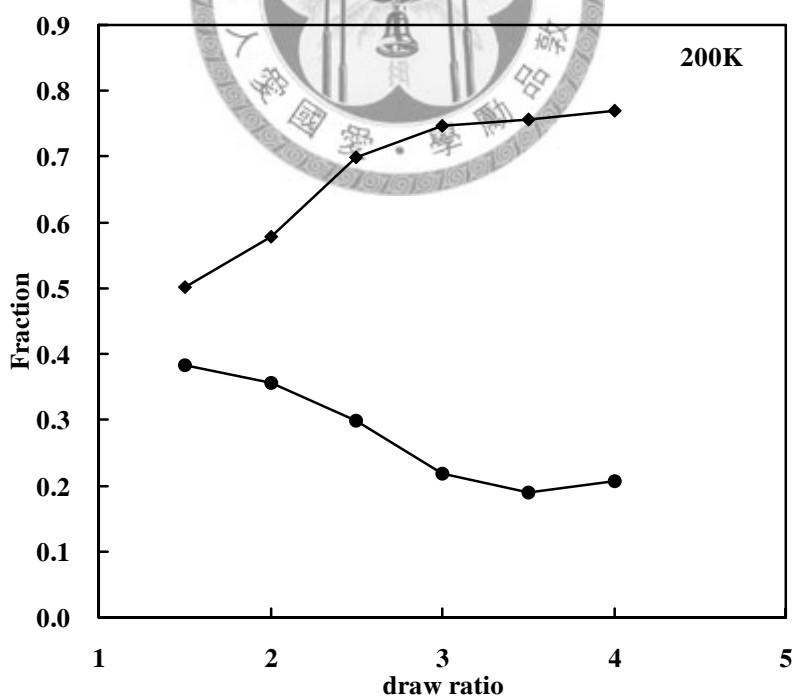


Figure C.2 the backbone torsions $\langle \phi_1 \rangle$ in trans (triangles) and $\langle \phi_2 \rangle$ in gauche (circles) for segments in a precursor (closed symbols) and outside any precursor (open symbols) at 200 K with draw speed $1 \times 10^{10} \text{ s}^{-1}$. (27x14)

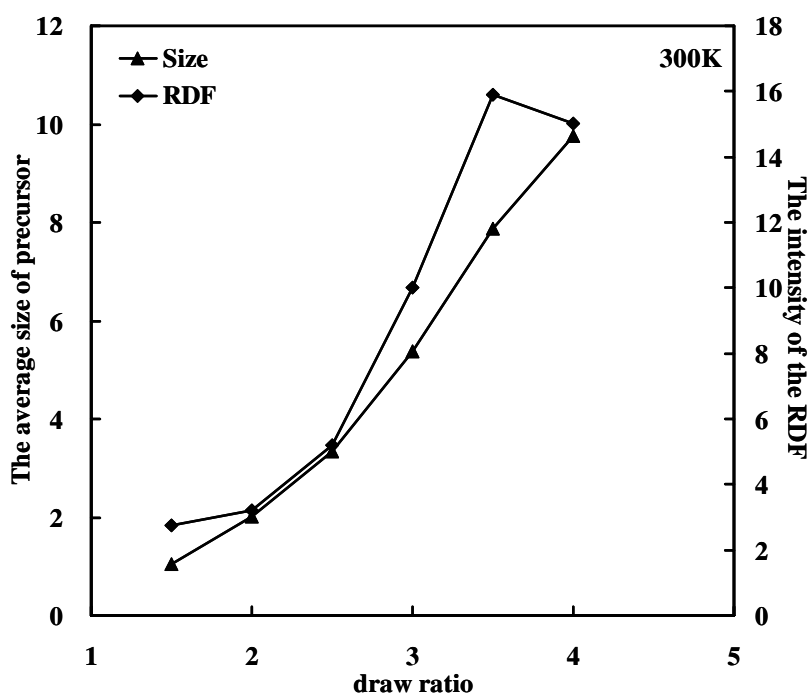


Figure C.3 The time evolution of RDF intensity (4.11Å) (diamond) and the time averaged number of parallel segments contained in a representative precursor (triangle) at 300 K with draw speed $1 \times 10^{10} \text{ s}^{-1}$. (27x14)

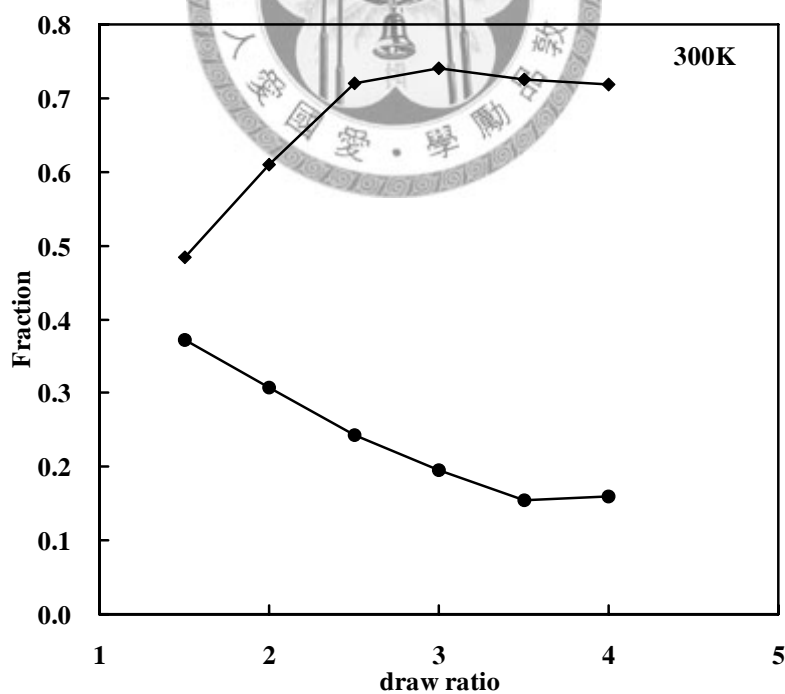


Figure C.4 the backbone torsions $\langle \phi_1 \rangle$ in trans (triangles) and $\langle \phi_2 \rangle$ in gauche (circles) for segments in a precursor (closed symbols) and outside any precursor (open symbols) at 300 K with draw speed $1 \times 10^{10} \text{ s}^{-1}$. (27x14)

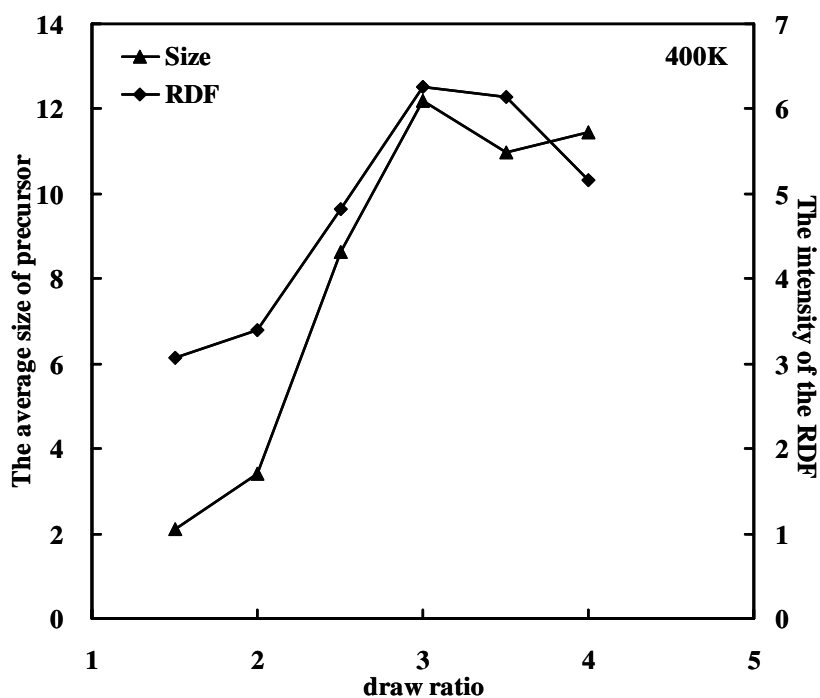


Figure C.5 The time evolution of RDF intensity (4.11Å) (diamond) and the time averaged number of parallel segments contained in a representative precursor (triangle) at 400 K with draw speed $1 \times 10^{10} \text{ s}^{-1}$. (27x14)

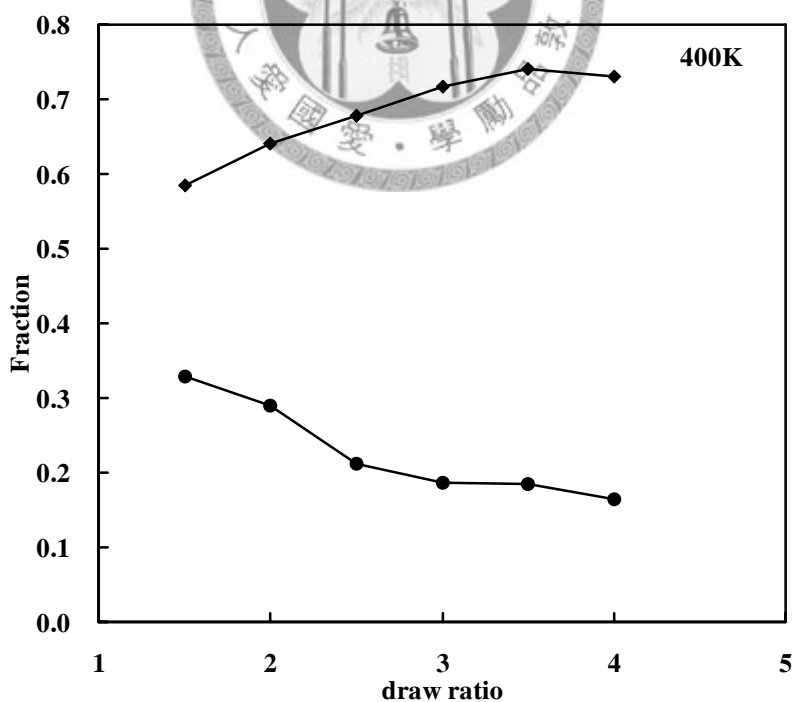


Figure C.6 the backbone torsions $\langle \phi_1 \rangle$ in trans (triangles) and $\langle \phi_2 \rangle$ in gauche (circles) for segments in a precursor (closed symbols) and outside any precursor (open symbols) at 400 K with draw speed $1 \times 10^{10} \text{ s}^{-1}$. (27x14)

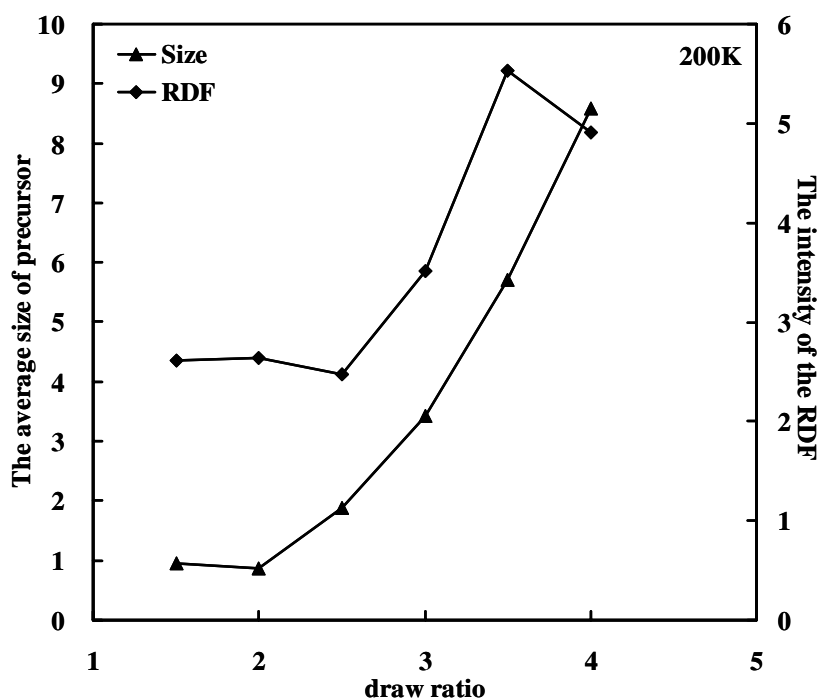


Figure C.7 The time evolution of RDF intensity (4.11\AA) (diamond) and the time averaged number of parallel segments contained in a representative precursor (triangle) at 200 K with draw speed $5 \times 10^{10} \text{ s}^{-1}$. (27x14)

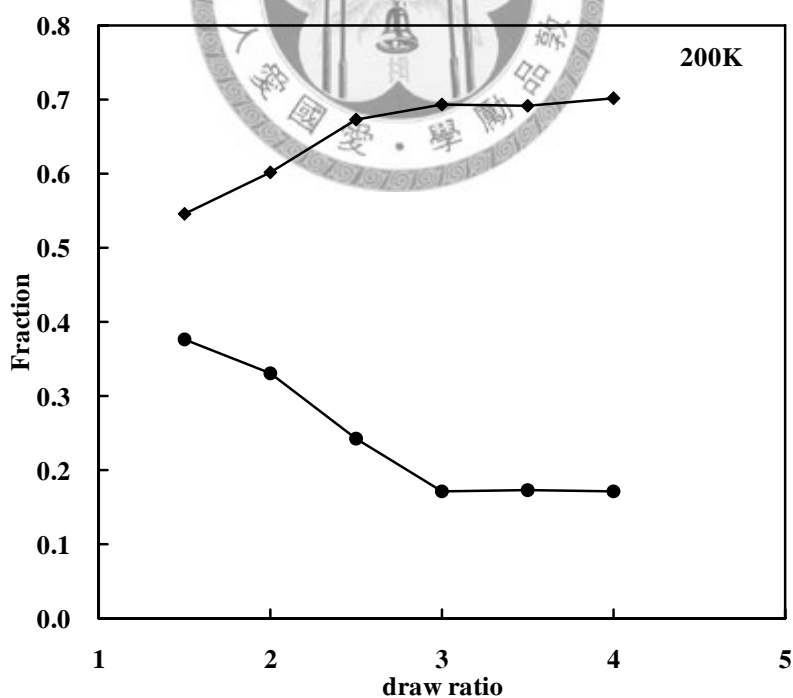


Figure C.8 the backbone torsions $\langle \phi_1 \rangle$ in trans (triangles) and $\langle \phi_2 \rangle$ in gauche (circles) for segments in a precursor (closed symbols) and outside any precursor (open symbols) at 200 K with draw speed $5 \times 10^{10} \text{ s}^{-1}$. (27x14)

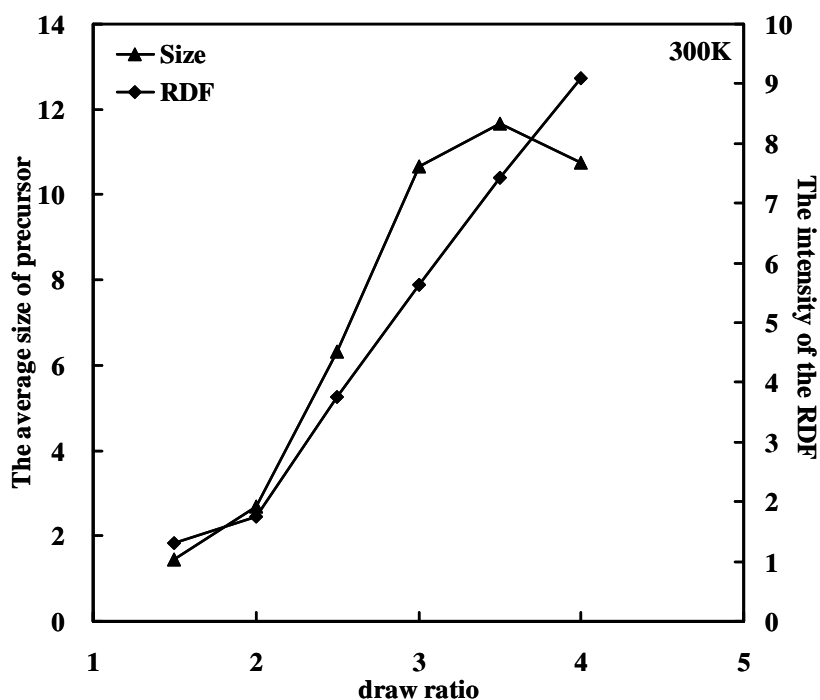


Figure C.9 The time evolution of RDF intensity (4.11Å) (diamond) and the time averaged number of parallel segments contained in a representative precursor (triangle) at 300 K with draw speed $5 \times 10^{10} \text{ s}^{-1}$. (27x14)

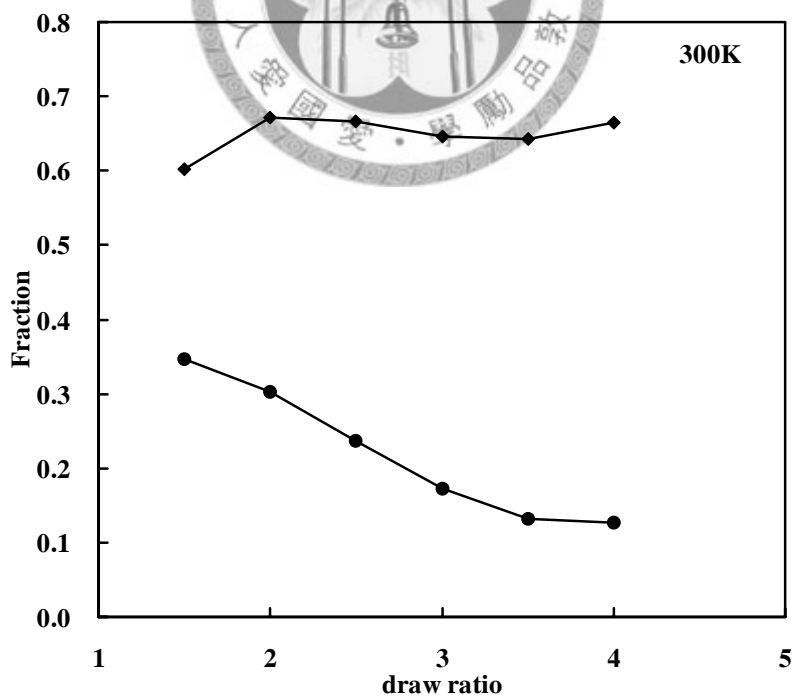


Figure C.10 the backbone torsions $\langle \phi_1 \rangle$ in trans (triangles) and $\langle \phi_2 \rangle$ in gauche (circles) for segments in a precursor (closed symbols) and outside any precursor (open symbols) at 300 K with draw speed $5 \times 10^{10} \text{ s}^{-1}$. (27x14)

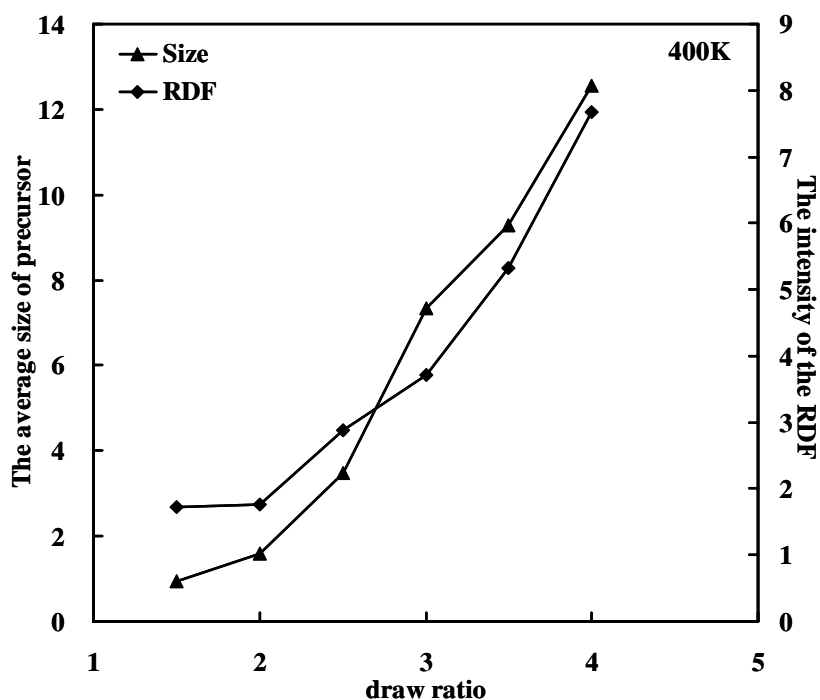


Figure C.11 The time evolution of RDF intensity (4.11\AA) (diamond) and the time averaged number of parallel segments contained in a representative precursor (triangle) at 400 K with draw speed $5 \times 10^{10} \text{ s}^{-1}$. (27x14)

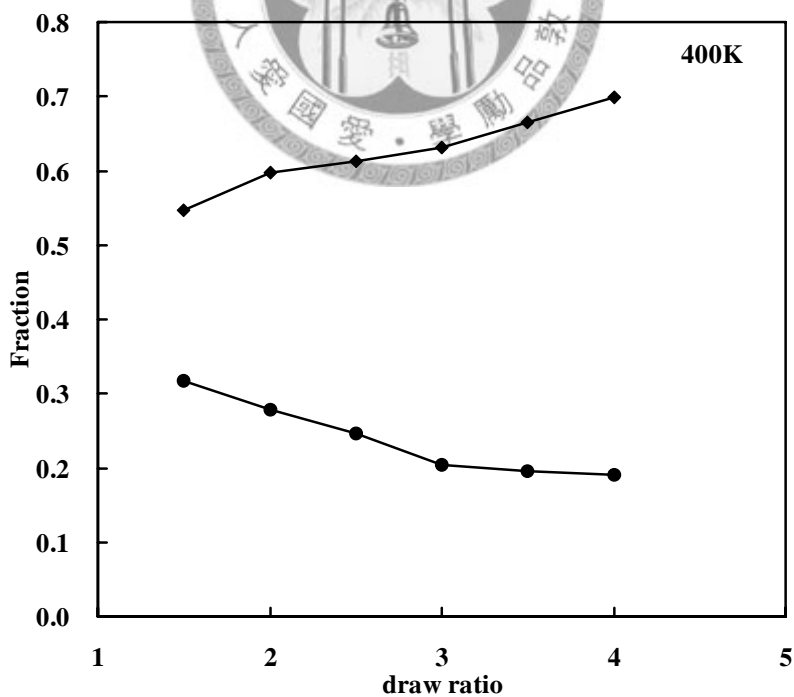


Figure C.12 the backbone torsions $\langle \phi_1 \rangle$ in trans (triangles) and $\langle \phi_2 \rangle$ in gauche (circles) for segments in a precursor (closed symbols) and outside any precursor (open symbols) at 400 K with draw speed $5 \times 10^{10} \text{ s}^{-1}$. (27x14)

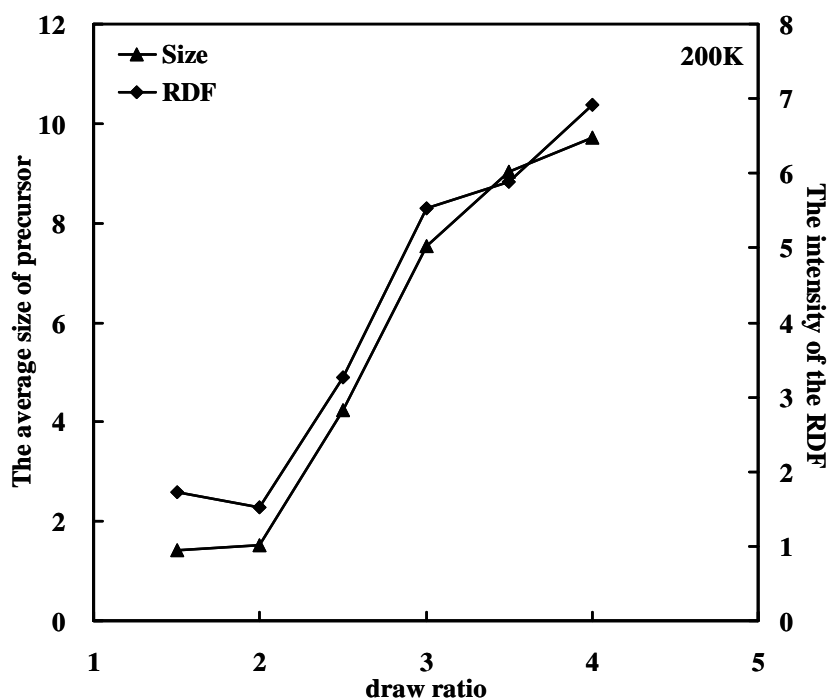


Figure C.13 The time evolution of RDF intensity (4.11Å) (diamond) and the time averaged number of parallel segments contained in a representative precursor (triangle) at 200 K with draw speed $1 \times 10^{11} \text{ s}^{-1}$. (27x14)

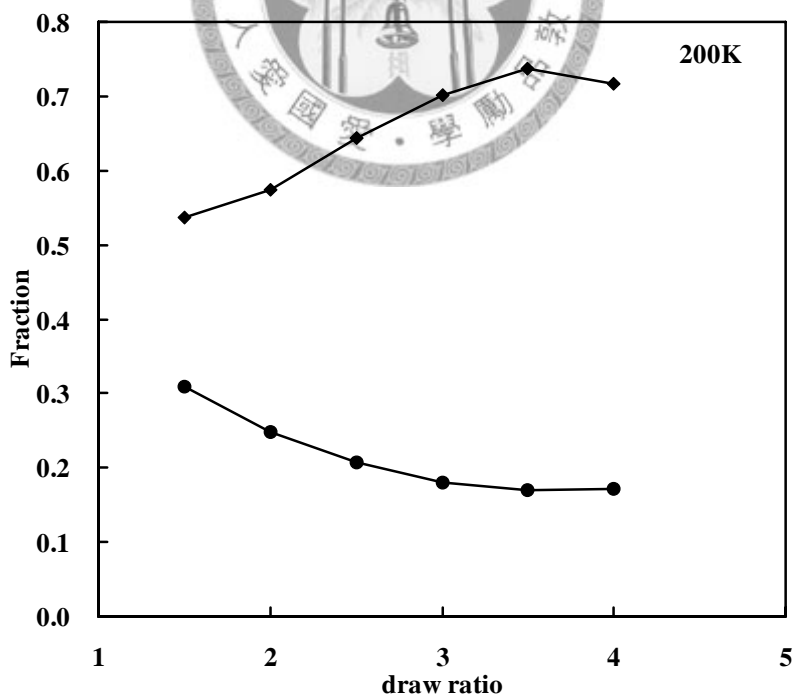


Figure C.14 the backbone torsions $\langle \phi_1 \rangle$ in trans (triangles) and $\langle \phi_2 \rangle$ in gauche (circles) for segments in a precursor (closed symbols) and outside any precursor (open symbols) at 200 K with draw speed $1 \times 10^{11} \text{ s}^{-1}$. (27x14)

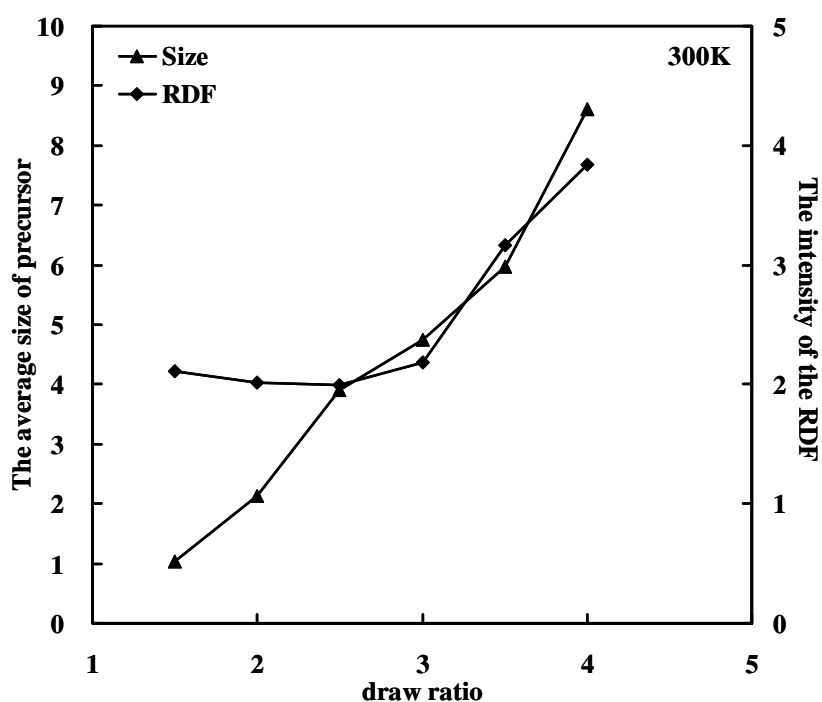


Figure C.15 The time evolution of RDF intensity (4.11\AA) (diamond) and the time averaged number of parallel segments contained in a representative precursor (triangle) at 300 K with draw speed $1 \times 10^{11} \text{s}^{-1}$. (27x14)

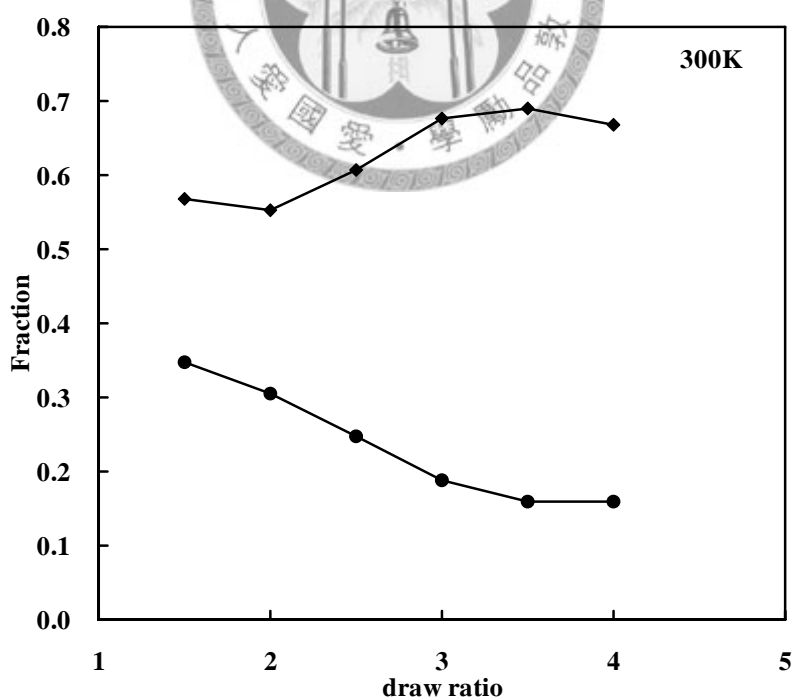


Figure C.16 the backbone torsions $\langle \phi_1 \rangle$ in trans (triangles) and $\langle \phi_2 \rangle$ in gauche (circles) for segments in a precursor (closed symbols) and outside any precursor (open symbols) at 300 K with draw speed $1 \times 10^{11} \text{s}^{-1}$. (27x14)

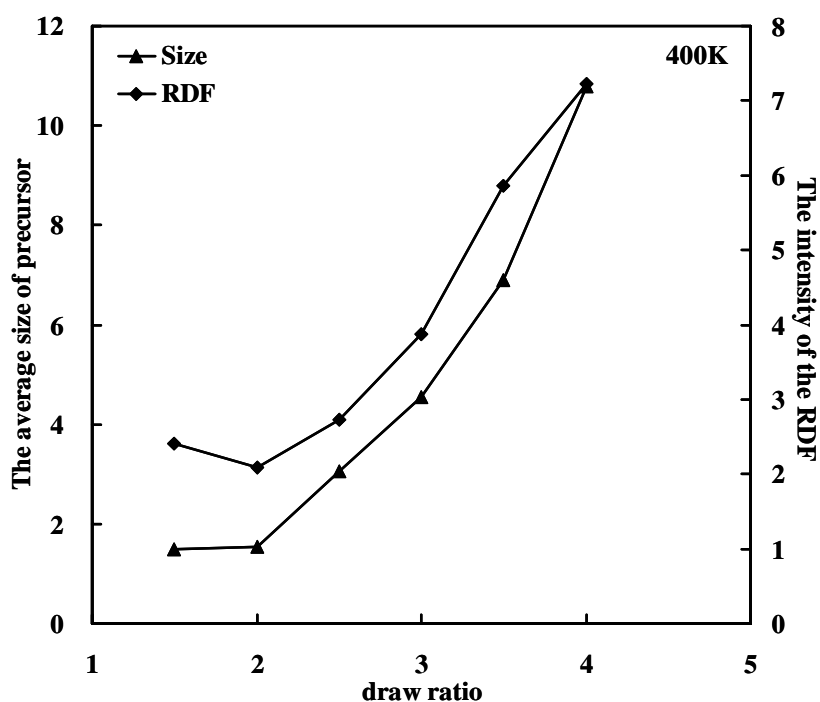


Figure C.17 The time evolution of RDF intensity (4.11Å) (diamond) and the time averaged number of parallel segments contained in a representative precursor (triangle) at 400 K with draw speed $1 \times 10^{11} \text{ s}^{-1}$. (27x14)

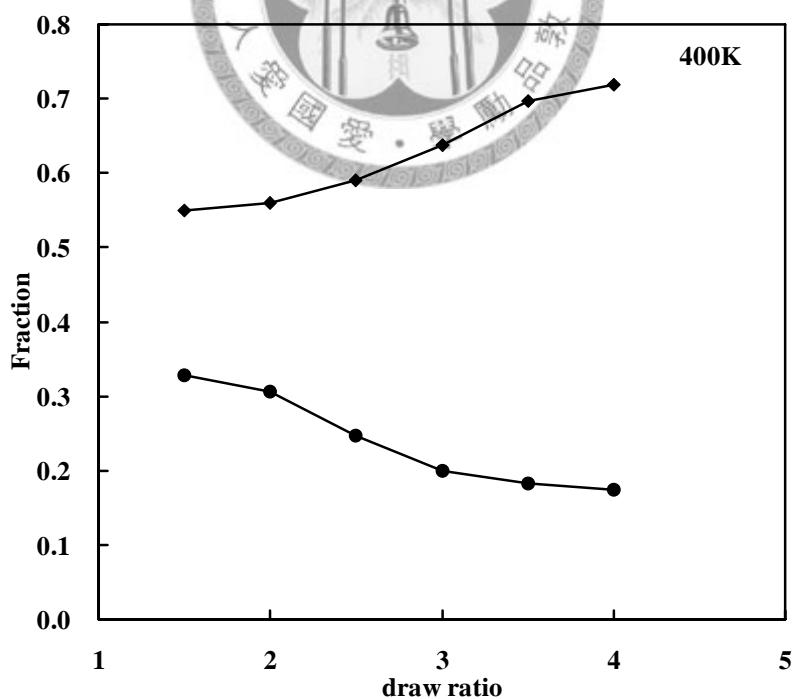


Figure C.18 the backbone torsions $\langle \phi_1 \rangle$ in trans (triangles) and $\langle \phi_2 \rangle$ in gauche (circles) for segments in a precursor (closed symbols) and outside any precursor (open symbols) at 400 K with draw speed $1 \times 10^{11} \text{ s}^{-1}$. (27x14)

Reference

1. Yamamoto, T. (2005), "Molecular dynamics modeling of the crystal-melt interfaces and the growth of chain folded lamellae," in *Interphases and Mesophases in Polymer Crystallization III*, pp. 37, G. Allegra, ed. New York, Springer.
2. Sperling, L. H., "Introduction to Physical Polymer Science," 2nd eds. John Wiley & Sons, Inc., New York, Pages (1992).
3. Keller, A., "A Note on Single Crystals in Polymers - Evidence for a Folded Chain Configuration," *Philosophical Magazine*, **2**, 1171 (1957).
4. Avrami, M., "Kinetics of phase change I - General theory," *Journal of Chemical Physics*, **7**, 1103 (1939).
5. Keith, H. D. and F. J. Padden, "Spherulitic Crystallization from Melt .I. Fractionation + Impurity Segregation + Their Influence on Crystalline Morphology," *Journal of Applied Physics*, **35**, 1270 (1964).
6. Imai, M., K. Kaji, T. Kanaya, et al., "Ordering Process in the Induction Period of Crystallization of Poly(Ethylene-Terephthalate)," *Physical Review B*, **52**, 12696 (1995).
7. Imai, M., K. Mori, T. Mizukami, et al., "Structural Formation of Poly(Ethylene-Terephthalate) During the Induction Period of Crystallization .2. Kinetic-Analysis Based on the Theories of Phase-Separation," *Polymer*, **33**, 4457 (1992).
8. Heeley, E. L., A. V. Maidens, P. D. Olmsted, et al., "Early stages of crystallization in isotactic polypropylene," *Macromolecules*, **36**, 3656 (2003).
9. Fukao, K. and Y. Miyamoto, "Dynamical transition and crystallization of polymers," *Physical Review Letters*, **79**, 4613 (1997).

10. Soccio, M., A. Nogales, N. Lotti, et al., "Evidence of early stage precursors of polymer crystals by dielectric spectroscopy," *Physical Review Letters*, **98**, (2007).
11. Wang, Z. G., B. S. Hsiao, E. B. Sirota, et al., "Probing the early stages of melt crystallization in polypropylene by simultaneous small- and wide-angle X-ray scattering and laser light scattering," *Macromolecules*, **33**, 978 (2000).
12. Liu, C. and M. Muthukumar, "Langevin dynamics simulations of early-stage polymer nucleation and crystallization," *Journal of Chemical Physics*, **109**, 2536 (1998).
13. Muthukumar, M. and P. Welch, "Modeling polymer crystallization from solutions," *Polymer*, **41**, 8833 (2000).
14. Gee, R. H., N. Lacevic and L. E. Fried, "Atomistic simulations of spinodal phase separation preceding polymer crystallization," *Nature Materials*, **5**, 39 (2006).
15. Miura, T. and M. Mikami, "Molecular dynamics study of crystallization of polymer systems confined in small nanodomains," *Physical Review E*, **75**, (2007).
16. Kim, K. J., J. H. Bae and Y. H. Kim, "Infrared spectroscopic analysis of poly(trimethylene terephthalate)," *Polymer*, **42**, 1023 (2001).
17. Park, S. C., Y. R. Liang, H. S. Lee, et al., "Three-dimensional orientation change during thermally induced structural change of oriented poly(trimethylene terephthalate) films using polarized FTIR-ATR spectroscopy," *Polymer*, **45**, 8981 (2004).
18. Lee, H. S., S. C. Park and Y. H. Kim, "Structural changes of poly(trimethylene terephthalate) film upon uniaxial and biaxial drawing," *Macromolecules*, **33**, 7994 (2000).
19. Jeong, Y. G., W. J. Bae and W. H. Jo, "Effect of uniaxial drawing on surface chain structure and surface tension of poly(trimethylene terephthalate) film," *Polymer*, **46**,

- 8297 (2005).
20. Wu, J., J. M. Schultz, J. M. Samon, et al., "In situ study of structure development in poly(trimethylene terephthalate) fibers during stretching by simultaneous synchrotron small- and wide-angle X-ray scattering," *Polymer*, **42**, 7141 (2001).
 21. Koyama, A., T. Yamamoto, K. Fukao, et al., "Molecular dynamics simulation of polymer crystallization from an oriented amorphous state," *Physical Review E*, **65**, (2002).
 22. Lavine, M. S., N. Waheed and G. C. Rutledge, "Molecular dynamics simulation of orientation and crystallization of polyethylene during uniaxial extension," *Polymer*, **44**, 1771 (2003).
 23. Dukovski, I. and M. Muthukumar, "Langevin dynamics simulations of early stage shish-kebab crystallization of polymers in extensional flow," *Journal of Chemical Physics*, **118**, 6648 (2003).
 24. Saitta, A. M. and M. L. Klein, "Influence of a knot on the stretching-induced crystallization of a polymer," *Journal of Chemical Physics*, **116**, 5333 (2002).
 25. Poulindandurand, S., S. Perez, J. F. Revol, et al., "Crystal-Structure of Poly(Trimethylene Terephthalate) by X-Ray and Electron-Diffraction," *Polymer*, **20**, 419 (1979).
 26. Desborough, I. J., I. H. Hall and J. Z. Neisser, "Structure of Poly(Trimethylene Terephthalate)," *Polymer*, **20**, 545 (1979).
 27. Bulkin, B. J., M. Lewin and J. Kim, "Crystallization Kinetics of Poly(Propylene Terephthalate) Studied by Rapid-Scanning Raman-Spectroscopy and Ft-Ir Spectroscopy," *Macromolecules*, **20**, 830 (1987).
 28. Chuah, H. H., "Orientation and structure development in poly(trimethylene terephthalate) tensile drawing," *Macromolecules*, **34**, 6985 (2001).

29. Jang, S. S. and W. H. Jo, "Analysis of the mechanical behavior of poly(trimethylene terephthalate) in an amorphous state under uniaxial extension-compression condition through atomistic modeling," *Journal of Chemical Physics*, **110**, 7524 (1999).
30. Zhang, J. L., "Study of poly(trimethylene terephthalate) as an engineering thermoplastics material," *Journal of Applied Polymer Science*, **91**, 1657 (2004).
31. Ward, I. M., M. A. Wilding and H. Brody, "Mechanical-Properties and Structure of Poly(Meta-Methylene Terephthalate) Fibers," *Journal of Polymer Science Part B-Polymer Physics*, **14**, 263 (1976).
32. Jakeways, R., I. M. Ward, M. A. Wilding, et al., "Crystal Deformation in Aromatic Polyesters," *Journal of Polymer Science Part B-Polymer Physics*, **13**, 799 (1975).
33. Yang, J. S. and W. H. Jo, "Analysis of the elastic deformation of semicrystalline poly(trimethylene terephthalate) by the atomistic-continuum model," *Journal of Chemical Physics*, **114**, 8159 (2001).
34. Huang, J. M. and F. C. Chang, "Crystallization kinetics of poly(trimethylene terephthalate)," *Journal of Polymer Science Part B-Polymer Physics*, **38**, 934 (2000).
35. Hong, P. D., W. T. Chuang, W. J. Yeh, et al., "Effect of rigid amorphous phase on glass transition behavior of poly(trimethylene terephthalate)," *Polymer*, **43**, 6879 (2002).
36. Hong, P. D., W. T. Chung and C. F. Hsu, "Crystallization kinetics and morphology of poly(trimethylene terephthalate)," *Polymer*, **43**, 3335 (2002).
37. Wu, P. L. and E. M. Woo, "Linear versus nonlinear determinations of equilibrium melting temperatures of poly(trimethylene terephthalate) and miscible blend with poly(ether imide) exhibiting multiple melting peaks," *Journal of Polymer Science*

Part B-Polymer Physics, **40**, 1571 (2002).

38. Sriramaoan, P., N. Dangseeyun and P. Supaphol, "Multiple melting behavior in isothermally crystallized poly(trimethylene terephthalate)," *European Polymer Journal*, **40**, 599 (2004).
39. Xu, Y., S. R. Ye, J. Bian, et al., "Crystallization kinetics analysis of poly(trimethylene terephthalate) including the secondary crystallization process," *Journal of Materials Science*, **39**, 5551 (2004).
40. Wang, X. S., D. Y. Yan, G. H. Tian, et al., "Effect of molecular weight on crystallization and melting of poly(trimethylene terephthalate). 1: Isothermal and dynamic crystallization," *Polymer Engineering and Science*, **41**, 1655 (2001).
41. Xue, M. L., J. Sheng, Y. L. Yu, et al., "Nonisothermal crystallization kinetics and spherulite morphology of poly(trimethylene terephthalate)," *European Polymer Journal*, **40**, 811 (2004).
42. Apiwanthanakorn, N., P. Supaphol and M. Nithitanakul, "Non-isothermal melt-crystallization kinetics of poly(trimethylene terephthalate)," *Polymer Testing*, **23**, 817 (2004).
43. Supaphol, P., N. Dangseeyun, P. Sriramaoan, et al., "Nonisothermal melt-crystallization kinetics for three linear aromatic polyesters," *Thermochimica Acta*, **406**, 207 (2003).
44. Liang, H., F. Xie, F. Q. Guo, et al., "Non-isothermal crystallization behavior of poly(ethylene terephthalate)/Poly(trimethylene terephthalate) blends," *Polymer Bulletin*, **60**, 115 (2008).
45. Chuah, H. H., "Crystallization kinetics of poly(trimethylene terephthalate)," *Polymer Engineering and Science*, **41**, 308 (2001).
46. Ohtaki, M., T. Kameda, T. Asakura, et al., "Structural characterization of drawn

- and annealed poly(trimethylene terephthalate) fibers," *Polymer Journal*, **37**, 214 (2005).
47. Wu, J., J. M. Schultz, J. M. Samon, et al., "In situ study of structure development during continuous hot-drawing of poly(trimethylene terephthalate) fibers by simultaneous synchrotron small- and wide-angle X-ray scattering," *Polymer*, **42**, 7161 (2001).
48. Kameda, T., M. Miyazawa and S. Murase, "Conformation of drawn poly(trimethylene terephthalate) studied by solid-state C-13 NMR," *Magnetic Resonance in Chemistry*, **43**, 21 (2005).
49. Ward, I. M. and M. A. Wilding, "Ir and Raman-Spectra of Poly(M-Methylene Terephthalate) Polymers," *Polymer*, **18**, 327 (1977).
50. Wu, T., Y. Li, Q. Wu, et al., "Thermal analysis of the melting process of poly(trimethylene terephthalate) using FTIR micro-spectroscopy," *European Polymer Journal*, **41**, 2216 (2005).
51. Malvaldi, M., G. Allegra, F. Ciardelli, et al., "Structure of an associating polymer melt in a narrow slit by molecular dynamics simulation," *Journal of Physical Chemistry B*, **109**, 18117 (2005).
52. Mayo, S. L., B. D. Olafson and W. A. Goddard, "Dreiding - a Generic Force-Field for Molecular Simulations," *Journal of Physical Chemistry*, **94**, 8897 (1990).
53. Becke, A. D., "Density-Functional Thermochemistry .3. the Role of Exact Exchange," *Journal of Chemical Physics*, **98**, 5648 (1993).
54. Lee, C. T., W. T. Yang and R. G. Parr, "Development of the Colle-Salvetti Correlation-Energy Formula into a Functional of the Electron-Density," *Physical Review B*, **37**, 785 (1988).
55. Miehlich, B., A. Savin, H. Stoll, et al., "Results Obtained with the

- Correlation-Energy Density Functionals of Becke and Lee, Yang and Parr," *Chemical Physics Letters*, **157**, 200 (1989).
56. Johnson, B. G., P. M. W. Gill and J. A. Pople, "The Performance of a Family of Density Functional Methods," *Journal of Chemical Physics*, **98**, 5612 (1993).
57. Gaussian 98 (2001), Revision A.11, Gaussian, Inc., Pittsburgh, PA.
58. Darden, T., D. York and L. Pedersen, "Particle Mesh Ewald - an N.Log(N) Method for Ewald Sums in Large Systems," *Journal of Chemical Physics*, **98**, 10089 (1993).
- 59.
60. Theodorou, D. N. and U. W. Suter, "Atomistic Modeling of Mechanical-Properties of Polymeric Glasses," *Macromolecules*, **19**, 139 (1986).
61. Brown, D. and J. H. R. Clarke, "Molecular-Dynamics Simulation of an Amorphous Polymer under Tension. 1. Phenomenology," *Macromolecules*, **24**, 2075 (1991).
62. Yashiro, K., T. Ito and Y. Tomita, "Molecular dynamics simulation of deformation behavior in amorphous polymer: nucleation of chain entanglements and network structure under uniaxial tension," *International Journal of Mechanical Sciences*, **45**, 1863 (2003).
63. Capaldi, F. M., M. C. Boyce and G. C. Rutledge, "Molecular response of a glassy polymer to active deformation," *Polymer*, **45**, 1391 (2004).
64. Lyulin, A. V., N. K. Balabaev, M. A. Mazo, et al., "Molecular dynamics simulation of uniaxial deformation of glassy amorphous atactic polystyrene," *Macromolecules*, **37**, 8785 (2004).
65. Plimpton, S., "Fast Parallel Algorithms for Short-Range Molecular-Dynamics," *Journal of Computational Physics*, **117**, 1 (1995).
66. Hentschke, R., "Simulation Methods for Polymer," eds. Dekker M., New York,

- Pages (2004).
67. Cerius² (2003), Accelrys Inc., San Diego.
 68. Mark, J. E., "Physical properties of polymers handbook," eds. AIP Press, N.Y., Pages (1996).
 69. Nose, S., "A Molecular-Dynamics Method for Simulations in the Canonical Ensemble," *Molecular Physics*, **52**, 255 (1984).
 70. Hoover, W. G., "Canonical Dynamics - Equilibrium Phase-Space Distributions," *Physical Review A*, **31**, 1695 (1985).
 71. Ho, R. M., K. Z. Ke and M. Chen, "Crystal structure and banded spherulite of poly(trimethylene terephthalate)," *Macromolecules*, **33**, 7529 (2000).

